Design, Synthesis, and Evaluation of MMP-11 FRET Substrates for the Early Detection of Pancreatic Cancer

Dissertation

zur Erlangung des akademischen Grades

des Doktors der Naturwissenschaften

(Dr. rer. nat.)

eingereicht im Fachbereich Biologie, Chemie, Pharmazie
der Freien Universität Berlin

vorgelegt von

M.Sc. Brit Sina Meyer

aus Münster

20. Januar 2011

Die Arbeit wurde im Zeitrahmen von Juli 2006 bis Dezember 2010 am Leibniz-Institut für Molekulare Pharmakologie (FMP) in Berlin unter Betreuung von Prof. Jörg Rademann durchgeführt.

1. Gutachter: Prof. Jörg Rademann

2. Gutachter: Prof. Rainer Haag

Disputation am 11. März 2011

Nothing shocks me. I'm a scientist!

Harrison Ford as *Indiana Jones*

für meine Eltern, Großeltern und Henrik

Zusammenfassung

Bauchspeicheldrüsenkrebs ist eine der Hauptursachen von Krebstodesfällen in Nordamerika und Europa mit einer mittleren Überlebensrate von nur 6 Monaten. Das Fehlen von Symptomen sowie diagnostischen Methoden führt in allen Fällen zur schlimmsten Prognose. Sektion der Bauchspeicheldrüse ist bisher die einzige Behandlungsmethode, die, wenn sie frühzeitig durchgeführt wird, die 5-Jahres Prognose auf 30 % hebt.[1] Konventionelle Imaging Methoden erkennen einen Tumor ab einer Größe von 1 cm, wonach eine Heilung bereits ausgeschlossen ist. Deshalb wurden, als Teil des Framework 6 EU Projektes "Novel molecular diagnostic tools for the prevention and diagnosis of pancreatic cancer" (MolDiag-PaCa) Zielgene identifiziert mit Hilfe einer Genexpressionsanalyse, die überexprimierte Gene in duktalen Adenocarzinomen berücksichtigt, die nicht in normalem Gewebe, Acinar Zellen oder in der Pankreatitis überexprimiert sind.
Matrix Metalloprotease 11 (MMP-11) wurde als Biomarker für Bauchspeicheldrüsenkrebs identifiziert und validiert. Proteasen wie MMP-11 können durch Fluoreszenz-markierte Substrate adressiert werden, die durch MMP-11 geschnitten werden. Eine Substratbibliothek wurde daher synthetisiert und *in vitro* evaluiert mittels eines FRET Assays und nachfolgender Identifizierung der Spaltprodukte per LC/MS-TOF. Das kombinierte, aktivste Substrat SM P 124 (k_{cat}/K_M = 9160 $M^{-1}s^{-1}$) wurde außerdem auf seine Aktivität gegenüber MMP-14 getestet wobei es 20 mal selektiver ist als vergleichbare Substrate mit ähnlich hoher Aktivität für MMP-11.
Zelluläre Assays bestätigten Substratumsatz mit MMP-11 überexprimierenden Zellen und zeigten keinen Umsatz mit der neg-

ativen Kontrollzelllinie Jurkat. Konfokalmikroskopieaufnahmen zeigten weiterhin nur wenig fluoreszierendes Hintergrundsignal eines negativen Kontrollsubstrates, im Gegensatz zum MMP-11 Substrat SM P 124, welches eine starke Färbung der Lösung, sowie Membran und Vesikeln zeigte. Kein Signal wurde beobachtet mit der Kontrollzelllinie Jurkat.
Zusätzlich wurde die Sonde als Imaging-Tracer weiterentwickelt, indem das Substrat an ein Copolymer gekuppelt wurde. Das Copolymer-Substrat Konjugat wurde erfolgreich *in vivo* in transgenen Tumormäusen und MIA PaCa-2 Xenograften getestet, die eine hochfluoreszente Bauchspeicheldrüse zeigten, wobei Kontrollmäuse kein Signal zeigten. Für nichtinvasive Bildgebung wurde zusätzlich eine Nahinfrarot (NIR) Probe entwickelt, deren Aktivität in MIA PaCa-2 Xenograften getestet wurde und fluoreszierende Tumoren lieferte.
Um eine räumliche Zuordnung des Signals zu gewährleisten wurde außerdem die Fluoreszein-markierte Sonde weiterentwickelt für Imaging mit hyperpolarisiertem (hp) Xenon ^{129}Xe.

Abstract

Pancreatic cancer is a major cause of cancer death in North America and Europe with a median survival rate of less than 6 months. Lack of symptoms and a dearth of diagnostic methods for its detection lead to its having one of the most dismal prognoses in all of medicine. Conventional imaging techniques detect tumors only at a minimum diameter of 1 cm at which point it has usually already reached malignant stage. The only treatment so far developed is that of pancreatic resection, but even when performed at an early stage, this treatment increases the 5-year survival rate to only 30%.[1]

Therefore, as part of the EU project "Novel molecular diagnostic tools for the prevention and diagnosis of pancreatic cancer" (MolDiag-PaCa), several target genes were identified with the help of a gene expression data analysis. This analysis included overexpressed genes in pancreatic ductal adenocarcinomas (PDAC) that are not expressed in normal ductal cells, acinar cells and pancreatitis.

Focus was placed on Matrix Metalloprotease 11 (MMP-11), a protease identified as a tumor biomarker that can be addressed by imaging substrates cleaved by MMP-11.

Consequently, a library of FRET-substrates was synthesized and successfully evaluated *in vitro* in a FRET assay while cleavage substrates were identified via LC/MS-TOF. The lead candidate SM P 124 (k_{cat}/K_M = 9160 $M^{-1}s^{-1}$) subsequently tested 20 times more selective for MMP-11 than comparable substrates with similarly high activity. Cellular assays confirmed cleavage with MMP-11 overexpressing cells, while no fluorescent signal was observed with negative control cell line Jurkat.

The probe was further developed for *in vivo* imaging by coupling the substrate to a copolymeric support (pHPMA) and designing the latter for near infrared (NIR) imaging. Transgenic tumor mice administered with the fluorescein-labeled copolymer-supported probe showed a strong fluorescent signal of the pretumorous pancreas, while control mice exhibited only weak background fluorescence. MIA PaCa-2 xenografts that were tested with NIRF-labeled substrate-copolymer conjugates also revealed a strong fluorescent tumor 24 h to 48 h after tail vein injection of the tracer and thereby successfully demonstrated for the first time imaging of MMP-11 activity *in vivo*.
In order to obtain spatially resolved images of MMP-11 activity, the probes were further developed for hyperpolarized (hp) ^{129}Xe imaging.

Danksagung

Ich danke Prof. Jörg Rademann für die Betreuung dieser Arbeit und vor allem für sein mir entgegengebrachtes Vertrauen für die Bearbeitung eines so spannenden und anspruchsvollen Themas.
Ich bedanke mich bei Prof. Rainer Haag für die Übernahme des Zweitgutachtens und des Prüfungsvorsitzes.
Weiterhin möchte ich mich speziell bei Prof. Rademann bedanken für die Erlaubnis ein dreimonatiges Auslandspraktikum in Shanghai, China zu absolvieren.
Für die Praktikumsstelle in Shanghai bedanke ich mich herzlich bei Dr. Steve Döring.
Vor allem möchte ich meinen Kooperationspartnern für die hilfreichen und anregenden Diskussionen und die gute Zusammenarbeit danken. Vielen Dank Prof. Stephan Hahn, Dr. Anette Sommer, Prof. Bence Sipos, Dr. Jens Waldeck, Dr. Anke Hahnenkamp, Dr. Dieter Saur und Dr. Leif Schröder.

Speziell möchte ich Katharina Koschek, Franziska Gottschalk, Keven Mallow und Chris Eckert hervorheben, die einen großen Beitrag zum Fortschritt des Projektes lieferten, sowie Stefanie Grosskopf, meiner Abzugsnachbarin, die immer für mich da war.
Besonders danke ich auch der gesamten Arbeitsgruppe für die Zusammengehörigkeit, die vielen interessanten und anregenden Diskussionen und das wunderbare Arbeitsklima. Danke Dr. Adeeb El-Dahshan, Dr. Kai Holland-Nell, Dr. Isabel Fernández, Dr. Vera Martos, Dr. Viviane Uryga-Polowy, Dr. Kim Boo Geun, Richard Raz, Johannes Preidl, André Horatscheck, Martin Richter, Jörn Saupe, Ahsanullah und vor allem Dr. Lioudmila Perepelittchenko. Dr. Christian Hoppmann möchte ich für viele Anregungen zur Peptidchemie danken.
Ich danke außerdem den Diplomanden Franziska Gottschalk und Michael Stolarski und den Praktikanten Felix Krüger, Barbara Stoess, Kerstin Paul und Sophia Möhl für die Mitarbeit an diesem Projekt.
Der Screening Unit unter Leitung von Dr. Jens-Peter von Kries

möchte ich für die Mitbenutzung der Geräte und der Möglichkeit zur Bearbeitung der Zellkultur danken. Zusätzlich bedanke ich mich bei Carola Seyffarth, Andreas Oder, Dr. Simone Graeber, Dr. Silke Radetzki, Dr. Martin Neuenschwander und Christoph Erdmann für die nette Zusammenarbeit und Hilfe.
Jenny Eichhorst und Dr. Burkhard Wiesner danke ich für die Einführung in die Konfokalmikroskopie.
Dr. Michael Lisurek danke ich für die Erstellung verschiedener Docking Simulationen, die die Grundlage der Diplomarbeit von Michael Stolarski stellte.
Zusätzlich danke ich meinem Standardtanz-Trainer Andreas Fischer, der mich durch sein Motto "einfach Machen!" ungeahnte Ziele erreichen ließ.
Ferner danke ich meinen Freunden für die wunderbare Ablenkung und besonders Henrik für seine Unterstützung und die gemeinsam verbrachte Zeit. Meinen Eltern und Großeltern danke ich herzlichst für die finanzielle und vor allem seelische Unterstützung.

Glossary

CD Circular Dichroism

CLSM Confocal laser scanning microscopy

Collidine 2,4,6-Trimethylpyridine

CT Computed tomography

Dabcyl (4-([4-(Dimethylamino)phenyl]azo)benzyl)

Dansyl (5-(dimethylamino)naphthalene-1-sulfonyl)

DAPI 4',6-diaminidin-2'-phenylindol-dihydrochloride

DBU 1,8-Diazabicyclo[5.4.0]undec-7-en

DCM Dichloromethane

DIC Diisopropylcarbodiimide

DIPEA Diisopropylethylamine

DMEM Dulbeccos Master's Eagle Medium

DMSO Dimethylsulfoxide

DPBS Dulbecco's phosphate buffered saline

ECM Extracellular Matrix

EDT Ethanedithiole

EE Ethyl acetate

EUS Endoscopic ultrasound

FITC Fluorescein isothiocyanate

FLI Fluorescence imaging

Fmoc 9-Fluorenylmethoxycarbonyl

Fmoc-Dap(ivDde)-OH Fmoc-3-((1-(4,4-dimethyl-2,6-dioxocyclohexylidene)-3-methylbutyl)amino)-L-alanine

Fmoc-PEG3-OH Fmoc-11-amino-3,6,9-trioxaundercanoic acid

FRI Fluorescence reflectance imaging

FRP free radical polymerization

GFP green fluorescent protein

HATU O-(7-Azabenzotriazol-1-yl)-N,N,N',N'-tetramethyluronium hexafluorophosphate

HOBt 1-Hydroxybenzotriazol

hp Hyperpolarized

HPMA N-(2-hydroxypropyl)methacrylamide

Hpx Hemopexin domain of matrix metalloproteases

HRP horseradish peroxidase

isoflurane 2-chloro-2-(difluoromethoxy)-1,1,1-trifluoro-ethane

kcat Units of substrate cleaved per second

Km Michaelis constant, concentration of substrate needed for half maximum enzyme velocity of cleavage

LC/MS Liquid chromatography

LC/MS-TOF Liquid chromatography - Time of flight

M Molar (mol/L)

MEM 2-Methoxyethoxymethyl

MeOH Methanol

Arg (A) Arginine

Asn (N) Asparagine

Asp (D) Aspartic acid

Dap Diaminopropionic acid

Gln (Q) Glutamine

Glu (E) Glutamic Acid

Gly (G) Glycine

His (H) Histidine

Ile (I) Isoleucine

Leu (L) Leucine

Lys (K) Lysine

Phe (F) Phenylalanine

Pro (P) Proline

Ser (S) Serine

Thr (T) Threonine

Tyr (Y) Tyrosine

Val (V) Valine

MMF medetomidine, midazolam and fentanyl

MMP Matrix Metalloprotease

MMP-11 Matrix Metalloprotease 11, Stromelysin 3 (ST-3)

MMP-14 Matrix Metalloprotease 14, Membrane Type Metalloprotease 1 (MT1-MMP)

MRI Magnetic resonance imaging

NCL Native chemical ligation

NIR Near Infrared

NIRF Near Infrared Fluorophore

OD Optical density

PanIN Pancreatic Intraepithelial Neoplasia

Pbf N-omega-(2,2,4,6,7-pentamethyldihyrdobenzofuran-5-sulfonyl

PBS Phosphate buffered saline

PDAC Pancreatic ductal adenocarcinoma

PDI Polydispersion index

PEG Polyethylenglycol

PET Positron emission tomography

pHPMA N-(2-hydroxypropyl)methacrylamide copolymer

ppm Parts per million

proMMP MMP with attached, inactivating prodomain

RFU Relative fluorescence unit

RIPA Radio-Immunoprecipitation Assay buffer

RLI Relative luminescence intensity

RT Room temperature

S1' Specificity pocket of MMPs

SDS Sodium dodecyl sulfate

SDS - PAGE SDS - polyacrylamide gel electrophoresis

SPECT Single-photon emission computed tomography

t Time

tBu tert-Butyl

TFA Trifluoroacetic acid

THF Tetrahydrofuran

TIMP Tissue Inhibitor of Matrix Metalloproteases

TIS Triisopropylsilane

Tris-HCl 2-Amino-2-hydroxymethyl-propane-1,3-diol

Trt Trityl

U Unit (100 pmol/min)

US Ultrasound

Contents

1 Introduction **19**

1.1 General Information About Pancreatic Cancer . 19

1.1.1 Pancreatic Cancer 19

1.1.2 Environmental and Genetic Factors of Pancreatic Cancer 22

1.1.3 Pancreatic Ductal Adenocarcinoma (PDAC) and Pancreatic Intraepithelial Neoplasia (PanIN) 23

1.1.4 Metastasis of PDAC 26

1.1.5 Matrix Metalloproteases (MMPs) 27

1.1.5.1 Matrix Metalloprotease 11 (MMP-11) 35

1.1.5.2 MMP-11 and Pancreatic Cancer 38

1.2 Early Diagnosis 43

1.2.1 Molecular Imaging in Cancer 43

1.2.1.1 Förster Resonance Energy Transfer (FRET) 47

1.2.1.2 Hyperpolarized Xenon (hp ^{129}Xe) Imaging 51

2 Aim of Thesis **56**

3 Results and Discussion **57**
3.1 Previous Work and Validation 57
3.1.1 Target Identification 57
3.1.2 Biomarker Validation 59
3.1.3 FRET-Substrates as MMP-11 Imaging Tools 61
3.2 Synthesis 63
3.2.1 MMP-11 Substrates 63
3.2.2 FRET Substrate Library Preparation . . 65
3.2.2.1 Library Construction 65
3.2.2.2 Synthesis of FRET Substrate Library 70
3.2.3 FRET Efficiency 82
3.3 *In vitro* Validation of FRET Imaging Substrates 90
3.3.1 Activity Determination 90
3.3.1.1 Kinetic FRET Assay 93
3.3.1.2 LC/MS-TOF Validation 101
3.3.1.3 Substrate Activity Comparison MMP-11/MMP-14 105
3.3.2 Activity Comparison Throughout the MMP Family 114
3.3.2.1 Kinetic FRET Assay 114
3.3.2.2 LC/MS-TOF Validation 119
3.3.3 Cellular Kinetic FRET Assay 124
3.3.4 Confocal Laser Scanning Microscopy of FRET Substrates 127
3.4 Polymer-Supported FRET Imaging Substrates . 132
3.4.1 Synthesis of Polymer-Supported FRET Substrates 134
3.4.1.1 Synthesis of Fluorescein-labeled Copolymer-Substrate Conjugates 134

3.4.1.2 FRET Efficiency 139
3.4.1.3 Synthesis of NIRF-labeled Copolymer-Substrate Conjugates 140
3.4.1.4 Quenching Efficiency 146
3.5 *In vitro* Validation of Polymer-Supported Imaging Substrates 149
3.5.1 Cellular FRET Assays 149
3.5.1.1 Fluorescein-labeled Copolymer-Substrate Conjugates 149
3.5.1.2 NIRF-labeled Copolymer-Substrate Conjugates 150
3.5.2 Confocal Laser Scanning Microscopy of Copolymer Conjugates 153
3.5.2.1 Fluorescein-labeled Copolymer-Substrate Conjugates 153
3.5.2.2 NIRF-labeled Copolymer-Substrate Conjugates 154
3.6 *In vivo* Validation of Polymer-Supported Imaging Substrates 160
3.6.1 Fluorescein-labeled Copolymer-Substrate Conjuagates 161
3.6.1.1 MIA PaCa-2 Xenograft Biodistribution *ex vivo* 161
3.6.1.2 Xenograft Imaging *in vivo* - Tumor Signal Determination 163
3.6.1.3 Transgenic Mice Imaging *in vivo* 165
3.6.2 NIRF-labeled Copolymer-Substrate Conjugates 168
3.6.2.1 MIA PaCa-2 Xenograft Biodistribution *ex vivo* 168

3.6.2.2 Xenograft Imaging *in vivo* . . . 174
3.7 Synthesis of Cryptophane-A-labeled Copolymer-Substrate Conjugates 183

4 Conclusion and Outlook 195

5 Experimental Part 207
5.1 General Materials and Instruments 207
5.2 Solid Phase FRET Substrate Synthesis Methods and Analysis 214
5.2.1 Preparation of FRET Substrates 215
5.2.2 Labeling Syntheses 219
5.2.3 Absorption and Emission Spectra 220
5.2.4 FRET Substrate Sequences and Analysis 221
5.3 *In vitro* Validation Methods and Conditions . . . 226
5.3.1 Kinetic Förster Resonance Energy Transfer (FRET) Assay 226
5.3.2 Cellular Kinetic FRET Assay 228
5.3.3 Western Blots 229
5.3.4 Confocal Laser Scanning Microscopy . . . 231
5.4 *In vivo* Validation Methods and Conditions . . . 233
5.4.1 Fluorescence Reflectance Imaging (FRI) . 233
5.4.2 Transgenic Mouse Imaging 233

6 Appendix 235

1 Introduction

1.1 General Information About Pancreatic Cancer

1.1.1 Pancreatic Cancer

Pancreatic cancer is the fourth major cause of cancer death in North America and Europe, with a number of 29,200 and 30,000 estimated new cases each year, respectively.[2, 3] Even though it is not a very common disease, accounting for only 6% of all cancer cases, pancreatic cancer is an aggressive and devastating type of cancer (Figure 1.1.1).

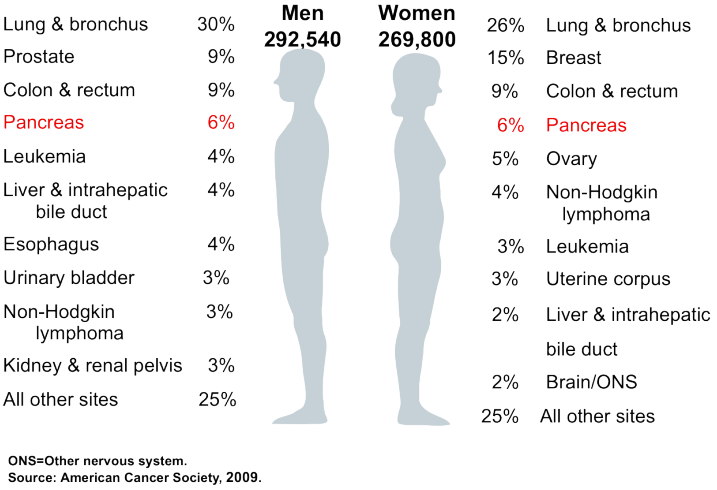

Figure 1.1.1: Cancer deaths in percentages in the U.S. for men and women in 2009 [2]

Lack of symptoms results in late diagnosis in which the cancer has already formed a tumor, resulting in a median survival rate of less than 6 months. Additionally, pancreatic cancer is known to metastasize early during the course of the disease to the regional lymph nodes and the liver.[4, 5, 6]

The statistic in figure 1.1.2 depicts data from 1989 to 1996, showing that pancreatic cancer is independent of race and sex (Figure 1.1.1), while the five-year survival rate strongly depends on the spreading of the cancer.[2] In 50 % of all cases pancreatic cancer spreads early, resulting in a five-year survival rate that is by far the worst compared to other types of cancer, and decreases further down to 1 % with the spreading of the disease.

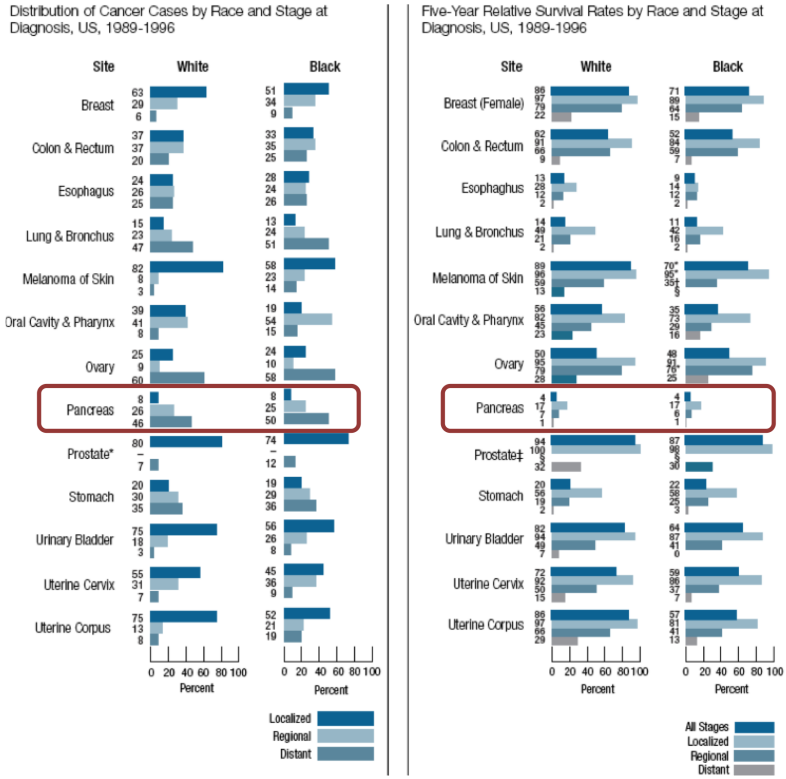

Figure 1.1.2: Distribution of cancer cases throughout race and stage in comparison to five-year survival rate throughout race and stage [2]

The only treatment currently available is pancreatic resection. Unfortunately, only 10 % of the patients diagnosed with pancreatic cancer are healthy enough to survive this surgical intervention.[7] Even when performed at an early stage, the operation increases the 5-year survival rate to only 30%.[1] And even then, most patients experience a relapse within 12 - 18 months.[7]

1.1.2 Environmental and Genetic Factors of Pancreatic Cancer

The causes of pancreatic cancer are difficult to determine and are usually summarized by age, smoking, pancreatitis and a family history of pancreatic cancer.

Advancing age is probably the highest risk factor for this disease, since risk of pancreatic cancer increases 40 fold between the ages of 40 and 80.[8] Behavioral factors such as tobacco smoking increase the risk of pancreatic cancer by a factor of at least 2.[9] DNA adducts of aromatic amines from tobacco smoke have been detected in pancreatic tissue, suggesting genetic mutations caused by tobacco carcinogens.[10, 11, 12] Moreover, it was found that high exposure to cadmium is associated with pancreatic cancer, since cadmium accumulates in the pancreas after uptake. Risch suggests that potentiated acidic gastric secretion is responsible for the pancreatic carcinogenesis.[13] Inheritance of pancreatic cancer has also been studied and was found to increase the risk by a factor of 2 to 3.[14] 10 % of all pancreatic cancer cases are associated with inherited predisposition.[15] Correspondingly, germline mutations of the following genes BRCA2, CDKN2A, STK11, p53, APC, HNPCC, AT, FANCC, and FANCG are related to hereditary pancreatic cancer.[16, 17, 18, 19, 20, 21, 22] Furthermore, diseases such as diabetes mellitus (non-insulin-dependent) and chronic pancreatitis are associated with this type of cancer.[7] AB Lowenfels and coworkers determined the risk factor for chronic pancreatitis patients with a minimum of two years follow up to be 16.5 times higher than for the general population and accounting for 10 % of all pancreatic cancer cases.[23] Recently, a concensus has emerged that this association between

inflammation of the pancreas and its cancer should be recognized by a new classification as pancreatic intraepithelial neoplasia (PanIN) for noninvasive precursor lesions.[24] These lesions, well-defined and noninvasive, are nonetheless strongly associated with infiltrating pancreatic ductal adenocarcinoma (PDAC).[25]

1.1.3 Pancreatic Ductal Adenocarcinoma (PDAC) and Pancreatic Intraepithelial Neoplasia (PanIN)

More than 85 % of tumors evolving in the pancreas originate from ductal cells. These tumors are called pancreatic ductal adenocarcinoma (PDAC).[26, 15] The term adenocarcinoma is used when cancer originates from glandular tissue such as the exocrine pancreas, consisting of ductal and acinar cells. Acini cells are responsible for digestive zymogen secretion to the branched network of ductal cells, delivering juice to the gastrointestinal tract. The endocrine pancreas, consisting of four specialized cell types organized in clusters called Langerhans Islets, is responsible for hormone secretion to the blood pool. Endocrine tumors, however, account for only 1 % of pancreatic cancer cases, which is why focus was placed on exocrine PDAC.[26] Figure 1.1.3 shows the general anatomy of the pancreas.

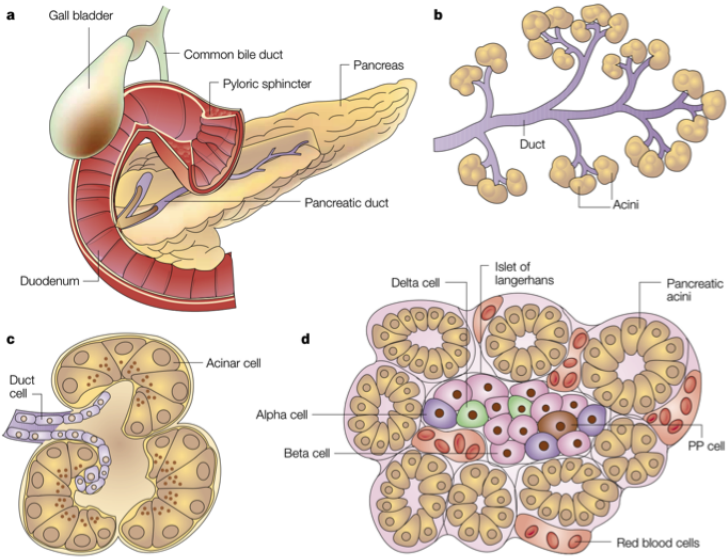

Figure 1.1.3: Anatomy of the pancreas; a) Pancreas with duct leading to duodenum; b) Exocrine pancreas c) Acinar cell; d) Pancreatic islet (endocrine pancreas) embedded in exocrine tissue. The exocrine pancreas consists of acini and ductal cells. (Figure 3b) The former produce all digestive enzymes and account for the majority of pancreatic tissue (80 %) while the latter secret mucous and bicarbonate to the digestive mixture before the juice is emtied into the duodenum. (Figure 3a) Next to the acini cells the endocrine pancreatic tissue (Islets of Langerhans, Figure 3d) produces hormones that are secreted directly to the blood stream.[26]

In general, it is believed that ductal cells are the progenitor cells of pancreatic adenocarcinoma.[26] Lesions within the duct, for example, can occur due to genetic alterations of genes such as K-

ras, p16, p53, DPC4, and BRCA2. [27, 28, 29, 30, 31, 32, 33, 34, 35] K-ras mutations are usually the first genetic changes occurring during lesion progression. 30 % of K-ras affected lesions are detected at the earliest stages of histological diversification.[36] These lesions result in increased proliferation of altered cells, intraductal lesions, and neogenesis.[26] To describe the different morphologies of dysplasia, three stages of PanINs were determined by Klimstra and Longnecker in 1994.[36]
Normal, healthy ductal pancreatic cells are flat, cuboidal epithelial cells. (Figure 1.1.4) However, during the first stages of noninvasive lesions, PanIN-1A and PanIN-1B display elongated or papillary cell architecture, respectively. Up to this point, lesions can still be a cause of inflammation (pancreatitis), meaning that stages PanIN-1A and 1B are not necessarily precursors of PDAC rendering them as low risk stages with hardly any neoplastic potential.[37] PanIN-2 ductal cells show the same elongated or papillary structure with mild to moderate dysplasia, such as nuclear abnormalities and some loss of polarity, while PanIN-3 displays severe dysplasia with severe nuclear atypia and intraluminal "budding".[25, 26] Furthermore, PanIN-3 shows the same genetic profile as PDAC and can therefore be considered a high-risk precursor stage of PDAC. For this reason, PanIN-2 lesions mark the starting point of neoplastic changes leading to invasive PDAC with severe desmoplasia, shown by immunohistochemistry in Figure 1.1.5.[37] Furthermore, targeting of stages PanIN-2 and PanIN-3 would allow an early diagnosis of high risk patients for PDAC.

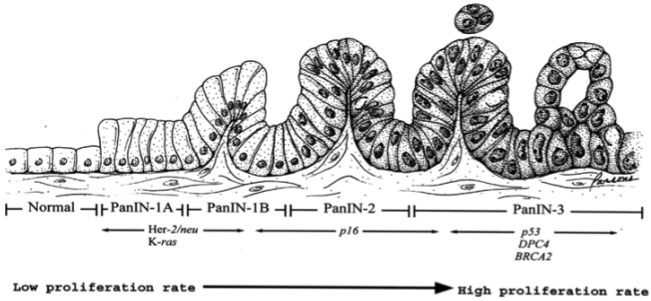

Figure 1.1.4: From non-invasive lesions to infiltrating adenocarcinoma in three stages [25]

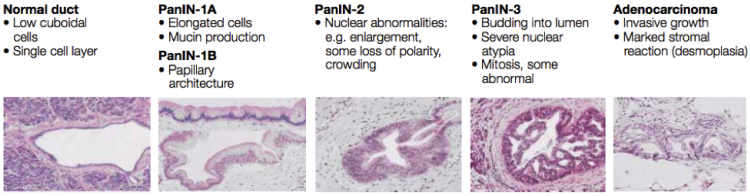

Figure 1.1.5: Immunohistochemistry of normal pancreatic duct in comparison to PanINs and adenocarcinoma [26]

1.1.4 Metastasis of PDAC

Desmoplasia is defined as connective tissue growth, meaning strong proliferation of stromal fibroblasts and deposition of extracellular matrix components like matrix metalloproteases and collagenes.[38] PDAC is known for its desmoplastic response and its propensity for early and distant metastasis.[15] Breakdown of

the extracellular matrix is a major factor for invasiveness and early metastatic development of the cancer. In order for the cells to become metastatic, the basement membrane has to be crossed. Since the basement membrane is primarily composed of type IV collagen, laminin, and heparin sulfate proteoglycans, a corresponding expression of proteases that degrade the mentioned components is required.[39] Three classes of such proteases are known to focally break down the basement membrane and therefore support metastasis: Serin proteases such as plasmin/plasminogen system, cathepsin proteases like cathepsin B, D, E and I, and matrix metalloproteases.[40]

1.1.5 Matrix Metalloproteases (MMPs)

Matrix metalloproteases are calcium-containing, zinc-dependent endopeptidases expressed in the extracellular matrix (ECM) and functioning as degradation/remodelling enzymes.[41] MMPs belong to one of the most important families of proteases, participating in ECM breakdown and thereby facilitating invasive behaviour of cancerous tissue.[42]

MMP activity is regulated by transcription, activation of precursor zymogens (proMMPs) due to prodomain cleavage by activator proteases (e.g. furin or plasmin) or by other MMPs, and inhibition of α_2-macroglobulin and endogenous tissue inhibitors of metalloproteases, so-called TIMPs. The MMP family currently consists of more than 25 members divided into 6 subgroups differing in protease domain construction and therefore substrate preferability.[41]
For instance, collagenases like MMP-1, -8, and 13 are mainly concerned with the cleavage of different types of collagenes while

gelatinases MMP-2 and -9 preferably cleave gelatin, a partly hydrolized form of collagene along with collagene (Figure 1.1.6). Stromelysins MMP-3, -10, and -11 (ST-1, ST-2, and ST-3) exhibit differing substrate preferences as MMP-3 usually cleaves gelatin and collagenes whereas MMP-10 cleaves laminin, fibronectin and elastin. MMP-11 however, has only weak activity against ECM proteins such as collagen IV, fibronectin, laminin, and aggrecan, a cartilage protein.[43, 44] Therefore, MMP-11 is often grouped with "Other" Metalloproteases in subgroup 6 rather than "Stromelysins" in subgroup 3. Subgroup 4, 5, and 6 contain MMPs that mostly cleave standard MMP substrates like fibronectin, gelatin and laminin. Subgroup 4 shows minimal domain MMPs such as MMP-7 and MMP-26, both lacking the Hemopexin-like (Hpx) domain, whereas subgroup 5 displays membrane-type MMPs. "Other" MMPs in subgroup 6 predominantly exhibit physiological substrates such as aggrecan and ECM proteins.

Subgroup	MMP	Name	Substrate
1. Collagenases	MMP-1	Collagenase-1	Col I, II, III, VII, VIII, X, gelatin
	MMP-8	Collagenase-2	Col I, II, III, VII, VIII, X, aggrecan, gelatin
	MMP-13	Collagenase-3	Col I, II, III, IV, IX, X, XIV, gelatin
2. Gelatinases	MMP-2	Gelatinase A	Gelatin, Col I, II, III, IV, VII, X
	MMP-9	Gelatinase B	Gelatin, Col IV, V
3. Stromelysins	MMP-3	Stromelysin-1	Col II, IV, IX, X, XI, gelatin
	MMP-10	Stromelysin-2	Col IV, laminin, fibronectin, elastin
	MMP-11	Stromelysin-3	Col IV, fibronectin, laminin, aggrecan
4. Matrilysins	MMP-7	Matrilysin-1	Fibronectin, laminin, Col IV, gelatin
	MMP-26	Matrilysin-2	Fibrinogen, fibronectin, gelatin
5. MT-MMP	MMP-14	MT1-MMP	Gelatin, fibronectin, laminin
	MMP-15	MT2-MMP	Gelatin, fibronectin, laminin
	MMP-16	MT3-MMP	Gelatin, fibronectin, laminin
	MMP-17	MT4-MMP	Fibrinogen, fibrin
	MMP-24	MT5-MMP	Gelatin, fibronectin, laminin
	MMP-25	MT6-MMP	Gelatin
6. Others	MMP-12	Macrophage metalloelastase	Elastin, fibronectin, Col IV
	MMP-19		Aggrecan, elastin, fibrillin, Col IV, gelatin
	MMP-20	Enamelysin	Aggrecan
	MMP-21	XMMP	Aggrecan
	MMP-23		Gelatin, casein, fibronectin
	MMP-27	CMMP	Unknown
	MMP-28	Epilysin	Unknown

Figure 1.1.6: Members of the matrix metalloprotease family [41]

Typically, MMPs consist of a catalytic domain of 170 amino acids harboring a zinc binding motif HEXXHXXGXXH where the three histidines coordinate to and stabilize the catalytic zinc ion. Commonly, a propeptide (yellow) of about 80 amino acids containing a ‘‘cysteine switch’’ motif PRCGXPD impairs the catalytic cleavage pocket by cysteine coordination to the catalytic zinc (proMMP) (Figure 1.1.7a). This C-Zn^{2+}coordination results in inactivity of proMMPs by preventing a water molecule essential for catalysis from binding to the catalytic zinc ion. Additionally, MMPs contain a “Met-turn” located 8 amino acids after the zinc binding motif, which supports the structure around the catalytic zinc atom by additional coordination of methionine to the catalytic zinc. A hemopexin-like (Hpx) domain (orange

ribbon) of about 200 amino acids that is linked to the catalytic domain by a linker peptide H (Hinge region) (blue spheres) facilitates cleavage of collagenes and inhibition by TIMPs. MT-MMPs (Membrane-type matrix metalloproteases) also bear a transmembrane domain (TM) that anchors these enzymes to the cell membrane. Furthermore, secreted MMPs contain a signalling peptide (Pre) that directs them to the endoplasmatic reticulum. Gelatin-binding MMPs (MMP-2, MMP-9) exhibit inserts resembling collagen-binding type II repeats of fibronectin (Fi), whereas furin-activated, secreted MMPs (MMP-11, MMP-28) contain a recognition motif (Fu) in between propetide and catalytic domain for the intracellular activation of furin-like serine proteases. The furin motif is also found in vitronectin-like insert (Vn) MMP-21 and MT-MMPs (MMP-14, MMP-15, MMP-16, MMP-24). MT-MMPs also contain a short cytoplasmic domain (Cy) as well as glycosylphosphatidylinositol (GPI)-anchored MMPs such as MMP-17 and MMP-25.[45, 46, 47]

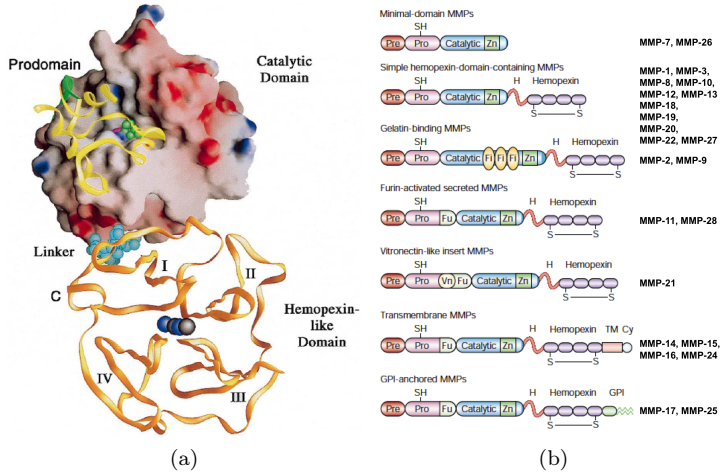

Figure 1.1.7: Common MMP domains a) Structural representation of full length MMP [48] b) Schematic domain representation of varying MMPs [50]

Furthermore, the catalytic domain consists of an open-sandwich topology where 2 out of 3 α-helices are packed against a 5 stranded β-sheet.[51] 1 to 3 structural calcium atoms and 1 structural zinc are imbedded into loops that form bulge segments of the catalytic domain. The catalytic zinc is located in the middle of the active site cleft and displays the center of protease activity.

MMPs strongly overlap in their substrate specificity due to their highly conserved catalytic domains throughout the family.[52] The main difference constitutes the S1' loop located to the right hand of the catalytic zinc. Due to its variation among different MMPs it is also called the specificity pocket.
MMPs 2, 3, 9, 12, 13, and 14, for instance, hold a Leu in position 214 (Leu214) thereby allowing formation of the S1' pocket as a

long, solvent-filled tube. In MMP-1 and MMP-7 this residue is occupied by Arg214 and Tyr214, both extending into the S1' opening and thereby limiting accommodation of the S1' subsite to ligands with short residues in P1'.[53] This has also been proven for substrate cleavage, since MMP-1 and MMP-7 do not cleave substrates with unnaturally long side chains in their P1' position.[54, 55] Furthermore, MMP-8 and MMP-9 harbor an arginine in position 243 and 242, respectively, that closes the pocket at the bottom allowing medium sized ligands to occupy these subsites.[56, 57] Superposition of catalytic domains of MMP-8 (yellow backbone), MMP-1, MMP-2, MMP-3, MMP-7, MMP-9, MMP-11, MMP-12, MMP-13, and MMP-14 (green) shows the highly conserved construction of catalytic domains and at the same time large deviations of the specificity loop S1' (Figure 1.1.8).

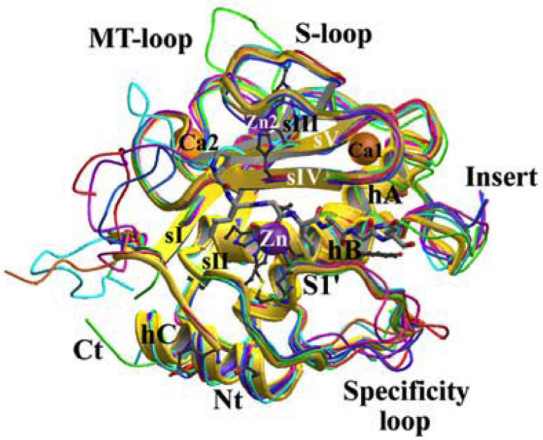

Figure 1.1.8: Crystal structure overlay of different MMPs [58]

Further subsites that were determined important for substrate binding via intensive substrate and inhibitor work are the hydrophobic S3, shallow subsite S2, extendable S1 and narrow S2' subsite.[58] Second in importance for substrate specificity is the hydrophobic subsite S3. The pocket is formed by rings of His162 and Phe164 and prefers to bind proline in this position (MMP-8 numbering). [48] S2 is a rather shallow depression constructed on top of an imidazole ring of third zinc-ligating His228. The polarity character of this pocket is influenced by residue 227, which is quite variable.

In collagene cleavage sites, S1 is mostly occupied by Gly, although longer residues can be fitted into the surface groove lined by His183 of the bulge edge strand and medium-sized residue 180 ranging from serine via isoleucine/leucine to phenylalanine. The S2' subsite forms a narrow cleft of the bulge rim and the side chains of S1' wall-forming segment Pro-X239-Tyr where X is phenylalanine in MMPs 11, 14, 15, and 16. Therefore, P2' residues will have to squeeze into this narrow cleft, excluding bulky residues.[53, 48]

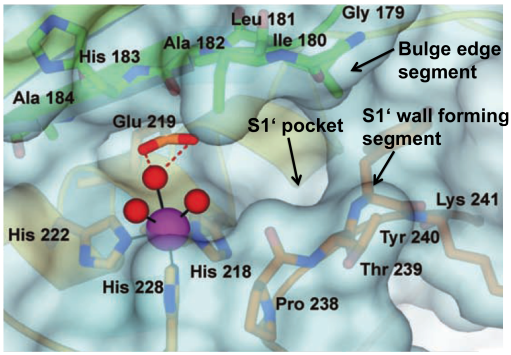

Figure 1.1.9: Active site cleft of MMP-12 [49]

Substrate cleavage is achieved via a general base mechanism involving Glu219.[59] The scissile peptide bond is strongly polarized by coordination to the catalytic zinc ion while Glu219 activates the zinc-bound catalytic water molecule that attacks the electrophilic carbonyl bond of the substrate with its lone electron pair. The tetrahedral intermediate is stabilized by zinc and the carbonyl function of neighboring alanine of the bulge edge strand. Glu219 acts as a proton shuttle first accepting a water proton and then losing it to the amino group, thereby again generating a charged glutamic acid that again binds a water proton, resulting in peptide bond cleavage (Figure 1.1.10).

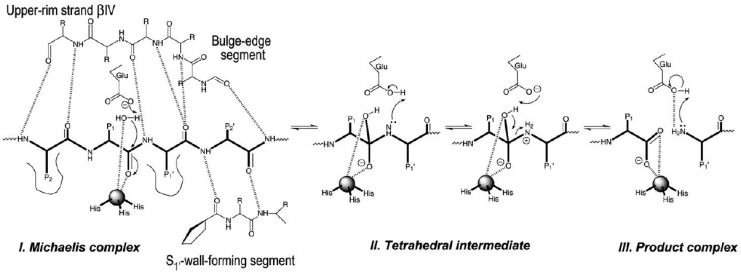

Figure 1.1.10: MMP-mediated substrate cleavage [52]

However, one MMP, MMP-11, varies strongly from the other MMPs in time and fashion of expression, substrate preference and subsite construction and therefore seems to have a different purpose. The next section will elucidate MMP-11 as an interesting target for pancreatic cancer.

1.1.5.1 Matrix Metalloprotease 11 (MMP-11)

MMP-11 strongly differs from other members of the MMP family. Expression of MMP-11 is observed in 80 to 100 % of invasive carcinomas of the breast, colon, head and neck, lung, ovary, prostate, skin, uterus, and pancreas.[60] Furthermore, MMPs such as MMP-1, MMP-3, MMP-10, MMP-11, and MMP-13 are not expressed in normal, healthy, and resting tissues. Expression is activated upon repair and remodeling processes and in diseased tissues.[41]
Most MMPs are secreted to and activated in the ECM. However, Pei and Weiss demonstrated that proMMP-11 is activated intracellulary and is then secreted, since proMMP-11 like proMT-MMPs posesses a furin recognition motif at the C-terminus of

the propeptide.[61, 62] Furthermore, an intracellular isoform (β-stromelysin 3, 40 kDa) has been detected and isolated from cultured cells and placenta by Luo et al. in 2002.[63] However, the function of this intracellular, active MMP-11 remains unknown.[46] Physiological substrates for MMP-11 are still under investigation, but it was shown that MMP-11 cleaves α-1-protease inhibitor (α1-PI), α_2-macroglobulin, and insulin-like growth factor binding protein-1 (IGFBP1).[64] Due to the fact that MMP-11 is expressed later than most of the other MMPs and in an active state, it is believed that MMP-11 is not involved in the initiation of basement membrane breakdown but rather in MMP-inhibiting protease degradation, ensuring MMP overexpression as well as overactivation leading to invasion of cancerous tissue.[65]

Moreover, MMP-11 contains a glutamine in position 215 located in the S1' subsite where most other MMPs occupy a conserved leucine.[66] This glutamine is essential for MMP-11 substrate cleavage as has been determined by activity determinations made with a Gln215-Ala215 mutant where substrate cleavage was reduced by a factor of 4.[55] Two water molecules were found to interact with the Gln215 and Arg244 (also unique in MMP-11) in the crystal structure of MMP-11. Figure 1.1.11 shows binding of a propylphenyl group of a phosphinic inhibitor to the S1' pocket of MMP-11. No interaction is established between ligand and pocket due to its hydrophobic residue. Introduction of a potential hydrogen donor might yield a hydrogen bond between ligand and pocket, thereby increasing affinity.

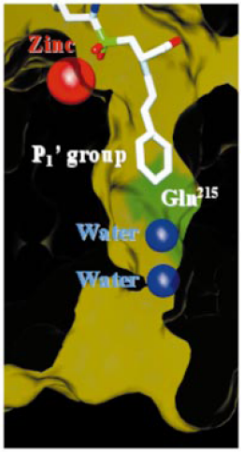

Figure 1.1.11: Crystal structure of S1' subsite of MMP-11 [66]

Furthermore, position 239 of the Met turn is occupied by an alanine in human MMP-11. Commonly, this position is occupied by a proline which interacts with a water molecule in order to stabilize substrate binding, due to hydrogen bond formation. This mutation explains the low overall proteolytic activity of human MMP-11, since a A239P mutant exhibited increased activity of MMP-11.[66, 64]
The S3 subsite also shows a large deviation from other MMPs. MMP-8 forms the S3 pocket of His162 and Phe164. His183 of MMP-11 is oriented in a similar way to His162 of MMP-8 but Phe185 of MMP-11 points into the opposite direction from Phe164 of MMP-8, resulting in lack of cavity formation for MMP-11 and explaining why MMP-11 does not prefer proline in P3 of substrates to be cleaved, as other MMPs do.[64]

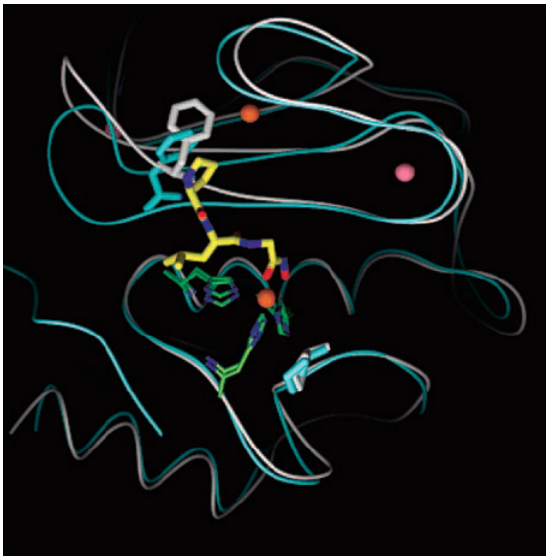

Figure 1.1.12: Superposition of MMP-11 crystal structure with that of MMP-8 [64]

1.1.5.2 MMP-11 and Pancreatic Cancer

MMP-11 was detected to be overexpressed in pancreatic cancer. Jones et al. were able to show up-regulation of MMP-11 in pancreatic tumor specimen collected from patients.[67] 75 specimen from tumor patients with PDAC and 10 specimen of normal tissue were compared whereas 52 of 75 (69%) PDAC specimen showed MMP-11 staining (carcinoma, stroma and adjacent pancreatitis) and only 2 out of 10 (20%) normal tissue probes showed a weak positive staining of epithelia, but no staining of stromal tissue. Therefore, significant up-regulation of MMP-11 was observed for pancreatic cancer (P=0,004) in the stromal tissue ad-

jacent to the tumor over normal pancreatic tissue. According to Jones et al, other significantly up-regulated metalloproteases in PDAC include MMP-3, MMP-7, and MMP-9. However, MMP-3 staining only showed significant staining differences when comparing tumor stroma with normal stroma ($P < 0.0001$). Still, all normal stroma probes stained for MMP-3 with an intensity of 2 on a scale from 0 to 3. Therefore, MMP-3 fails as a diagnostic marker for early detection. MMP-7 and MMP-9 were not detected in tumor stroma or adjacent pancreatitis, respectively. This limits detection to very small areas during diagnosis, even though cancer expression versus normal tissue expression varies significantly. Figure 1.1.13 shows MMP expression quantification determined by immunohistochemistry. Figure 1.1.14 depicts staining results of MMP-11 on PDAC versus normal tissue. MMP-11 staining is marked in red with strong staining of tumorous epithelial cells and a light stroma staining.

Immunohistochemical staining of pancreatic tissue

MMP or TIMP[a]		Pancreatic ductal adenocarcinoma			Normal pancreas			
Antibody for:	Staining intensity	Carcinoma	Stroma	Adjacent pancreatitis[a]	Epithelia	Stroma	Cancer vs. normal	Prognostic significance
MMP-1	0	16 (36%)	Nil	38 (85%)	7 (70%)	Nil	NS	NS
$N = 45$ PDAC,	1	11 (24%)		2 (4%)				
$N = 10$ normal	2	15 (33%)		5 (11%)	3 (30%)			
	3	3 (7%)						
MMP-2	0	25 (33%)[b]	Nil	35 (47%)	3 (30%)	Nil	NS	NS
$N = 75$ PDAC,	1	21 (28%)		9 (12%)	4 (40%)			
$N = 10$ normal	2	13 (17%)		17 (23%)	3 (30%)			
	3	16 (21%)		14 (19%)				
MMP-3	0	5 (11%)	18 (40%)	13 (29%)			stroma *vs.* stroma, $P < 0.0001$	NS
$N = 45$ PDAC,	1	16 (36%)	22 (49%)	1 (2%)	10 (100%)			
$N = 10$ normal	2	12 (27%)	5 (11%)	31 (69%)		10 (100%)		
	3	12 (27%)	0					
MMP-7	0	4 (9%)[b]	Nil	19 (42%)	8 (80%)	Nil	$P < 0.0001$	$P < 0.005$
$N = 45$ PDAC,	1	13 (29%)		6 (13%)	2 (20%)			
$N = 10$ normal	2	19 (42%)		16 (35%)				
	3	9 (20%)		4 (11%)				
MMP-8	0	12 (27%)[d]	Nil	2 (8%)	4 (40%)	Nil	$P = 0.04$	NS
$N = 45$ PDAC,	1	18 (40%)		9 (36%)	6 (60%)			
$N = 10$ normal	2	13 (29%)		13 (52%)				
	3	2 (4%)		1 (4%)				
MMP-9	0	26 (58%)	Nil	Nil	10 (100%)	Nil	$P = 0.0009$	NS
$N = 45$ PDAC,	1	13 (29%)						
$N = 10$ normal	2	3 (7%)						
	3	3 (7%)						
MMP-11	0	23 (31%)	53 (71%)	35 (47%)	8 (80%)	Nil	$P = 0.004$	$P = 0.02$
$N = 75$ PDAC,	1	20 (27%)	18 (24%)	9 (12%)	2 (20%)		(RT-PCR, $P = 0.0005$)	
$N = 10$ normal	2	18 (24%)	3 (4%)	17 (23%)				
	3	14 (19%)	1 (1%)	14 (19%)				
MMP-12	0	25 (56%)	Nil	20 (44%)		Nil	NS	NS
$N = 45$ PDAC,	1	19 (42%)		20 (44%)	8 (80%)			
$N = 10$ normal	2			5 (11%)	2 (20%)			
	3	1 (2%)						
MMP-14	0	31 (41%)[b,c,d]	Nil	37 (49%)	6 (60%)	Nil	NS	NS
$N = 75$ PDAC,	1	26 (35%)		22 (29%)	4 (40%)			
$N = 10$ normal	2	12 (16%)		15 (20%)				
	3	6 (8%)		1 (1%)				

Figure 1.1.13: MMP-11 expression in cancer vs normal tissue [67]

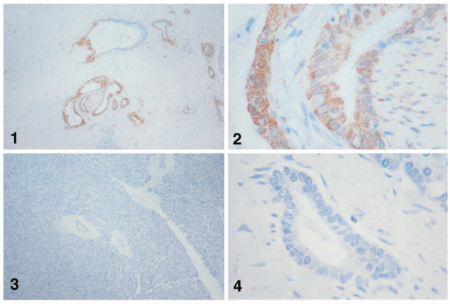

Figure 1.1.14: Immunohistochemical staining of MMP-11 in tumorous (1+2) and normal (3+4) tissue [67]

Moreover, results from reverse transcriptase PCR (RT-PCR) from 18 PDAC specimen and 8 normal controls also revealed significant up-regulation of mRNA levels for MMP-11 (P=0.0005). Additionally, MMP-11 was found to be strongly involved with positive lymph node status (P=0.0073) and was also identified as a prognostic marker for the patient's survival (P=0.02).[67] MMP-1 and MMP-15 also indicated up-regulation of mRNA levels, but since these metalloproteases failed immunohistochemistry staining, they were not further considered as diagnostic markers. mRNA levels of MMP-3, MMP-7, and MMP-9 were not significantly different from normal tissue. Therefore, they were also excluded as markers for early diagnosis of pancreatic cancer (Figure 1.1.15).

In summary, in comparison to other expressed MMPs, only MMP-11 was found to be significantly up-regulated in PDAC versus normal tissue, indicating, that up-regulation of mRNA levels is strongly involved with lymph node status and is a prognostic marker for survival. These facts point out the high selective potential of MMP-11 as a diagnostic biomarker for pancreatic cancer.

RT-PCR for the following:	Pancreatic ductal adenocarcinoma (N = 18)	Normal pancreas (N = 8)	Cancer *vs.* normal
MMP-1	0.027 (0.011–0.052)	0.004 (0.001–0.005)	$P = 0.006$
MMP-2	0.032 (0.016–0.073)	0.029 (0.017–0.122)	NS
MMP-3	0.00096 (0.00066–0.0017)	0.0037 (0.0005–0.011)	NS
MMP-7	0.032 (0.012–0.10)	0.044 (0.038–0.072)	NS
MMP-9	0.008 (0.004–0.02)	0.004 (0.001–0.02)	NS
MMP-11	0.057 (0.016–0.102)	0.0001 (0.0001–0.001)	$P = 0.0005$
MMP-14	2.4×10^{-5} (4.3×10^{-7}–2.1×10^{-4})	6.7×10^{-5} (3.2×10^{-5}–2.0×10^{-3})	NS
MMP-15	9.48×10^{-5} (1.3×10^{-5}–2.0×10^{-4})	1×10^{-3} (3.6×10^{-4}–2×10^{-3})	$P = 0.0026$
TIMP-1	0.76 (0.42–1.24)	0.338 (0.081–0.648)	$P = 0.030$
TIMP-2	0.002 (0.0004–0.004)	0.003 (0.001–0.006)	NS
TIMP-3	0.035 (0.01–0.06)	0.031 (0.006–0.075)	NS

Values are the median (inter-quartile range) expression ratio of the sample, glyceraldehyde-3-phosphate dehydrogenase NS, not significant. RT, reverse transcription; MMP, matrix metalloproteinases; TIMP, tissue inhibitor of the metalloproteinases; NS, not significant

Figure 1.1.15: MMP-11 mRNA levels determined by RT-PCR [67]

1.2 Early Diagnosis

1.2.1 Molecular Imaging in Cancer

Early diagnosis implies diagnosis at a stage where a tumor has not yet formed. At present, diagnostic concepts for pancreatic cancer involve abdominal ultrasound (US), computed tomography (CT), and endoscopic ultrasound (EUS).[68] Unfortunately, assessment of early pancreatic lesions (PanINs) leading to the formation of a tumor fails when these modalities are employed, due to limited sensitivity and accuracy.[69] However, genetic lesions of tissue leading to invasive carcinoma already show different protein expression patterns compared to healthy tissue as has been discussed in the previous section.
Molecular imaging addresses these cancer-specific proteins and makes them visible by the use of reporter molecules, such as fluorophores or radionuclides. Moreover, molecular imaging is noninvasive and enables quantification of targets at the molecular level.[70] It allows integration of molecular or physiological information specific to each patient, obtained by conventional imaging modalities. Typical modalities used are PET/SPECT imaging (Positron emission tomography / single-photon emission computed tomography), MRI (Magnetic resonance imaging), FLI (Fluorescence imaging), and US (Ultrasound).[71]

PET Positron emitting isotopes such as ^{11}C, ^{13}N, ^{15}O, ^{18}F, ^{64}Cu, ^{62}Cu, ^{124}I, ^{76}Br, ^{82}Rb and ^{68}Ga, with ^{18}F being the most clinically utilized, are incorporated into tracer molecules that detect a specific molecular target. Annihilation of the positrons emitted with nearby electrons yields high energized γ-photons

radiating in a 180° angle in opposing directions. Detection and signal origin reconstruction result in three-dimensional images with high sensitivity; their detection limit is a pM concentration of the tracer.[72] Unfortunately, positron emitting isotope generation requires access to a cyclotron, and due to the rather short half-lives (roughly 2 h for ^{18}F), imaging is limited to single processes.[73]

SPECT SPECT images are constructed by rotational detection around the body of γ-photons emitted by radionuclides. Typical γ-emitters include ^{99}Tc^{m} (6 h), ^{111}In (2.8 d), ^{123}I (13.2 h), and ^{125}I (59.5 d). Due to the longer half-lives of these γ-emitters, imaging of molecular processes is not limited to a short time range. Additionally, since a cyclotron is not needed to generate the respective radionuclides, this method is less costly and therefore preferred.[73] Still, due to irradiation safety issues, PET/SPECT imaging is mainly used for tracers that have been successfully preevaluated by optical imaging (Figure 1.2.1).

Optical Imaging Optical imaging methodologies include measurements of fluorescence, bioluminescence, absorption, or reflectance as the source of contrast.[70] Fluorescent optical imaging in particular is rapidly expanding as a noninvasive method for disease and tumor progression evaluation providing high sensitivity (nM), use of non-radioactive materials and safe detection, while employing readily available instruments at moderate cost.[75, 76] However, depth penetration of tissue is a limiting factor, due to high light scattering and absorption by water, hemoglobin, or collagenes.[77] Therefore, fluorophores such as fluorescein, absorbing at 485 nm are mostly used for *in vitro*

Imaging modality	Energy used	Spatial resolution (mm)	Temporal resolution (s)	Molecular sensitivity (mol/l)	Tissue penetration	Small animal or clinical	Cost	Advantages	Disadvantages
PET	Annihilation photons	1–4 animals; 6–10 clinical	1–300	10^{-11}–10^{-12}	>300	Both	$$$$	Sensitivity versatility, targeted probes	Cyclotron required, low radiation isotopes
SPECT	Gamma rays	0.5–5 animals; 7–15 clinical	60–20,000	10^{-10}–10^{-11}	>300	Both	$$$	Multiple probes simultaneously detected	10–100 fold < sensitive than PET
MRI	Radio frequency waves	0.025–0.1 animals; 0.2 clinical	60–3,000	10^{-3}–10^{-5}	>300	Both	$$$$	Anatomical & functional imaging, high spatial resolution	Low sensitivity, long acquired time, poor contrast
FLI	Visible to NIR light	2–10	10–2,000	10^{-9}–10^{-11}	1–20	Small animal	$	Physiological imaging & multiple types of probes	Attenuation and autofluorescence
Ultrasound	Ultrahigh frequency sound waves	0.05–0.5 animals; 0.1–1 clinical	0.1–100	$<10^{-12}$[a]	1–200	Both	$	Images morphology and physiology	Limited ability to image through bone & lungs

Dollar sign represents high, medium high, medium, and low cost for both purchasing equipment and usage fees.
[a] Information that is not well characterized

Figure 1.2.1: Advantages and disadvantages of varying imaging modalities [74]

validation of novel tracers, while near infrared (NIR) absorbing cyanine dyes are usually used for *in vivo* imaging of small animals, due to their higher tissue penetration and 700-800 nm absorption range where autofluorescence (absorption of water, blood and tissue) is at a minimum (Figure 1.2.2).[69]

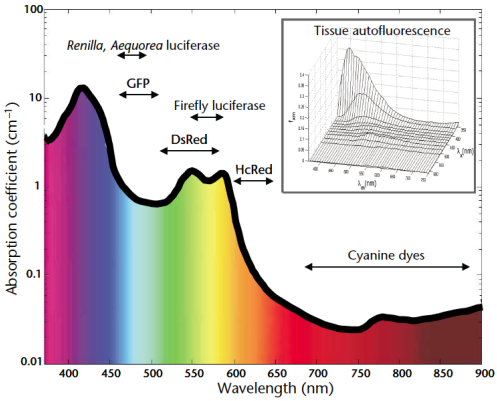

Figure 1.2.2: Absorption of differing fluorophores like GFP (green fluorescing protein) and cyanine dyes, adapted from [77]

Preparing molecular imaging probes calls for specific, high-affinity ligands with the ability to reach and stay in the tumor at sufficient concentration, in order to be detectable *in vivo*. Rapid excretion, non-specific binding, fast metabolism, and delivery barriers are common challenges faced in developing *in vivo* imaging probes.[70] High background signal due to non-specific binding points out an especially critical factor for high resolution images.[78]

"Smart" probes, activated upon contact with a target protein and

then producing a significant fluorescent signal, avoid an overall high background signal.[73] Preparation of such "smart" probes can be accomplished by employing a straightforward quenching methodology called Förster resonance energy transfer (FRET).

1.2.1.1 Förster Resonance Energy Transfer (FRET)

FRET is a phenomenon of a non-radiative excitation transmission of a donor molecule to an acceptor molecule due to coulombic dipole-dipole interactions. The transfer is dependent on an overlap of excitation spectrum of the donor with the emission spectrum of the acceptor, as depicted in figure 1.2.3.[79]

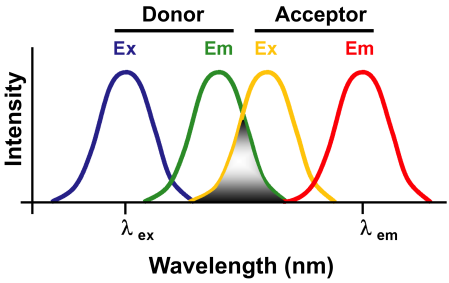

Figure 1.2.3: Spectral overlap of FRET donor emission with acceptor excitation [80]

Furthermore, spatial proximity ($<$ 10 nm) and a favorable orientation result in an effective transfer and a non-radiative excitation of the donor. The rate of energy transfer is determined by the reciprocal fluorescence lifetime of the donor, times the radius of 50 % transfer efficency, divided by the distance of donor and acceptor. The distance acts on the rate with a power of

6, whereas the orientation functions on the transfer rate by the power of 1. The following equation is employed to determine the rate of transfer k_T.

$$k_T \left[ns^{-1}\right] = \frac{1}{\tau_D}\left(\frac{R_0}{r}\right)^6 \quad (1.2.1)$$

with k_T = rate of transfer, τ_D= fluorescence lifetime of donor in the absence of acceptor, r = distance of donor and acceptor, R_0 = critical Förster radius (50 % energy transfer)

The critical Förster radius R_0 is the distance at which the energy transfer efficiency is 50%, calculated as follows (taking into account the orientation of donor to acceptor, the quantum yield of the donor, the overlap integral of emission spectrum of donor with excitation spectrum of acceptor as well as the refractive index of the solution):

$$R_0 \left[nm\right] = 2.11\times10^{-2}\left(\frac{\kappa^2 \Phi_D J(\lambda)}{n^4}\right)^{\frac{1}{6}} \quad (1.2.2)$$

with κ^2= $\sin\theta_D \sin\theta_A \cos\varphi$ - $2\cos\theta_D \cos\theta_A$ (orientation factor),
Φ_D= quantum yield of donor,
J= $\int_\lambda I_\lambda^D(\lambda)\varepsilon(\lambda)\lambda^4 d\lambda$ (overlap integral of donor and acceptor),
n = refractive index of solution

Figure 1.2.4a represents the effect of increasing distance to decreasing transfer efficiency by the power of six while figure 1.2.4b displays perfect alignment of donor and acceptor whenever the

angle along an axis of donor to acceptor is θ_{DA}= 0°. However, an angle of θ_{DA}= 90° yields an orientation factor of $\kappa^2 = 0$, resulting in energy transfer distinction. In solution, transition (dipole) moments of donor and acceptor are usually randomly oriented, e.g. in fluid solutions $\kappa^2 = \frac{2}{3}$.

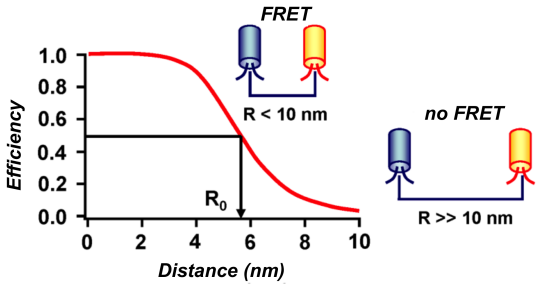

(a) Efficiency - distance relationship

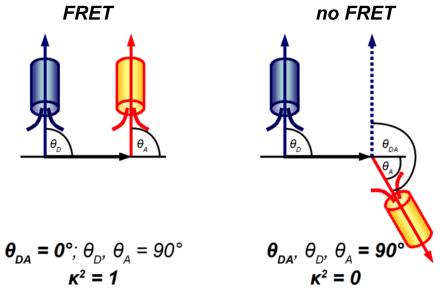

(b) Orientation dependance of donor and acceptor

Figure 1.2.4: Requirements for efficient Förster resonance energy transfer [80]

Furthermore, if the acceptor molecule is non-fluorescent, meaning that a successfull overlap of emission spectrum with excitation spectrum of acceptor results in non-radiative energy trans-

fer but yields no emission, then these kind of acceptors are also called dark quenchers, since they render fluorophores non-fluorescent.
Upon proteolytic activation of dark quenched probes, donor fluorophore and dark quencher will separate spatially and the fluorophore will regain its fluorescence like a light bulb that is turned on. Dabcyl (4-(4'-dimethylaminophenylazo)benzoic acid) is such a dark quencher chromophore, releasing heat by molecular vibrations instead of light upon excitation.[81] This exact method allows critical reduction of non-specific background signal for *in vivo* imaging.

MRI Magnetic resonance imaging employs radio frequency to alter induced magnetization of a body, thereby creating a rotating magnetic field that is detected by a scanner.[82] Non-invasive ^{1}H MRI is probably the most widely used technique for scanning deep tissue in diagnosis of human disease.[84] Spatial resolution is high, although a signal is only detected at mM concentrations, rendering MRI a quite insensitive method and making it ineffective for imaging of proteins with low expression levels in an up-regulated state. Amplification of the signal is therefore essential to employ MRI for molecular imaging purposes.[85]
Common contrast agents utilize gadolinium (Gd^{3+}), a highly paramagnetic element, to enhance signal-to-background ratio. However, a 1:1 ratio of tracer molecule to contrast complex is not sufficient to increase sensitivity. Moreover, Gd^{3+} is not internalized by cells, thereby excluding an intracellular accumulation effect over time for signal enhancement.[86]

In 1994, Albert et al. introduced the noble gas xenon (^{129}Xe) as a signal enhancing contrast agent for MRI after hyperpolariza-

tion. Hyperpolarization of ^{129}Xe increases magnetization by a factor of about 10^5 per nucleus, and thus results in strong signal enhancement.[87] Furthermore, ^{129}Xe is non-toxic in comparison to Gd^{3+} and is biologically inert when introduced to the body below anesthetic threshold of 70 % by volume of inhaled gas mixture. Additionally, ^{129}Xe exhibits a large NMR chemical shift sensitivity with a spectral window of over 200 ppm in aequeous solution and efficiently polarizable due to its large electron shell which is easily deformable.[84, 88]

1.2.1.2 Hyperpolarized Xenon (hp ^{129}Xe) Imaging

^{129}Xe can be hyperpolarized, for instance, by optical pumping with rubidium vapor. Therefore, circular polarized laser light at 795 nm is utilized to excite rubidium valence electrons to selectively depopulate a sub-ground state, resulting in an overpopulation of "up"-spin. (Figure 1.2.5a) Polarization transfer from photons to nuclear spins is called spin exchange optical pumping (SEOP).[89] Hyperpolarized xenon is then generated by colliding a continous stream of xenon gas with the hyperpolarized rubidium vapor. However, collisions with unpolarized buffer gas like N_2 result partly in quenching of hypolarization (Figure 1.2.5b).[90]

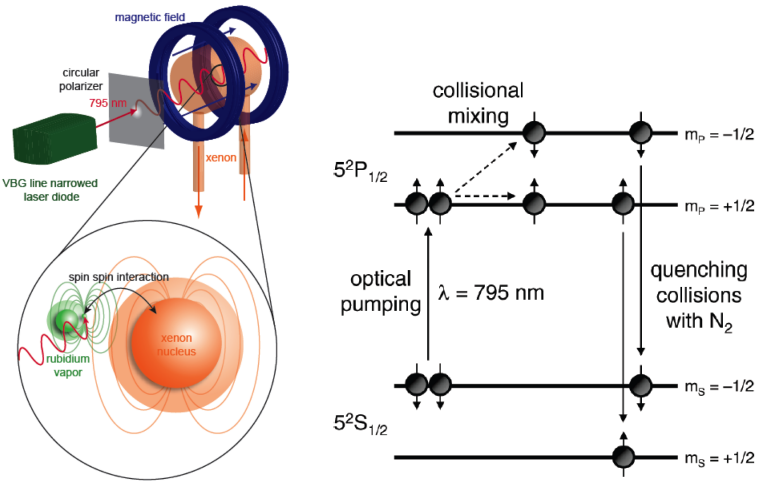

Figure 1.2.5: Hyperpolarization of ^{129}Xe a) Optical pumping for the preparation of hyperpolarized ^{129}Xe [91] b) Spin flip by optical pumping [90]

MR imaging of inhaled hp ^{129}Xe in the lungs, brain and other organs was demonstrated by Duhamel et al., Ruppert et al, and Driehuys et al. from 2001 to 2006.[92, 93, 94] However, even greater sensitivity is demanded of targeted hp ^{129}Xe tracers for *in vivo* molecular imaging purposes.[84]

Xenon was shown to bind reversibly to a molecular cage with a van der Waals volume of 95 Å^3 formed by two cyclotriveratrylene caps joined by three ethyl linkers also called Cryptophane-A.[84] Xenon binds to Cryptophane-A with an affinity of $K_A \sim$ 3900 M^{-1} in $C_2D_2Cl_4$ at 278 K.[95] Because of its large electron shell, ^{129}Xe, which moves freely in aqueous solution, behaves differently from caged ^{129}Xe in aqueous solution, distinguishable by

a chemical shift of > 120 ppm. Still, the signal evolving from caged xenon is only a fraction of the signal that is measured from xenon floating around freely (Figure 1.2.6).

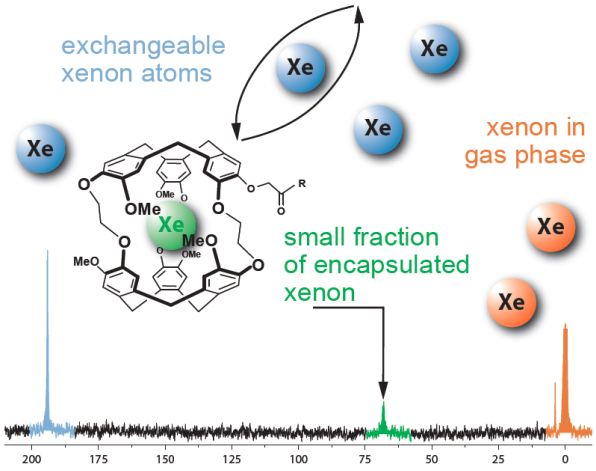

Figure 1.2.6: ^{129}Xe chemical shift diversity in differing media [91]

In order to further increase the signal-to-noise ratio, Schröder et al. developed a methodology called hyper-chemical exchange saturation transfer (Hyper-CEST) in 2006.[96]

Hyper-CEST The principle utilizes hp ^{129}Xe that is caged by Cryptophane-A, and that therefore experiences a different chemical shift apart from free xenon atoms, to selectively depolarize xenon atoms within the cage by irradiation of the probe at the caged xenon frequency, also called selective saturation. Since xenon atoms bind reversibly to the cage, xenon atoms diffuse into the cage at a polarized state and diffuse out of the cage

in a depolarized state, due to the long relaxation time of hp xenon $T_1 \approx 66$ s in water with a fast exchange rate of xenon in the Cryptophane-A cage of $\tau_{ex} \approx 40$ ms. If the Cryptophane-A probe localizes at a specific compartment due to target interaction, then Hyper-CEST yields an accumulation of depolarized xenon at the specified compartment (Figure 1.2.7).[96]

However, the extinction of a signal is difficult to image, whereas a change in signal can be highlighted by subtraction of two spectra, one before selective saturation and one after (Figure 1.2.8a). In this way, a strong, selective signal is generated with almost zero background, ideal for the detection of molecular imaging probes *in vivo* (Figure 1.2.8).

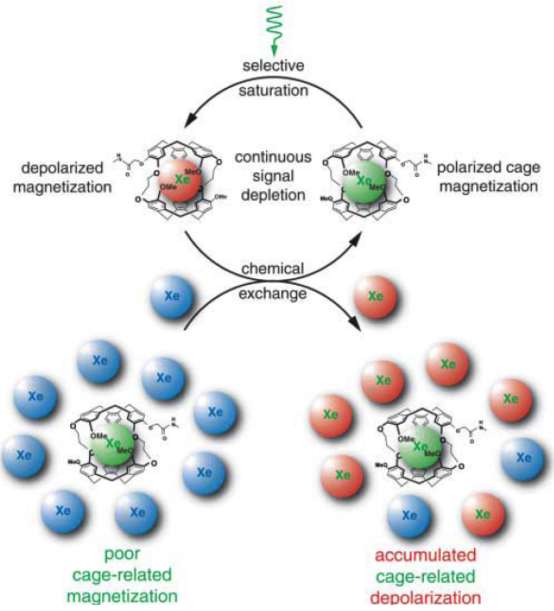

Figure 1.2.7: Selective saturation of hp ^{129}Xe [96]

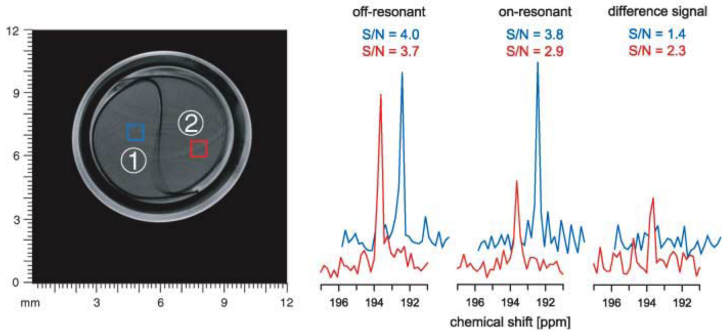

(a)

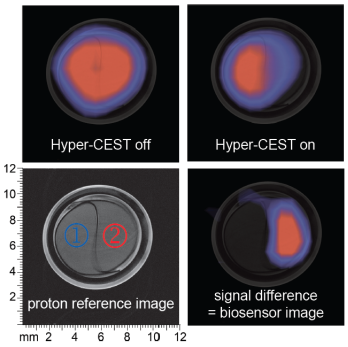

(b)

Figure 1.2.8: Hyper-CEST demonstration of signal enhancment for *in vivo* imaging applications [96] a) left: Phantom with 2 chambers, left chamber without Cryptophane-A targeting solution, right chamber with Cryptophane-A targeting solution; right: Signal substraction after Hyper-CEST results in a single signal (difference signal); b) Images resulting from hp ^{129}Xe measurements; upper left: Hyper-CEST off; upper right: signal depletion in Cryptophane-A targeted chamber; lower right: calculated signal difference clearly mapping Cryptophane-A presence in the right chamber of the phantom

2 Aim of Thesis

Due to lack of symptoms for pancreatic cancer and its poor survival rate of 6 % over 5 years, early diagnostic tools are desperately needed in order to detect early stages of pancreatic cancer — preferably before a tumor has grown. Targeted optical imaging probes allow tracing of potential pancreatic ductal adenocarcinoma (PDAC) biomarkers at protein expression levels and enable detection of early stage lesions that lead to invasive adenocarcinomas.

Therefore, aim of this thesis was the development of optical tracers for pancreatic cancer that target an identified and evaluated, specific PDAC biomarker. Furthermore, investigation of the designated optical imaging probes should clarify fluorescence properties, activity, selectivity and cellular effectiveness.

3 Results and Discussion

3.1 Previous Work and Validation

3.1.1 Target Identification

For the early detection of pancreatic cancer a biomarker needed to be identified. A gene up-regulated in early stages of tumor development as well as in the tumor itself but not expressed or down-regulated in normal tissue or inflammatory tissue would provide an ideal target for early diagnosis.
Therefore, in order to identify biomarkers for pancreatic cancer, Prof. Stephan Hahn from the Ruhr-University Bochum initiated a database research for genes overexpressed in pancreatic ductal adenocarcinoma (PDAC). A list of 3700 genes was generated by applying a literature search from 1965 to 2006 for all genes reported to be overexpressed in pancreatic cancer (Figure 3.1.1). A sublist, containing genes overpressed in PDAC and/or in pancreatic intraepithelial neoplasia (PanIN) stages 2 and 3, but excluding all genes overexpressed in acinar cells, yielded 1895 genes. This sublist was filtered for extracellular matrix or membrane genes, genes from the cytoplasm, and genes with very high differential expression ratio reducing the sublist to 536 genes. The "Top 536 gene list" was then adjusted by excluding all genes over-

expressed in inflammatory pancreas, so-called pancreatitis, so as to be able to distinguish between mostly pancreatitis-related PanIN 1 and high risk-lesions PanIN 2 or 3. This dataset was provided by Bayer Schering Pharma AG and was generated by Affymetrix arrays (including cDNA, aRNA arrays or by immunohistochemical stainings). Finally, a selection of 16 biomarkers including receptors, proteases and transmembrane proteases was obtained in cooperation with Prof. Stephan Hahn and Bayer Schering Pharma AG. All selected genes were validated via immunohistochemical stainings carried out by Prof. Bence Sipos from Prof. Günther Klöppel's group from the University Kiel.

Focus was set on drugable targets that can be addressed via small synthetic molecules. Therefore, all receptors were eliminated for target approach, since they are usually multimeric constructs of proteins resulting in large contact surfaces that are not likely to react with small synthetic tracers. Ideally, secreted proteases pose interesting targets. Since these enzymes accumulate throughout the extracellular matrix (ECM), compounds do not have to overcome the cell membrane thereby simplifying the targeting process.
Therefore, matrix metalloprotease 11 (MMP-11) was chosen as a priority target (Figure 3.1.1).

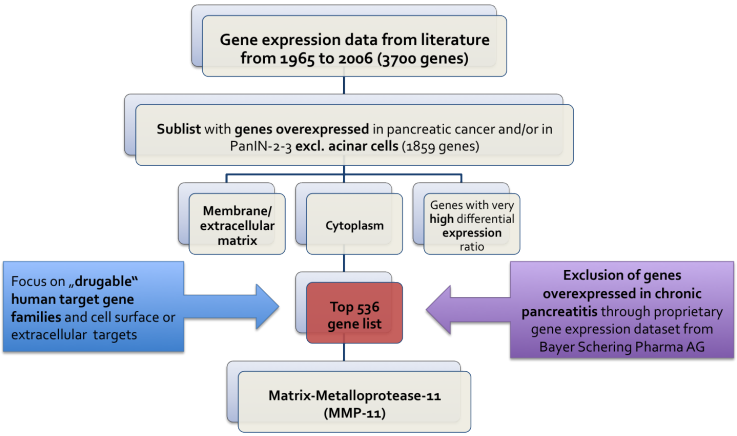

Figure 3.1.1: Target Identification Pathway

MMP-11 is activated intracellularly and is then secreted to the ECM.[61] It is literature-known for up-regulation in for example breast tumors, tumors of the head and neck, and pancreatic cancer.[97, 98, 67] It enables straightforward access for synthetic molecules, due to its catalytic zinc center that can be easily adressed with hydroxamate inhibitors or peptidic substrates, chelating the catalytic zinc ion.[65] Furthermore, its catalytic preference for unnatural amino acid containing substrates distinguishes MMP-11 from other metalloproteases and allows a targeted approach for early diagnosis of pancreatic cancer.[99]

3.1.2 Biomarker Validation

In order to confirm MMP-11 as a biomarker for pancreatic cancer, pancreatic tumor tissues from patients (provided from Prof. Günter Klöppels group, University Kiel) were tested for their

MMP-11 expression in a Western Blot. Pancreatic tumor tissues (N= 8) and normal tissue samples (N=8) were sliced and lysed. Equal amounts of sample were applied to an SDS-gel. The proteins were separated via electrophoresis and transferred to a PVSF membrane, which was stained with an MMP-11 antibody. A horseradish peroxidase (HRP) labeled secondary antibody was used for the detection of anti-MMP-11 antibody. The blot showed strong expression in ductal adenocarcinoma (DAC) while hardly any MMP-11 expression was observed with normal pancreatic tissue (Figure 3.1.2a). Furthermore, the blots were quantified due to luminescent intensity of the corresponding MMP-11 specific bands. A t-test for statistical significance with a 95 % confidence interval resulted in a confirmative very significant difference of tumorous vs normal expression levels of MMP-11 (P=0.0027) (For significance determination, see table 5.3.1 on page 231).

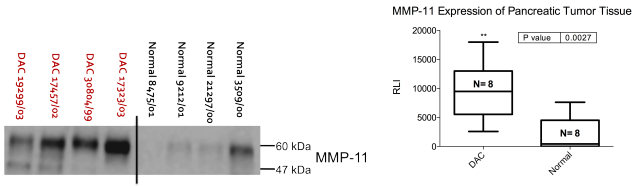

(a) MMP-11 Western Blot (b) Quantitative Validation

Figure 3.1.2: Patient's PDAC and normal tissue tested in Western Blot

3.1.3 FRET-Substrates as MMP-11 Imaging Tools

However, staining experiments with MMP-11 overexpressing cells (MCF-7) with fluorophore-labeled antibodies were unsuccessful. (Data not shown) Expression levels of MMP-11 were too low in order to detect them visually. Signal amplification was therefore essential to image MMP-11 expression in living cells. Targeting of MMP-11 was therefore approached via imaging substrates. The cleavage of the substrate can be exploited to produce a visually detectable signal that is amplified, the more substrate is cleaved. Förster resonance energy transfer (FRET) was chosen as a signal generation method for optical detection. Due to the spectral overlap of emission of donor fluorophore and absorption of an acceptor molecule, fluorescence is quenched in intact substrates, whereas upon cleavage, fluorescence is emitted at the emission wavelength of the donor fluorophore as described in section 1.2.1.1 on page 47.

A number of commercially available FRET-substrates for MMP detection are currently on the market. Most of these substrates employ a 7-methoxycoumarin-4-acetamide (Mca) - dinitrophenyl (Dnp) FRET pair. The excitation and emission wavelengths for coumarin labeled substrates are 325 nm and 395 nm, respectively. Unfortunately, excitation at 325 nm results in autofluorescence of cellular components like mitochondria and lysosomes but also of collagene located within the extracellular matrix.[100] Therefore, coumarin FRET pairs are not suitable for cellular or *in vivo* imaging. FRET substrates labeled with a FRET pair functioning at longer wavelengths are also available, although not for MMP-11. Recently, Novabiochem added a coumarin labeled

sequence Mca-PLA-C(MeOBn)-WARA(Dnp)-NH_2 for MMP-11 cleavage to their products. Novabiochem remains the only distributor with actual activity values (k_{cat}/K_M= 36,000 $M^{-1}s^{-1}$) for their MMP-11 substrate. The sequence is based on the findings of Mucha et al. and will be described in detail in the next section.[99] In summary, commercially available MMP-11 cleavable FRET substrates are rare and employ labels correlating with cellular autofluorescence. Additionally, FRET substrates have never been used to image MMP-11 *in vitro* or *in vivo* before. It was therefore essential to establish MMP-11 cleavable FRET substrates that can be used as imaging tools *in vitro* and *in vivo* to monitor MMP-11 expression and activity in order to provide an early diagnostic tool for PDAC.

3.2 Synthesis

3.2.1 MMP-11 Substrates

Up to this point, only two papers are published concerning MMP-11 substrates. In 1998, Mucha *et al.* published MMP-11 substrate sequences containing unusual amino acids at the P1' position. The P3 to P3' positions were adapted from the earlier established fluorescently quenched metalloprotease sequence Dns-PLA-Xaa-WAR-NH_2 (Figure 3.2.1).[101, 102] The sequences showed high activity towards mouse MMP-11, but unfortunately no selectivity for MMP-11. The most active sequence for MMP-11 containing a methoxybenzyl (MeOBn) protected cysteine at P1' was even 90 times more active for MMP-14.[99] The latter was used as a comparison since MMP-11 and MMP-14 belong to a group of few metalloproteases expressed intracellularly in an active state, due to their furin cleavage site.[61, 103, 104]

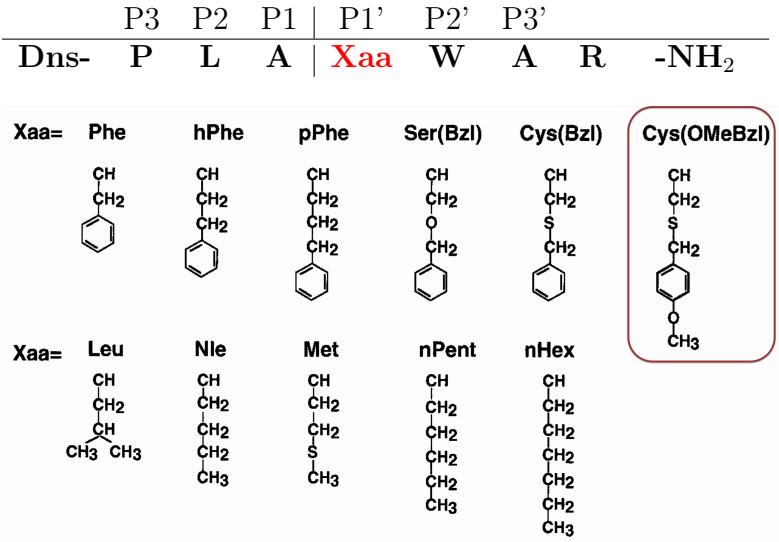

Figure 3.2.1: Unusual amino acids tested in P1' position of MMP-11 substrates [99]

Different residues binding into the S1' pocket of MMP-11 were evaluated. The exchange of leucine in P1' to MeOBn protected cysteine displayed the strongest effect on activity as it tripled the turnover of the substrate for mouse MMP-11 (k_{cat}= 0.033 s^{-1} with K_M= 1.5 μM) and increased k_{cat}/K_M 13-fold to 22,000 $M^{-1}s^{-1}$. However, the same exchange happens to increase the turnover with MMP-14 6-fold (k_{cat}= 4.3 s^{-1} with K_M= 2.79 μM) and therefore, the k_{cat}/K_M value 30-fold to 1,541,218 $M^{-1}s^{-1}$ (Figure 3.2.2).

The sequences presented are FRET substrates, using tryptophane as a fluorophore and the dansyl (5-(dimethylamino)naphthalene-1-sulfonyl (Dns)) residue as a quencher. Unfortunately, background fluorescence of these substrates was disturbingly strong,

so that activity measurements had to be carried out via HPLC assay rather than a FRET assay.[99] Moreover, the low emission wavelength of tryptophane correlates with autofluorescence from living cells and is therefore not applicable for cellular imaging.

Furthermore, Pan *et al.* identified substrate sequences, cleaved by human MMP-11, using a phage display library setup in 2003.[64] The sequences occupied a leucine in the P1' position and varied the P3 to P3' positions. The sequences were not as active as the ones from Mucha *et al.*, which may be due to the fact that Pan *et al.* addressed human MMP-11, which is less active than mouse MMP-11 due to its Pro239 mutation.[64] However, sequences published by Pan *et al.* displayed a 10-fold selectivity for human MMP-11 when compared to MMP-14. Peptides MA15 and MA18 from figure 3.2.3 showed moderate activity with k_{cat}/K_M= 710 $M^{-1}s^{-1}$ and k_{cat}/K_M= 2030 $M^{-1}s^{-1}$, respectively. The substrate's K_M values were located in the high micromolar range (K_M=705 μM and K_M=207 μM, respectively) which was probably the reason for the low overall activity of these substrates.
Additionally, these sequences were not labeled with any fluorophores suggesting that labeling modifications of the bare sequences may influence activity and most importantly selectivity for MMP-11.

3.2.2 FRET Substrate Library Preparation

3.2.2.1 Library Construction

In order to combine high activity with selectivity for *in vitro* and *in vivo* imaging substrates, a combinated peptide substrate

Comparison of the MT1-MMP and ST3 specificity

Assays were carried out in 50 mM Tris/HCl, pH 7.5, 10 mM $CaCl_2$, in the presence (ST3) or absence (MT1-MMP) of 200 mM NaCl.

Substrates	k_{cat}/K_m	
	MT1-MMP	ST3
	$M^{-1}\,s^{-1}\,(10^4)$	
Dns-Pro-Leu-Ala-Cys(OMeBzl)-Trp-Ala-Arg-NH_2	159 ± 0.44	1.67 ± 0.04
Dns-Pro-Leu-Ala-Cys(Bzl)-Trp-Ala-Arg-NH_2	65 ± 0.32	1.12 ± 0.09
Dns-Pro-Leu-Ala-Ser(Bzl)-Trp-Ala-Arg-NH_2	25 ± 0.05	0.70 ± 0.01
Dns-Pro-Leu-Ala-pPhe-Trp-Ala-Arg-NH_2	24 ± 0.07	0.18 ± 0.009
Dns-Pro-Leu-Ala-hPhe-Trp-Ala-Arg-NH_2	9.5 ± 0.06	0.27 ± 0.03
Dns-Pro-Leu-Ala-nHex-Trp-Ala-Arg-NH_2	6.3 ± 0.04	0.001 ± 0.004
Dns-Pro-Leu-Ala-Leu-Trp-Ala-Arg-NH_2	4.2 ± 0.03	0.18 ± 0.0015
Dns-Pro-Leu-Ala-Met-Trp-Ala-Arg-NH_2	3.6 ± 0.03	0.52 ± 0.006
Dns-Pro-Leu-Ala-nPent-Trp-Ala-Arg-NH_2	3.1 ± 0.02	0.30 ± 0.005
Dns-Pro-Leu-Ala-Nle-Trp-Ala-Arg-NH_2	1.8 ± 0.01	0.13 ± 0.005
Dns–Pro-Leu-Ala-Phe-Trp-Ala-Arg-NH_2	1.1 ± 0.01	0.02 ± 0.006
Dns–Pro-Leu-Phe-Cys(Bzl)-Trp-Ala-Arg-NH_2	<1	0.52 ± 0.03
Dns–Ala-Ala-Ala-Cys(Bzl)-Trp-Ala-Arg-NH_2	<1	0.90 ± 0.02

TABLE II

Kinetic parameters for the hydrolysis by MT1-MMP and ST3 of substrates containing a Cys(OMeBzl) or Leu side chain in their P_1' position

Substrate	MT1-MMP			ST3		
	K_m	k_{cat}	k_{cat}/K_m [a]	K_m	k_{cat}	k_{cat}/K_m [a]
	μM	s^{-1}	$M^{-1}\,s^{-1}$	μM	s^{-1}	$M^{-1}\,s^{-1}$
Xaa = Cys(OMeBzl)	2.79 ± 0.8	4.3 ± 0.7	1541218	1.5 ± 0.17	0.033 ± 0.003	22000
Xaa = Leu	13.7 ± 0.32	0.73 ± 0.01	53284	6.8 ± 1.1	0.011 ± 0.001	1617
$\Delta\Delta G^{\ddagger}$ [b] Leu → Cys(OMeBzl)		2.00 kcal/mol			1.55 kcal/mol	

[a] Calculated from the ratio of the k_{cat} and K_m values.
[b] $\Delta\Delta G^{\ddagger} = RT \ln[(k_{cat}/K_m)_{Cys(OMeBzl)}/(k_{cat}/K_m)_{Leu}]$, $T = 298K$.

Figure 3.2.2: Comparison of unusual amino acid containing sequences for MMP-11 [99]

Catalytic properties of peptides with MMP-14 and MMP-11

Peptide		k_{cat}/K_M			
Number	Sequence	MMP-14	MMP-11	MMP-11-A235P	MMP-11-E216A
			$_M^{-1}\,s^{-1}$		
MA13	GGPLG↓LYAGG	16,000	<20	<20	<20
MA15	GGAAN↓LVRGG	<200	710	2,900	<20
MA18	GGYAE↓LRMGG	<200	2,030	20,800	<20
MA16	GGQPRG↓VWGG	6,100	<20	<20	<20
MA17	GGTDA↓WLSGG	<200	<20	<20	<20
MA20	GGPLA↓LWARG	7,400	<20	70	<20
MA21	GAAGA↓MFLEA	<200	70	350	<20

Figure 3.2.3: Substrate sequence comparison of Phage Display sequences [64]

library was prepared. MeOBn protected cysteine was used in P1' position inspired from Mucha *et al.* (entry 3 in table 3.2.1) to enhance activity with MMP-11. Positions P3 to P3' were varied with combinations of the original metalloprotease sequence (entry 3) and combinations from the phage display sequence by Pan *et al.* (entry 1 and 2) to increase selectivity for MMP-11, as shown in table 3.2.1. The variation yielded 15 different sequences and 1 additional negative control (entry 16, table 3.2.2) that were evaluated and compared. Leucine analogs of all sequences were included as activity controls. Two glycines flanking each side of the recognition sequence were adopted as spacers for the fluorophores from Pan *et al.* Sequences adapted from the literature are highlighted in gray (Table 3.2.2).

Entry	Sequence	k_{cat}/K_M (MMP-11) ($M^{-1}s^{-1}$)	K_M (MMP-11) (μM)	k_{cat} (MMP-11) (s^{-1})	Selectivity for MMP-11	Selectivity for MMP-14
1	GGYAELRMGG	2030	207	0.58	10	
2	GGAANLVRGG	710	705	0.69	4	
3	Dns-PLAC(OMeBn)WAR-NH_2	22000 15000	1.5 5.2	0.033 0.078		90 47

Table 3.2.1: Sequence combination to yield substrates with high activity and selectivity for MMP-11 [99, 64, 55]

Entry	Sequence
1	GGAANC(MeOBn)RMGG
2	GGYAEC(MeOBn)RMGG
3	GGAANLRMGG
4	GGYAELRMGG
5	GGAANC(MeOBn)VRGG
6	GGYAEC(MeOBn)VRGG
7	GGAANLVRGG
8	GGYAELVRGG
9	GGPLAC(MeOBn)WARGG
10	GGAANC(MeOBn)WARGG
11	GGYAEC(MeOBn)WARGG
12	GGPLALWARGG
13	GGAANLWARGG
14	GGYAELWARGG
15	GGNAAC(MeOBn)RMGG
16	GGYAENGG

Table 3.2.2: Sequence library of peptidic substrates for MMP-11; Gray rows display sequences adopted from the literature

3.2.2.2 Synthesis of FRET Substrate Library

Nazarenko *et al.* demonstrated in 1997 the successfull synthesis of dabcyl-quenched fluorescein labeled hairpin primers with a signal-to-background ratio of 35:1 for the direct detection of PCR-amplified DNA.[83] Dabcyl (4-(4'-(dimethylamino)phenylazo)benzoic acid) belongs to the dark quenching acceptors for FRET with an excitation decay of molecular vibration (heat) instead of light. Therefore, in order to prepare dark quenched FRET substrates for MMP-11, fluorescein was chosen as the donor and dabcyl as an acceptor chromophore.

Synthesis of the peptide library was accomplished employing solid phase synthesis.

Uryga-Polowy *et al.* established a C-terminal fluorescein labeling of peptides in 2009.[105] This labeling method allows straighforward synthesis of the peptides on solid phase and would simplify introduction of the quencher moiety for the generation of FRET substrates. Applying this methodology, the fluorophore is attached to the backbone, rendering it rigid, whereas the quencher is attached to the sidechain of the peptide, making the residue highly flexible. This strategy facilitates the right spatial orientation of fluorophore and quencher to enhance the quenching effect of FRET. Fluorescein-labeled polystyrol 2-chlorotrityl resin was prepared as described previously by Uryga-Polowy *et al.* (Figure 3.2.4).

First, phenolic hyroxy groups of 5-aminofluorescein **1** were protected with pivaloyl anhydride, followed by Fmoc (9-Fluorenylmethoxycarbonyl) protection of the anilic amine in *ortho*-position. 5-aminofluorescein was chosen because of its superior reactivity to 6-aminofluorescein that is slightly deactivated due to the mesomeric electron withdrawal in para position. The pivaloyl protecting groups were then deblocked under acidic conditions and the 5-Fmoc-aminofluorescein was loaded onto 2-chlorotrityl chloride resin to yield C-terminally labeled fluorescein-trityl resin **5**. Since one of the phenolic hydroxy groups is attached to the resin, the other one needs to be protected to prevent side reactions. It was therefore protected with MEM chloride (2-Methoxyethoxymethyl chloride) to yield **6**. The Fmoc group was deprotected and the fluorescein-labeled resin **7** was used for peptide construction.

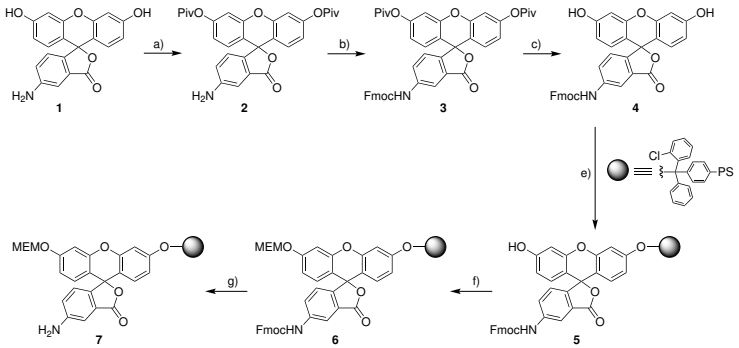

Figure 3.2.4: Preparation of C-terminally labeled fluorescein resin for solid phase peptide synthesis as described by Uryga-Polowy et al.[105] Conditions: a) Piv_2O, Cs_2CO_3, DMF, RT, 90 min, 96%; b) Fmoc-Cl, NaOH, THF, 0°C, 16 h, 84%; c) 95% TFA in H2O, 60°C, 120 min, 92%; d) Fmoc-Cl, NaOH, THF, 0°C, 16 h, 40 %; e) 2-chlorotrityl chloride resin, DIPEA, DCM/DMF, RT, 180 min; f) MEM-Cl, DIPEA, DMF, RT, 90 min; g) 20% piperidine in DMF, RT, 2 x 10 min

The prepared resin **7** was used to synthesize all fluorescein-labeled FRET substrates used later on. 58 % loading efficiency was measured via UV mediated Fmoc-determination, representing a 25 % coupling increase in comparison to published data.

Since the anilic amine of fluorescein has reduced coupling reactivity, the first coupling of glycine to the resin-bound fluorescein was carried out with 5 eq of glycine, 5 eq HATU (O-(7-azabenzotriazol-1-yl)-N,N,N',N'-tetramethyluronium hexafluorophosphate) and 10 eq of collidine (2,4,6-trimethylpyridine) for 3 h at room temperature (RT) twice, resulting in 96 % coupling yield.

The following couplings for sequence generation were proceeded using standard Fmoc strategy peptide couplings, using 3 eq of each amino acid, HOBt (1-hydroxybenzotriazole), DIC (N,N'-diisopropylcarbodiimide) and 3 eq DIPEA (N,N'-diisopropylethylamine) for 1.5 h at RT. Base was added to all couplings in order to prevent cleavage of the fluorescein from the trityl resin. Deblocking of the Fmoc protection group with 20 % piperidine in DMF two times for 10 min at RT was followed by an additional coupling of the next amino acid. This procedure was repeated for all following couplings.

Dabcyl (4-(4'-(dimethylamino)phenylazo)benzoic acid) was used as a quencher and was purchased as a Fmoc-L-lysine(dabcyl)-OH conjugate. It was coupled to the peptide sequence under the previously mentioned conditions. Finally, 3 arginine residues were added to the N-terminus to increase hydrophilicity, since substrate sequences prepared without 3 arginines at the N-terminus were found to be unsoluble under assay conditions (aqueous medium, pH=7.5). An additional glycine was added as a spacer for further modifications (see 3.4 on page 132). The glycine was capped with an acetyl group and the complete sequence was cleaved from the resin employing the cleavage cocktails shown in table 3.2.3 with 40 % TFA (trifluoroacetic acid) for MeOBn protected cysteine containing sequences in P1' position and 90 % TFA for leucine containing substrates.

Since the MeOBn protecting group of cysteine was not to be cleaved, a final TFA concentration of 40 % was not to be transgressed. However, all sequences included three arginines near the N-terminus usually affording 90 % TFA for three hours at RT for N-ω-(2,2,4,6,7-pentamethyldihyrdobenzofuran-5-sulfonyl) (Pbf) cleavage.[106] Therefore, an extension of reaction time to 24 h

at RT was applied. Furthermore, addition of 1 % phenol to the cleavage cocktail was essential in order to scavenge deprotected Pbf groups and therefore impair back-addition of Pbf to the arginines.

Chromatograms recorded after cleavage of 24 h at RT with and without addition of 1 % phenol depict major differences in product yield. Due to 4 arginines within the applied sequence, a product distribution of 5 differently protected and unprotected sequences resulted without the addition of phenol. Figure 3.2.5 shows 254 nm (top) and 500 nm (bottom) chromatograms whereas a) depicts cleavage product without addition of phenol and b) shows the cleavage product with addition of phenol. The desired product has a retention time of 2.76 min and can be clearly seen in the 500 nm chromatogram after cleavage with phenol.

Entry	Cocktail	for C(MeOBn) sequences (%)	for leucine sequences (%)	Reason
1	DCM	50	5	Improves swelling
2	TFA	40	90	Resin cleavage
3	H_2O	4	2	Scavenger for ^{t}Bu
4	Phenol	1 (w/v)	1 (w/v)	Scavenger for Pbf
5	EDT	2.5	1	Reducing agent
6	TIS	2.5	1	Scavenger for Trt

Table 3.2.3: Cleavage cocktail for peptide substrates applied to the resin for 24 h at RT

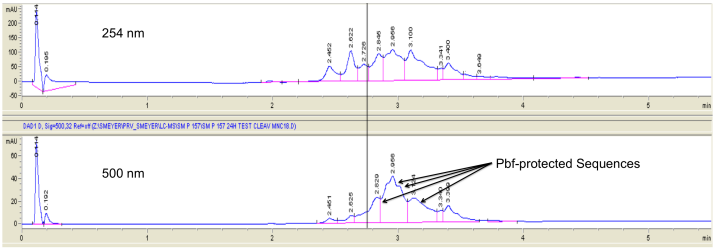

(a) Chromatogram after cleavage without addition of 1% phenol

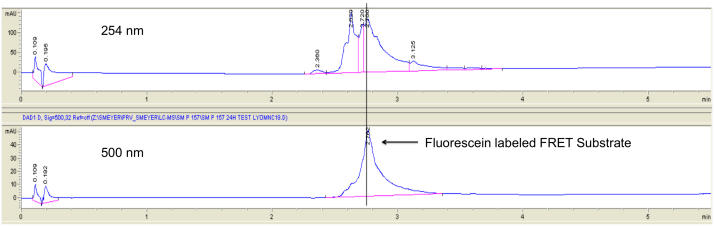

(b) Chromatogram after cleavage with addition of 1% phenol

Figure 3.2.5: Cleavage condition comparison with and without addition of 1% phenol

All substrates were isolated via reverse phase HPLC (see 5.1 on page 209). Yields are given in table 3.2.5. Purities were determined with LC/MS-TOF measurements. Chromatograms can be found in the appendix 6 on page 235. Additionally, recorded HR-MS values are listed on page 221.

Entry	FRET-Substrates and Fluorescence Standards	Yield (crude) %	Yield (%)	Name
1	Ac-GRRRK(Dabcyl)GGAAN-C(MeOBn)RMGG-Fluo	21	6	SM P 124
2	Ac-GRRRK(Dabcyl)GGYAE-C(MeOBn)RMGG-Fluo	31	7	SM P 127
3	Ac-GRRRK(Dabcyl)GGAAN-LRMGG-Fluo	34	6	SM P 130
4	Ac-GRRRK(Dabcyl)GGYAE-LRMGG-Fluo	50	17	SM P 133
5	Ac-GRRRK(Dabcyl)GGAAN-C(MeOBn)VRGG-Fluo	25	3	SM P 148
6	Ac-GRRRK(Dabcyl)GGYAE-C(MeOBn)VRGG-Fluo	40	6	SM P 151
7	Ac-GRRRK(Dabcyl)GGAAN-LVRGG-Fluo	41	7	SM P 154
8	Ac-GRRRK(Dabcyl)GGYAE-LVRGG-Fluo	33	8	SM P 157
9	Ac-GRRRK(Dabcyl)GGPLA-C(MeOBn)WARGG-Fluo	65	11	SM P 166
10	Ac-GRRRK(Dabcyl)GGAAN-C(MeOBn)WARGG-Fluo	48	5	SM P 169
11	Ac-GRRRK(Dabcyl)GGYAE-C(MeOBn)WARGG-Fluo	51	7	SM P 172
12	Ac-GRRRK(Dabcyl)GGPLA-LWARGG-Fluo	42	19	SM P 175
13	Ac-GRRRK(Dabcyl)GGAAN-LWARGG-Fluo	46	18	SM P 178

14	Ac-GRRRK(Dabcyl)GGYAE-LWARGG-Fluo	39	10	SM P 181
15	Ac-GRRRK(Dabcyl)GGNAA-C(MeOBn)RMGG-Fluo	23	8	SM P 125
16	Ac-GRRRK(Dabcyl)GYAENG-Fluo	59	26	SM P 123
17	Ac-C(MeOBn)RMGG-Fluo (Fluorescence Standard)	71	32	SM CM
18	Ac-C(MeOBn)VRGG-Fluo (Fluorescence Standard)	48	48	SOM 9
19	Ac-C(MeOBn)WARGG-Fluo (Fluorescence Standard)	53	5	SOM 11
20	Ac-LRMGG-Fluo (Fluorescence Standard)	30	30	SOM 5
21	Ac-LVRGG-Fluo (Fluorescence Standard)	48	48	SOM 8
22	Ac-LWARGG-Fluo (Fluorescence Standard)	39	8	SOM 10

Table 3.2.5: Yields from substrate library, sequences adapted from the literature are highlighted in gray

The average crude yield for the substrate synthesis is 42 %. A main factor for the low yields is the lability of the fluorophore attachment to the trityl resin. Yellow coupling solutions were often observed 1 h after coupling cocktail application, indicating partial detachment of the peptide sequence. Introduction of a

linker system for fluorescein attachment to the resin **9** might relieve the strong steric hinderance between 2-chlorotrityl resin and fluorescein **8** and might therefore increase peptide synthesis yield (Figure 3.2.6).

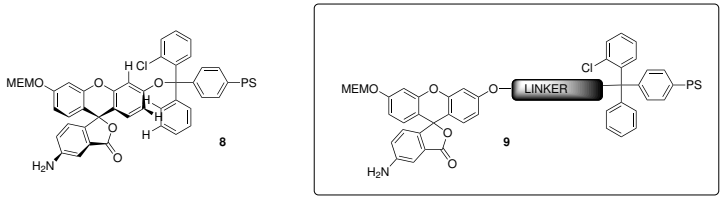

Figure 3.2.6: Linker approach for C-terminal fluorescein labeling

Moreover, sequences without MeOBn protected cysteine resulted in better yields, due to better cleavage conditions of 90 % TFA ensuring Pbf deprotection. The length of the peptide also influences the yield, with shorter peptides resulting in higher yields. Substrate sequences representing MMP-11-cleaved sequences were synthesized as fluorescent standards for the *in vitro* evaluation of the FRET assay. Fluorescent standard peptides were synthesized with an average yield of 48 %, with the advantage that some of the sequences were obtained with 98 % purity and were used without further purification. Reasons for yield diminishment after HPLC purification include isolation of different oxidation states of sulfur-containing peptides, as well as isolation of sequences with one or more Pbf protection group still attached.

The general structure of the substrates **10** is depicted in figure 3.2.7. The fluorescein label is shown in orange, the dabcyl quencher in red, hydrophilicity adjustments in blue, whereas the recognition sequence for MMP-11 is represented in green. Pre-

sumably, the MeOBn protected cysteine in P1' binds to the catalytic S1' subsite of the MMP while the carbonylic oxygen of the P1 position coordinates to the catalytic zinc. A catalytic water molecule is needed for insertion in order to hydrolyze the substrate between P1 and P1'.[65]

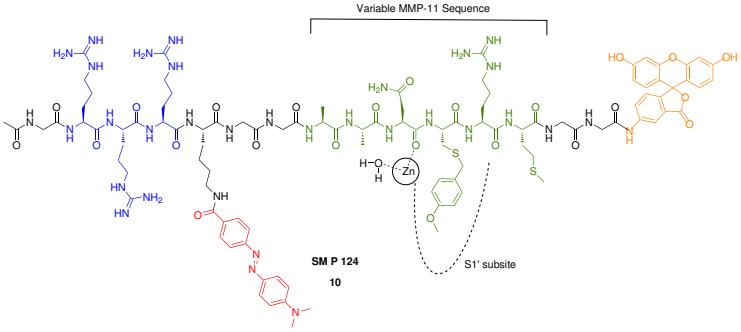

Figure 3.2.7: General substrate structure

Furthermore, in order to compare a commercially available metalloprotease substrate offered by Enzo Life Sciences, Lörrach, the best sequence was also labeled with a AMCA-Dnp (7-Amino-4-methyl-3-coumarinylacetic acid - Dinitrophenyl) FRET pair.
AMCA labeled substrates were synthesized by C-terminal attachment of AMCA to a rink amide resin as published previously by Wood *et al.*[107] Attachment of Fmoc-protected AMCA **12** (Figure 3.2.8) was achieved by coupling with 3 eq of Fmoc-AMCA, HOBt and DIC, each, in DMF for 3h at RT to a Fmoc deprotected Rink amide resin. Fmoc deprotection with 20 % piperidine in DMF yielded the AMCA-labeled resin **14** with a Fmoc determined loading of 95 %. The first coupling, hindered due to the anilic nature of the amine, was performed with 5 eq

of HATU and glycine, each and 10 eq of collidine in DMF for 3h at RT, twice. The loading efficiency was determined to be 94 %. Repeated deblocking and coupling with HOBt and DIC in DMF afforded the AMCA-Dnp quenched FRET peptide substrate. Cleavage from the resin was achieved by employing the cleavage cocktail described in table 3.2.3 on page 75.

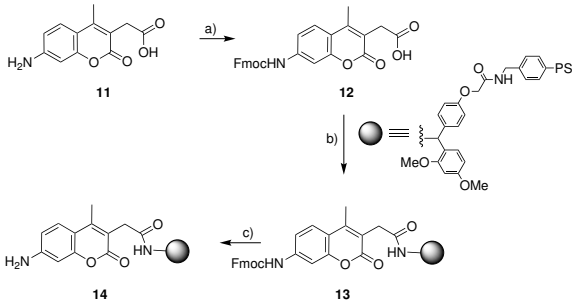

Figure 3.2.8: C-terminal AMCA labeling on Rink amide AM resin; Conditions: a) Fmoc-Cl, $NaHCO_3$, Acetone/H_2O 1:1, RT, 24 h, 85 %; b) Rink amide AM resin, HOBt, DIC, DCM/DMF 1:1, RT, 3h, 95 %; c) 20 % piperidine in DMF, RT, 2 x 10 min

Excitation and emission wavelengths of these substrates are 325 nm and 393 nm, respectively. Hence, as previously mentioned, they cannot be used for live-cell imaging due to autofluorescence correlation of the cells. Table 3.2.6 lists the sequences for this comparison. MMPs cleave entry 1 between glycine and leucine, whereas entry 2 and 4 represent cleaved substrates as fluorescence standards.

Entry	Sequence	Name	Yield crude (%)	Yield (%)
1	Mca-PLGLDap(Dnp)AR-NH_2	OmniMMP^{TM}	-	-
2	Mca-PLG-NH_2	SM P 96	96	89
3	Ac-RRRK(Dnp)GAAN-C(OMeBn)RMG-AMCA-NH_2	SM P 155	40	24
4	Ac-C(OMeBn)RMG-AMCA-NH_2	SM P 93	97	86

Table 3.2.6: Coumarin labeled FRET sequences synthesized

3.2.3 FRET Efficiency

The prepared sequences were evaluated for their fluorescence properties. Excitation and emission spectra were recorded at 485 nm and 525 nm, respectively for fluorescein labeled substrates, and at 325 nm and 393 nm excitation and emission wavelengths for AMCA labeled substrates. Spectra were recorded at a final concentration of 5 μM in Tris-HCl assay buffer, pH= 7.5. Intact FRET substrates of the same concentration show the same absorption values (OD), whereas high quenching efficiency results in low emission values (RFU). Quenching efficiencies depend on the distance between donor and acceptor chromophore and on the peptide sequence, since orientation of the fluorophore to the quencher increases non-radiant transmission of excitation when the members of the FRET pair are aligned at the same angle to each other.
Figure 3.2.9 shows the absorption of the FRET substrate library.

The median absorbance at 5 μM is 0.2. Deviations are caused by measuring inaccuracies of the scale and pipetting errors, due to the very small quantities applied.

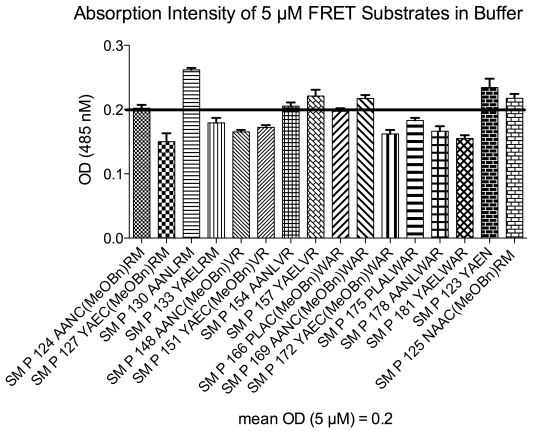

Figure 3.2.9: Absorption intensities at 485 nm

Emission intensities of all intact FRET substrates (black and white), as well as unquenched, cleaved fluorescent standards (colored) were measured and plotted in figure 3.2.10.
Substrate sequences have a major effect on quenching efficiencies, as can be seen by comparison of emission intensities of the different fluorescent standards. The P1' position does not have an effect on fluorescence emission, since no difference is observed between leucine and cysteine containing standards. However, variations of P2' to P4' significantly interfere with the fluorescent signal. Cleaved sequences containing the WAR motif (green bars), for instance, are 1.6 times less intensive in their fluorescence emission. This is probably due to quenching effects of

tryptophan, correlating with the attached fluorescein as has been evaluated by Togashi *et al.*[108] It is believed that tryptophan protonates the fluorescein-dianion at pH= 7.4, thereby lowering fluorescence emission, induced by less efficient electron delocalization of the xanthene system.

Furthermore, amino acids in positions P1-P3 of intact FRET sequences strongly affect quenching efficiency. Quenching works very efficiently with sequences containing RM in positions P2' and P3' and containing a AAN or YAE motif in P3 to P1 (SM P 124, SM P 130, SM P 127, SM P 133). The fluorescent signal is reduced from 2000 RFU to about 50 RFU. Quenching of FRET substrates with a WAR motif in P2' to P4' and containing PLA in positions P3 to P1 (SM P 166, SM P 175) exhibit a fluorescence decrease by a factor of 17. This decrease maybe due to a better orientation of quencher to fluorophore, since proline induces a kink to the backbone, due to its cyclic residue, and because exchange of the P3-P1 motif to YAE (SM P 172, SM P 181) reduces the signal only 10-fold, whereas application of AAN in these positions (SM P 169, SM P 178) only results in a 6-fold quenching.

Moreover, comparison of FRET efficacy of substrates containing a VR motif in P2' to P3' yields even less efficient quenching, as full sequences are decreased 5-fold with a AAN motif in P3 to P1 (SM P 148, SM P 154) and only 3-fold with a YAE motif (SM P 151, SM P 157).

In summary, highest quenching efficiencies, with a 35-fold signal reduction, were observed with substrates SM P 124, SM P 127, SM P 130, and SM P 133, containing a RM motif in P2' and P3' and a AAN or YAE motif in positions P3-P1.

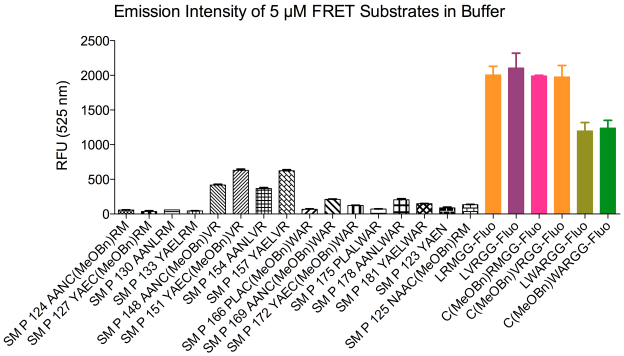

Figure 3.2.10: Emission intensities of prepared FRET-substrates

In order to investigate structural impacts on FRET efficiency, circular dichroism (CD) spectra were recorded to inspect possible secondary structures of the peptides. The peptide sequences did not show any characteristic absorption, suggesting random coil formation, but did show differences that may explain the high variation of emission intensities of prepared FRET substrates. Example spectra for secondary structures such as α-helix and antiparallel β-sheet are presented in figure 3.2.11.[109] Recorded spectra are depicted in figure 3.2.12 showing the complete substrate library and selected substrates with similar FRET efficiency.

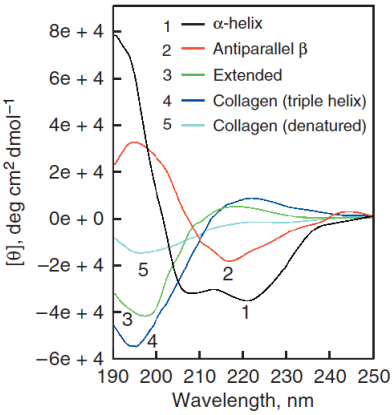

Figure 3.2.11: Example CD spectra of secondary structures types and random coil (denatured) [109]

FRET substrate SM P 130 exhibits typical random coil orientation with an absorption minimum at 195 nm and mean residue ellipticity of about -20,000 deg cm^2 $dmol^{-1}$. Unfortunately, no interconnection between secondary structure and FRET efficiency was observed, when comparing CD spectra of low FRET efficency substrates SM P 151 and SM P 157 with CD spectra of high FRET efficiency substrates SM P 127 and SM P 133, displaying only marginal differences.

Signal output of cleaved and intact FRET substrate SM P 124 dissolved in DMSO (dimethyl sulfoxide) was visualized under a fluorescence microscope. Figure 3.2.13 shows the intact sequence in the upper vessel in orange, whereas the cleaved sequence has a yellow color and a high fluorescent signal when excited at 483 nm and measured at 525 nm.

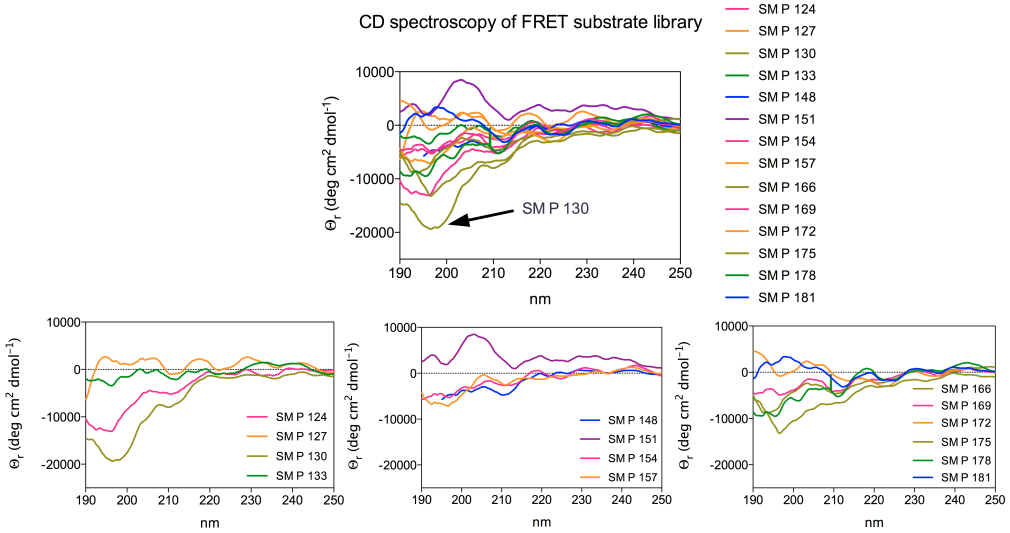

Figure 3.2.12: CD specroscopy of prepared FRET substrate library; Upper row: overlay of all FRET substrates, lower row: sets of sequences with comparable FRET efficiencies

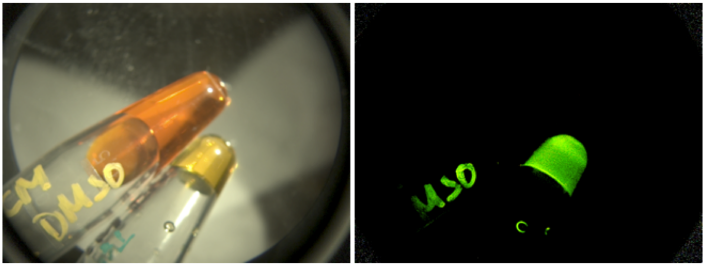

Figure 3.2.13: left: white light image showing intact FRET substrate (orange fluid, upper vessel) and cleaved substrate as fluorescent standard (yellow fluid, vessel below)

Moreover, prepared AMCA substrates were also tested for their quenching efficiency. Emission intensities of quenched substrates in comparison to cleaved fluorescent standard substrates are depicted in figure 3.2.14. The cleaved substrates (green and blue bar) show an overall less intensive signal output of only around 180 RFUs at 5 μM when compared to the high emission of fluorescein-labeled substrates ($\sim$2000 RFU). The C-terminal labeled AMCA substrate also resulted in less emission of the cleaved substrate. However, quenching is very effective, since the signal is nearly completely diminished. No difference of quenching efficacy was observed between C-terminal labeling and N-terminal fluorophore attachment. The prepared AMCA substrate is as efficiently quenched as the commercially available OmniMMP^{TM} substrate; even though the latter shows slightly better emission values, the two coumarin substrates are comparable in their FRET properties.

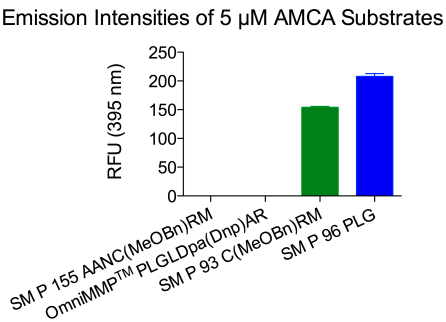

Figure 3.2.14: Emission of Dnp quenched AMCA substrates and cleaved fluorescence standards

3.3 *In vitro* Validation of FRET Imaging Substrates

3.3.1 Activity Determination

MMPs follow first-order Michaelis-Menten kinetics, taking into account the following conditions. The total enzyme concentration, along with the intermediate enzyme-substrate complex concentration, does not change during the course of reaction.[110] The reaction is irreversible and the product does not bind to the enzyme, although it was observed that measurements at high substrate concentrations ($> 20\ \mu$M) lead to substrate inhibition of the enzyme due to some product binding. This effect was only observed with sequences containing unnatural amino acids, suggesting that improved binding to the S1' subsite of the protease results in product binding. However, at smaller concentrations the above-mentioned assumptions are valid and can be described in a formula as follows:

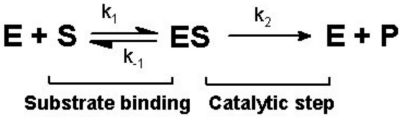

The off-rate k_2 represents in this case also k_{cat} or the turnover number as long as the product formation step is a unimolecular process. It presents the maximum amount of enzyme reactions catalyzed per second. The reaction velocity approaches υ_{max} asymptotically, as depicted in figure 3.3.1; therefore $\frac{1}{2}\ \upsilon_{max}$ is used to determine the affinity constant K_M, also called the

Michaelis constant. K_M is a combination of all rate constants and a measure of substrate concentration at which the protease reaches half maximum reaction rate. It is also an approximation for the substrate affinity. Small K_M values represent high affinity for the enzyme and will reach a saturation of the reaction rate (υ_{max}) more quickly.

$$K_M = \frac{k_{-1} + k_2}{k_1} \tag{3.3.1}$$

The equation above shows that k_{cat} is entangled with K_M, resulting in lower affinities with higher turnover of the enzyme.

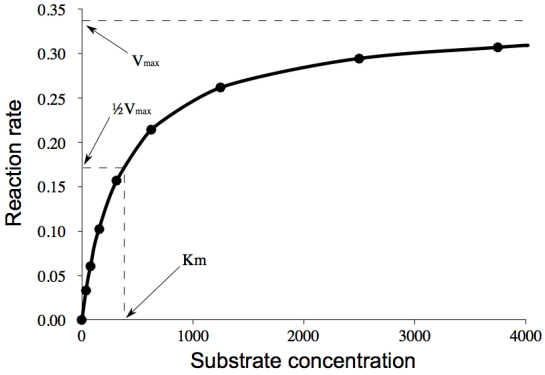

Figure 3.3.1: Michaelis-Menten kinetics of substrate conversion [111]

To determine the K_M and k_{cat} values for the prepared FRET substrates, fluorescence intensities measured by FRET assay were plotted in a fluorescence over time graph as shown in figure 3.3.2. In general, substrate activities are compared using the ratio of

k_{cat} over K_M to take into account the enzyme's activity as well as the affinity for the substrate.

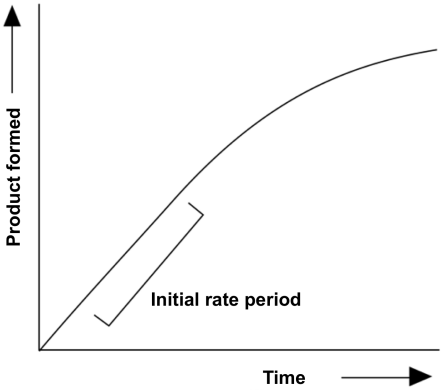

Figure 3.3.2: Fluorescence (Product formed) increase over time with linear inital rate period [112]

The slope of the linear part of evolving fluorescence is equal to the rate of reaction of the protease at that specific substrate concentration.
To determine the activity of the substrate, namely the k_{cat}/K_M value, a new graph is plotted, displaying reaction rate over substrate concentration as shown before in figure 3.3.1. A non-linear regression is fitted to this graph (see 5.3.1 on page 226) to determine K_M and υ_{max}. Finally, k_{cat} can be calculated from the equation below and set into ratio with K_M.

$$k_{cat} = \frac{\upsilon_{max}}{[E_0]} \tag{3.3.2}$$

3.3.1.1 Kinetic FRET Assay

Substrate cleavage was validated for the human recombinant catalytic domain of MMP-11 and MMP-14. The latter was used for comparison in order to be able to further compare results obtained with those published by Mucha *et al.* and Pan *et al.* Both publications used MMP-14 as a second MMP, since both proteases are activated intracellularly and are therefore expressed in an active state.[61]

MMP-11 and MMP-14 were titrated against SM P 124 (AAN-C(MeOBn)RM) prior to measurement of the substrate library to determine protease activity. Unfortunately, MMP-11 activity strongly depends on the delivered batch. MMP-11 is a fragile enzyme, that quickly loses activity upon storage. To stabilize the protein, 1 % BSA was added to stock aliquots and glycol content was increased from 30 % to 50 %. All MMPs used were treated the same way. However, MMP-11 activity varies 10-fold between batches. For this reason, all substrate comparison measurements were performed with the same enzyme batch (batch 3-T7477). Consistently, selectivity measurements were also carried out with one specific batch (batch 3-T7141). Linear regressions and activity values for both enzymes are displayed in figure 3.3.3. Since MMP-14 was determined to be 20 times more active than batch 3-T7477 of MMP-11, 12.5 nM MMP-11 and 0.625 nM MMP-14 resulted in the same activities of the enzymes and where thus applied for all substrate library comparison FRET assays.

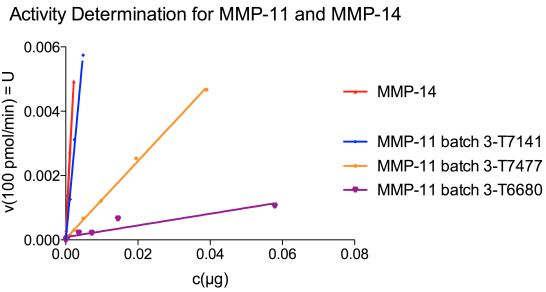

Protease	Activity [U/μg]
MMP-11 batch 3-T7477	0.121 ± 0.002
MMP-11 batch 3-T7141	1.209 ± 0.058
MMP-11 batch 3-T6680	0.018± 0.002
MMP-14 batch 3-T6985	2.222 ± 0.059

Figure 3.3.3: Activity determination of MMP-11 and MMP-14

Measured fluorescence increase over time graphs are depicted below for all substrates for MMP-11 (batch 3-T7477) and MMP-14. Graphs were equally scaled to 3000 RFU for the y-axis and 100 min for the x-axis. Small changes in fluorescence are represented within the graph with smaller scaled graphs.

A major change in fluorescence (up to 1000 RFU) with both proteases is observed with substrate SM P 124. However, SM P 127 and SM P 133 display no deviation from the blank control whereas little increase is observed with SM P 130, also for both proteases (Figures 3.3.4 and 3.3.5).

Furthermore, SM P 148, 151, 154, and 157 show very high fluorescence background activity, since the blank control changes with the same intensity than substrates incubated with enzyme. Moreover, graphs in figures 3.3.6 and 3.3.7 display large devia-

tions of triplicates resulting in error bars with a range of 300-400 RFUs. However, a significant increase of fluorescence apart from the blank control can be observed for substrate SM P 148 for both enzymes and SM P 157 for MMP-11. SM P 151 and SM P 154 were not converted according to the FRET assay employed. Moreover, SM P 166 and SM P 172 display an increase of fluorescence when assayed with MMP-14 or both metalloproteases, respectively. FRET substrates SM P 169 and SM P 175 remained uncleaved (Figures 3.3.8 and 3.3.9).
Negative control substrate SM P 123 was neither cleaved by MMP-11 nor MMP-14, as anticipated (Figure 3.3.11). Unfortunately, SM P 178 and SM P 181 were also not converted (Figure 3.3.10). However, SM P 125 which differs from SM P 124 only by a P1 to P3 exchange in the sequence shows activity with the two proteases, although background fluorescence is twice as high as measured with SM P 124. The change in fluorescence measured over time for all substrates is displayed in the following figures.

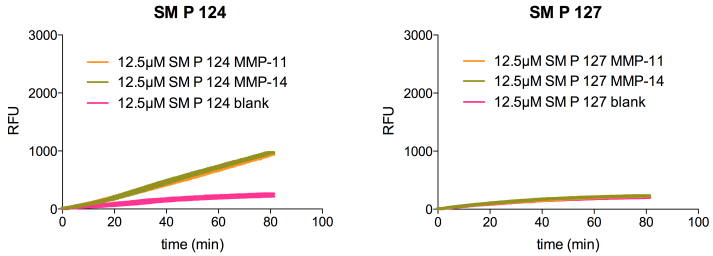

Figure 3.3.4: Fluorescence increase over time of substrates SM P 124 and SM P 127

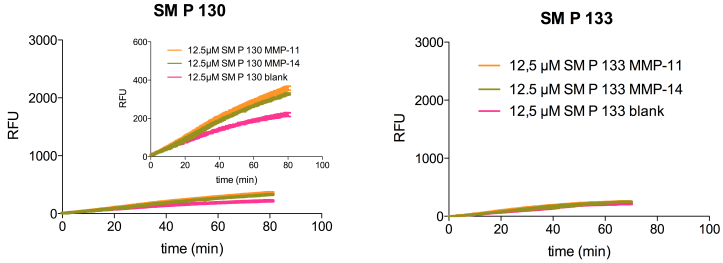

Figure 3.3.5: Fluorescence increase over time of substrates SM P 130 and SM P 133

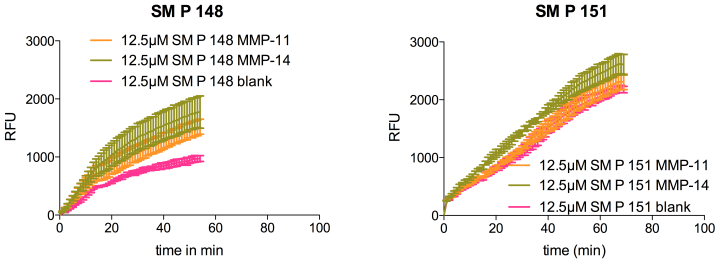

Figure 3.3.6: Fluorescence increase over time of substrates SM P 148 and SM P 151

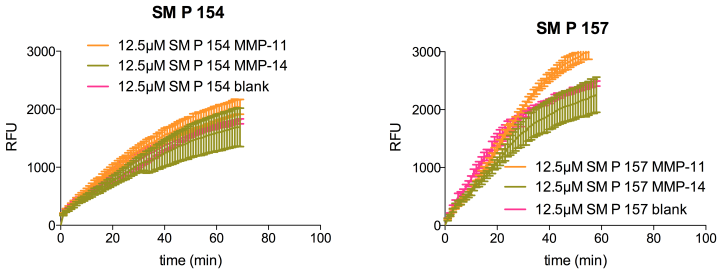

Figure 3.3.7: Fluorescence increase over time of substrates SM P 154 and SM P 157

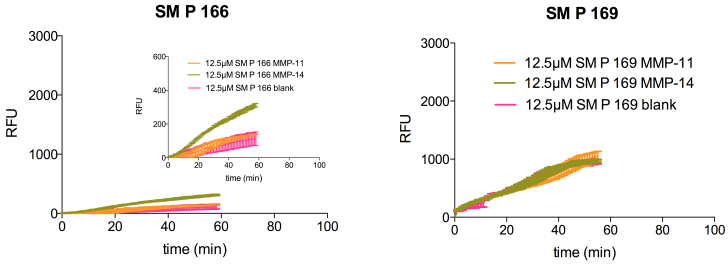

Figure 3.3.8: Fluorescence increase over time of substrates SM P 166 and SM P 169

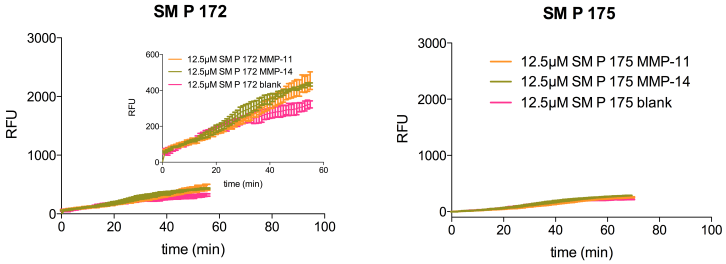

Figure 3.3.9: Fluorescence increase over time of substrates SM P 172 and SM P 175

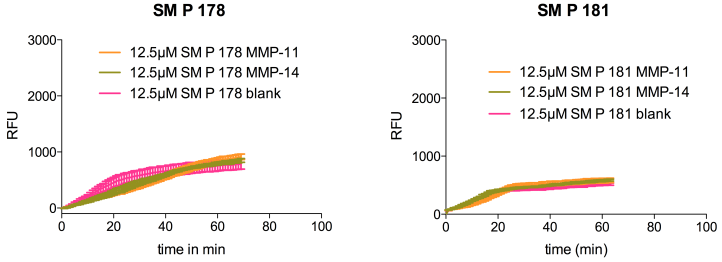

Figure 3.3.10: Fluorescence increase over time of substrates SM P 178 and SM P 181

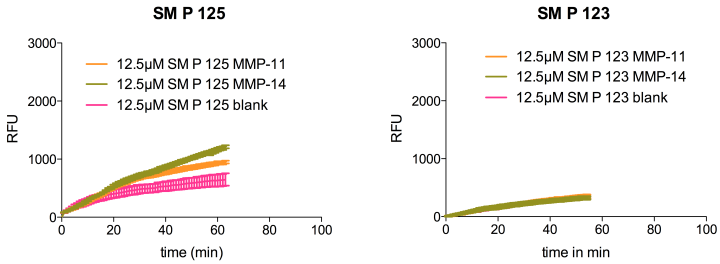

Figure 3.3.11: Fluorescence increase over time of substrates SM P 125 and SM P 123

Additionally, the prepared AMCA substrate was compared to the commercially available OmniMMP^{TM} substrate from Enzo Life Sciences. Change of fluorescence over time revealed substrate conversion for both metalloproteases with substrate SM P 155, but no conversion of OmniMMP^{TM} with MMP-11 (Figure 3.3.12).

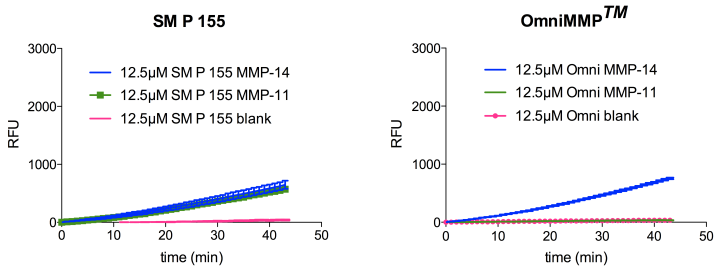

Figure 3.3.12: Fluorescence increase over time with AMCA-labeled substrates SM P 155 and commercially available OmniMMP^{TM}

Interestingly, sequences adapted from the literature (SM P 133, SM P 154, SM P 166) showed no activity when exposed to MMP-11. In particular, SM P 166 (PLAC(MeOBn)WAR) that has been published as a dansyl-tryptophan FRET substrate by Mucha et al. and which is commercially available as a coumarin labeled FRET substrate for MMP-11 by Novabiochem showed no activity with MMP-11 but only with MMP-14 when labeled with a fluorescein FRET pair (see table 3.2.1 on page 69 for literature values). These findings indicate the challenge in preparing highly active fluorescein labeled FRET substrates for MMP-11 that can be employed for imaging purposes, since combination of published MMP-11 sequences to a 16 membered library yielded only 6 sequences showing fluorescence increase and therefore potential substrate cleavage with MMP-11.

3.3.1.2 LC/MS-TOF Validation

Due to high background fluorescence of some of the substrates, a secondary assay was used to confirm substrate cleavage. Results from FRET assays were confirmed by analyzing the reaction mixture via LC/MS-TOF. Samples were measured about 90 min after addition of enzyme to the substrates. MS-TOF was used to identify cleaved substrates by mass and to assign the corresponding peaks in the chromatograms. Control chromatograms show the substrate without enzyme in assay buffer. LC/MS-TOF chromatograms confirmed assay results measured by change of fluorescence from FRET-assays. Conversion of the substrates yielded an additional peak at about 10.4 min retention time. No change in chromatograms was observed with uncleaved substrates. Single oxidized but intact substrate is observed at 11.6 min aquisition time. Corresponding example spectra are shown in figure 3.3.13 for non-converting substrates like SM P 127, while figure 3.3.14 presents results for cleaved substrates like SM P 124. Further LC/MS-TOF chromatograms of the performed FRET assays can be found in the appendix on page 239. Chromatograms were recorded at 500 nm, therefore, only dabcyl-labeled cleavage product is visible (peak at 10.4 min, figure 3.3.14), despite of evolving fluorescein-labeled product with lower absorption intensity.

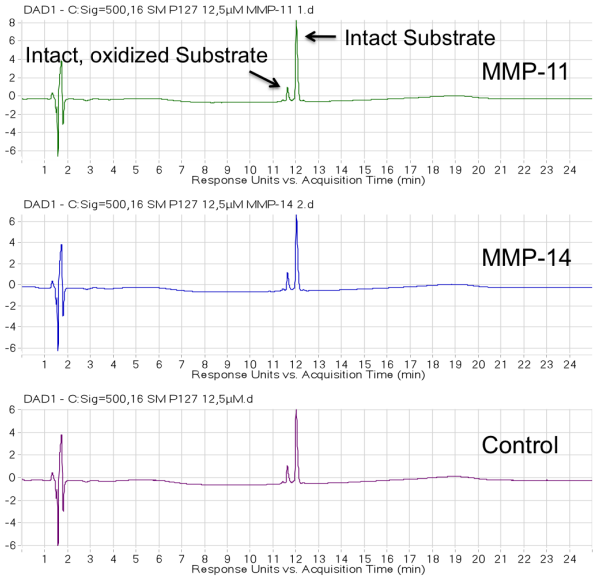

Figure 3.3.13: Chromatograms of non-converted FRET substrate SM P 127 incubated with MMP-11 (top), MMP-14 (middle), and without enzyme (bottom); small peak at 11.6 min represents single oxidized intact substrate, no substrate cleavage was observed

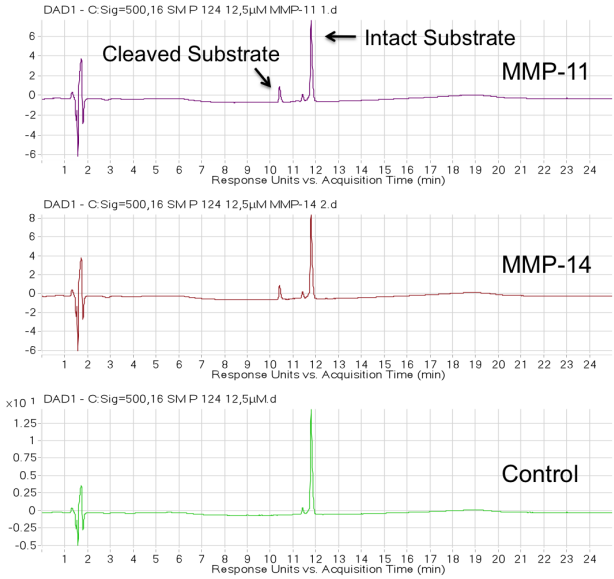

Figure 3.3.14: Chromatograms of FRET substrate SM P 124 incubated with MMP-11 (top), MMP-14 (middle), and without enzyme (bottom); evolving peak at 10.4 min represents fluorescein-labeled cleavage product

Table 3.3.1 summarizes substrate conversion with MMP-11 and MMP-14 detected via fluorescence FRET assay and by LC/MS-TOF assay. Rows highlighted in blue represent FRET substrates that were cleaved by MMP-11 and that were successfully validated by both assays (SM P 124, SM P 125, SM P 130, SM P 148). The same is true for SM P 124 analog AMCA labeled substrate SM P 155 highlighted in yellow, suggesting that attachment of fluorophores is not the reason for inactivity of most substrates, but that it is rather sequence related.

Entry	Substrate	FRET		LC/MS-TOF		Sequence
		MMP-11	MMP-14	MMP-11	MMP-14	
1	SM P 124	X	X	X	X	AANC(MeOBn)RM
2	SM P 127	-	-	-	-	YAEC(MeOBn)RM
3	SM P 130	X	X	X	X	AANLRM
4	SM P 133	-	-	-	-	YAELRM
5	SM P 148	X	X	X	X	AANC(MeOBn)VR
6	SM P 151	-	X	-	-	YAEC(MeOBn)VR
7	SM P 154	-	-	-	-	AANLVR
8	SM P 157	X	-	-	-	YAELVR
9	SM P 166	-	X	-	X	PLAC(MeOBn)WAR
10	SM P 169	-	-	-	-	AANC(MeOBn)WAR
11	SM P 172	X	X	-	-	YAEC(MeOBn)WAR
12	SM P 175	-	X	-	X	PLALWAR
13	SM P 178	-	-	-	-	AANLWAR
14	SM P 181	-	-	-	-	YAELWAR
15	SM P 123	-	-	-	-	YAEN
16	SM P 125	X	X	X	X	NAAC(MeOBn)RM
17	SM P 155	X	X	X	X	AANC(MeOBn)RM
18	OmniMMP^{TM}	-	X	-	X	PLAGLDap(Dnp)AR

Table 3.3.1: Assay validation via fluorescence and LC/MS-TOF, "X" marks substrate conversion, whereas "-" marks substrates that were not cleaved; gray rows display sequences adapted from the literature whereas blue rows display FRET substrates that are successfully cleaved by MMP-11 validated by both assays, the yellow row shows the successfully tested AMCA-substrate

A substrate preference for MMP-11 of the AAN motif in P3-P1 positions is indicated, since MMP-11 active substrates SM P 124, SM P 130, and SM P 148 bear this motif. Exchanging the AAN motif by YAE or PLA resulted in inactivity of the substrates. Exchange of alanine from P3 to P1 and asparagine from P1 to P3 is valid since SM P 125 is still active. Positions P2' and P3' can consist of a RM or VR motif. However, placing a WAR motif in P2'-P4' position results in complete activity loss as observed with SM P 169 and SM P 175. Entries 8 and 11 (SM P 157 and SM P 172) were revealed to show only insignificant increase of fluorescence with the FRET assay, since conversion of these substrates could not be confirmed with LC/MS-TOF.

3.3.1.3 Substrate Activity Comparison MMP-11/MMP-14

Substrate activities for MMP-11 and MMP-14 were determined for SM P 124, SM P 125, SM P 130, and SM P 148. The substrate sequence is the main factor for activity, although activity can also be enhanced with less space-demanding FRET pairs, since use of the smaller AMCA-Dnp FRET pair doubles activity of the substrate (Activity SM P 124 : SM P 155 is 1 : 2).
The highest substrate activity was determined for the AMCA labeled substrate SM P 155 with a k_{cat}/K_M value of 2685 $M^{-1}s^{-1}$. SM P 155 has a K_M of 4 μM and a k_{cat} of 0.011 s^{-1} while SM P 124 (k_{cat}/K_M= 1380 $M^{-1}s^{-1}$) displays a K_M of about 6 μM with a k_{cat} of 0.008 s^{-1}. Since a higher turnover number results in a higher K_M with unimolecular processes, it can be shown that the AMCA-Dnp FRET pair also strongly increases primary binding affinity k_1 with MMP-11, resulting in a slightly smaller K_M of SM P 155. Exchange of MeOBn protected cysteine to a leucine

in position P1' (SM P 130) results in activity loss (k_{cat}/K_M= 560 $M^{-1}s^{-1}$) as well as the P3 to P1 exchange of alanine and asparagine (SM P 125, k_{cat}/K_M= 630 $M^{-1}s^{-1}$). Both substrates display only half the k_{cat}/K_M value of SM P 124. SM P 148 ($k_{cat}/K_M\sim$ 1050 $M^{-1}s^{-1}$) displays large error bars due to its high background fluorescence in the FRET assay. This fact renders evaluation of substrate SM P 148 very challenging. The output varies a great deal, resulting in a huge standard error of 72 % of the calculated activity. SM P 148 is therefore not further considered as a reasonable FRET substrate, whereas SM P 124 represents the best fluorescein labeled FRET substrate (Table 3.3.2). Data plotted in the following graphs was collected in three independent measurements with three replicates each.

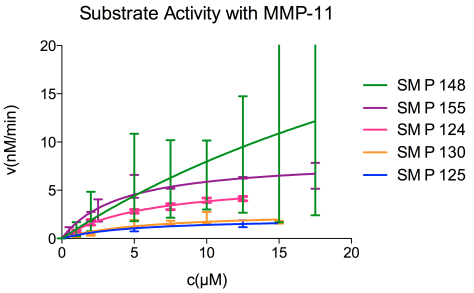

Figure 3.3.15: Substrate activities with MMP-11 of fluorescein labeled FRET substrates SM P 124, SM P 125, SM P 130, SM P 148, and AMCA labeled substrate SM P 155

Substrate activities assayed with MMP-14 show that AMCA substrate SM P 155 (k_{cat}/K_M= 47,820 $M^{-1}s^{-1}$) is 3 times more active than SM P 124 (k_{cat}/K_M= 16,530 $M^{-1}s^{-1}$). Because k_{cat}

Entry	FRET Substrate	Substrate Activity with MMP-11 k_{cat}/K_M $[M^{-1}s^{-1}]$	K_M [μM]	k_{cat} $[s^{-1}]$
1	SM P 124	1380	5.95 ± 1.44	0.0082 ± 0.0009
2	SM P 125	630	5.06 ± 3.15	0.0028 ± 0.0007
3	SM P 130	560	5.83 ± 3.92	0.0037 ± 0.0010
4	SM P 148	1050	41.05 ± 181.1	0.0543 ± 0.1812
5	SM P 155	2685	4.12 ± 1.45	0.0111 ± 0.0014

Table 3.3.2: Substrate Activity with MMP-11

is 10-fold higher for SM P 155 than for SM P 124, K_M increases in this case to 45 μM instead of 12 μM for SM P 124. However, when comparing activities for these two substrates, SM P 124 is 12 times more active for MMP-14 than for MMP-11, whereas SM P 155 is 18 times more active for MMP-14, leading to the conclusion that the fluorescein-dabcyl FRET pair reduces activity but increases selectivity towards MMP-11. SM P 130 (k_{cat}/K_M= 1380 $M^{-1}s^{-1}$) is only twice as active for MMP-14 compared to MMP-11, whereas SM P 125 (k_{cat}/K_M= 6760 $M^{-1}s^{-1}$) shows the same activity ratio than SM P 124. SM P 130 is a combination of the two most active and selective substrate sequences published by Pan *et al.*, originating from a phage display screening, identifying naturally selective sequences for MMP-11. This explains the rise in activity ratio for MMP-11 over MMP-14 for SM P 130, although it is accompanied with a significant loss of overall substrate activity. Incorporation of the MeOBn protected cysteine renders the substrate more active, but also reduces MMP-11/MMP-14 activity ratio (Table 3.3.3).

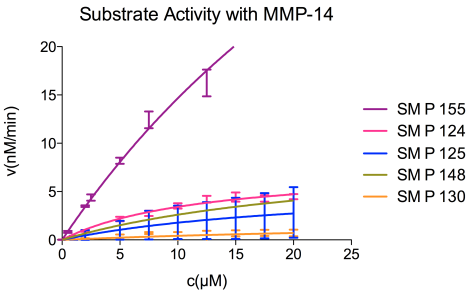

Figure 3.3.16: Substrate activities with MMP-14 of fluorescein labeled FRET substrates SM P 124, SM P 125, SM P 130, SM P 148, and AMCA labeled substrate SM P 155

Comparison of active FRET substrates tested, highlights SM P 124 as the most active fluorescein-dabcyl labeled substrate. Despite of a 12-fold enhanced activity for MMP-14 in comparison to MMP-11 for SM P 124, combination of literature sequences and modification with a fluorescein - dabcyl FRET pair yielded successfully evaluated FRET substrates for human MMP-11 with 4-fold increased activity compared to substrates published by Pan *et al.* for human MMP-11.[64] Additionally, an overall reduction of activity ratio for MMP-14 over MMP-11 from 90-fold down to 12-fold was achieved, when compared to the very active but unselective sequence tested with mouse MMP-11 by Mucha *et al.*[99] In addition, activity comparison with a more active batch of MMP-11 also revealed a further activity ratio decrease for MMP-14 over MMP-11 to a factor of 2 (see final activity value in table 3.3.6 on page 118).

Entry	FRET Substrate	Substrate Activity with MMP-14 k_{cat}/K_M [$M^{-1}s^{-1}$]	K_M [μM]	k_{cat} [s^{-1}]	Activity Ratio MMP-11/MMP-14
1	SM P 124	16530	12.28 ± 3.15	0.2030 ± 0.0255	1/12
2	SM P 125	6760	23.44 ± 72.79	0.1585 ± 0.3082	1/11
3	SM P 130	1380	44.41 ± 182.40	0.0612 ± 0.1885	1/2
4	SM P 148	9644	25.75 ± 44.92	0.2483 ± 0.2872	1/9
5	SM P 155	47820	44.82 ± 19.4	2.1433 ± 0.6918	1/18

Table 3.3.3: Substrate activity with MMP-14

Concluding from the performed measurements, FRET substrates for MMP-11 are best constructed employing arginine and methionine in P2' and P3', respectively as in SM P 124 rather than valine and arginine as in SM P 148, since it reduces FRET efficacy and therefore results in high background fluorescence. Furthermore, a AAN motif is essential in positions P3-P1 as substrates harboring a YAE or PLA motif were inactive with MMP-11. Alanine proved to be essential in P3 as substrates containing proline or tyrosine in P3 were found to be inactive. However, the shorter amide residue of asparagine was tolerated, but yielded a 2-fold decrease in activity with MMP-11.
The unnatural amino acid C(MeOBn) ligating to the S1' pocket was found to increase activity with MMP-11 (SM P 124), but also increased activity for MMP-14. Since MMP-11 is the only metalloprotease occupying a glutamine in position 215 of the S1' pocket, it was believed that an interaction with this specific amino acid would strongly increase selectivity for MMP-11. This hypothesis was proven wrong, as in fact, leucine proved to increase the activity ratio of MMP-11 over MMP-14 (SM P 130).
Addition of the large fluorescein-dabcyl FRET pair to the sequence may however disturb affinity for the protein, due to interference of the rather long dabcyl residue coupled to a lysine. Shortening of the quencher moiety by coupling it to a diaminopropionic acid instead of coupling to a lysine may increase affinity of the fluorescein-dabcyl labeled substrates as has been observed for SM P 155 bearing a shorter dinitrophenyl dark quencher. Table 3.3.4 on page 113 summarizes pocket binding trends of successfully tested sequences for MMP-11 listed in an order of decreasing activity starting with the most active substrate SM

P 155 as entry 1. Polar residues are marked blue, while unpolar amino acids are listed in red.

Entry	Name	P3	P2	P1	P1'	P2'	P3'	FRET pair
1	SM P 155	A	A	N	C(MeOBn)	R	M	AMCA-Dnp
2	SM P 124	A	A	N	C(MeOBn)	R	M	Fluo-Dabcyl
3	SM P 125	N	A	A	C(MeOBn)	R	M	Fluo-Dabcyl
4	SM P 130	A	A	N	L	R	M	Fluo-Dabcyl
5	SM P 148	A	A	N	C(MeOBn)	V	R	Fluo-Dabcyl
6	MMP-11	H183-F185	Q227	H183	Q215	I180 - F240	unknown	Subsite Interaction
7		unpolar	polar	polar	polar	unpolar	solvent exposed	Character

Table 3.3.4: Sequence argumentation with crystal sructure information obtained from [64, 65, 57, 56, 53, 52, 48]

3.3.2 Activity Comparison Throughout the MMP Family

3.3.2.1 Kinetic FRET Assay

Due to overlapping substrate preferences and highly conserved catalytic domains throughout the MMP family the term "activity comparison" was preferred over "selectivity discussion", as the term "selectivity" is generally not applicable for MMPs.
For the activity determination of FRET substrate SM P 124 with additional members of the MMP family, two MMP kits were purchased from Enzo Life Sciences containing MMP-1, -2, -3, -7, -8, -9, -10, -11, -12, and MMP-13. All enzymes were titrated with 12.5 μM SM P 124 at differing enzyme concentrations.
Figure 3.3.5 depicts the graphical linear regression, whereas activities are listed below in U/μg, 1 U (Unit) being 100 pmol/min. Buffer conditions for MMP-3 were altered to pH= 6, since this protease is most active at the given pH. FRET assay concentrations of differing MMPs were used in relation to their activity. For MMP-11 a higher concentration was chosen to simplify fluorescence readout, due to sensitivity of MMP-11 stability.

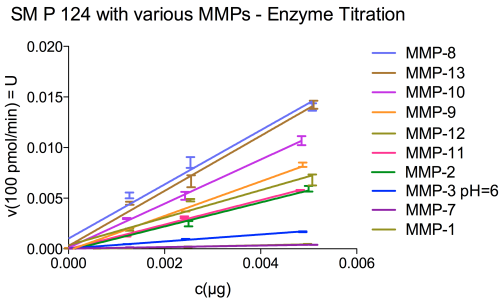

Figure 3.3.17: Enzyme titration of different MMPs with FRET substrate SM P 124

Entry	Protease	Activity [U/μg]	c [nM]
1	MMP-1	0.096 ± 0.099	12.0
2	MMP-2	1.186 ± 0.113	1.6
3	MMP-3	0.345 ± 0.017	4.2
4	MMP-7	0.076 ± 0.007	6.0
5	MMP-8	2.675 ± 0.306	0.3
6	MMP-9	1.702 ± 0.110	0.5
7	MMP-10	2.178 ± 0.060	4.6
8	MMP-11 (batch 3-TT7141)	1.209 ± 0.058	12.5
9	MMP-12	1.359 ± 0.220	1.0
10	MMP-13	2.718 ± 0.182	0.4

Table 3.3.5: Enzyme activity determination of varying MMPs with FRET substrate SM P 124

Substrate velocities of SM P 124 with eleven different MMPs were plotted against the concentration of SM P 124 applied. The graphs were fitted with non-linear Michaelis-Menten approximation (Figure 3.3.18). Data shown was combined from three or

more independent measurements with three replicates each. Table 3.3.6 displays activities of SM P 124 with different MMPs as well as selectivity for MMP-11. Final activity values for SM P 124 are shown in yellow.

SM P 124 was identified as a highly active substrate for MMP-11 when competing against MMP-1 and MMP-7 (Figure 3.3.18b, graphical representation of table 3.3.6). This result is in agreement with structural data of the S1' pocket of MMP-1 and MMP-7 that occupy arginine and tyrosine, respectively, in a position where leucine is observed in all other MMPs and where MMP-11 holds a glutamine.[55] Therefore, the specificity pocket S1' of MMP-1 and MMP-7 forms a more shallow pocket that interferes with long, unnatural residues like MeOBn and results in inactivity of SM P 124.
SM P 124 proves to be only twice as active for MMP-14 than for MMP-11, resulting from measurements with a more active batch of MMP-11 (3-T7141).
Furthermore, SM P 124 is equally well cleaved for MMP-3 at pH= 6 and MMP-10, which may be due to familial similaritiy, since MMP-3 and MMP-10 are also part of the stromelysin family (stromelysin-1 and stromelysin-2).
MMP-2, -8, -9, -12, and -13 cleave SM P 124 about 10 times faster. Unfortunately, no comparable data is available for MMP-11 substrates published previously, as they have only been tested in comparison to MMP-14.

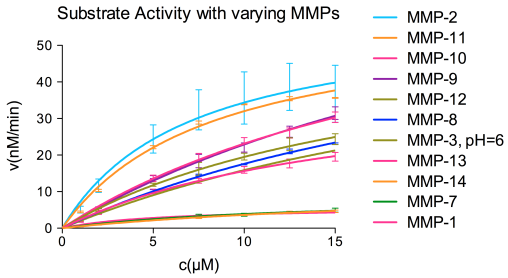

(a) Michaelis-Menten kinetics of SM P 124 with varying MMPs

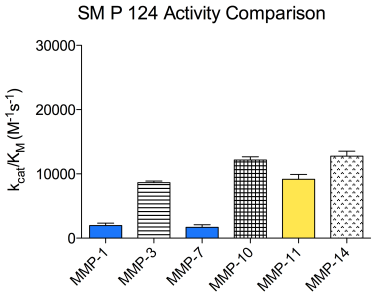

(b) Activity comparison of SM P 124 with a variation of MMPs

Figure 3.3.18: SM P 124 substrate selectivity assayed with a variation of available MMPs

Activity measurements with a quite active MMP-11 batch (batch 3-T7141) revealed increased overall activity values for SM P 124. The value was reproduced about 6 times and will be considered as the final activity value (k_{cat}/K_M= 9160 $M^{-1}s^{-1}$). Therefore, activity was increased by a factor of 4 when compared to Pan *et al.*'s substrates. Activity for MMP-11 over MMP-14 was in-

Entry	Protease	SM P 124 Activity k_{cat}/K_M [$M^{-1}s^{-1}$]	K_M [μM]	k_{cat} [s^{-1}]	Selectivity for MMP-11
1	MMP-1	1590	5.46 ± 0.86	0.0082 ± 0.0005	6
2	MMP-2	86970	6.99 ± 3.27	0.6081 ± 0.1228	$\frac{1}{10}$
3	MMP-3	8500	31.42 ± 13.04	0.2610 ± 0.080	1
4	MMP-7	1950	13.66 ± 5.08	0.0254 ± 0.0054	5
5	MMP-8	130020	29.18 ± 3.82	3.8317 ± 0.3625	$\frac{1}{14}$
6	MMP-9	111020	32.31 ± 10.67	3.231 ± 0.7917	$\frac{1}{12}$
7	MMP-10	12400	24.20 ± 5.71	0.2866 ± 0.0464	1
8	MMP-11	9160	8.23 ± 1.08	0.0778 ± 0.0047	-
9	MMP-12	49120	19.00 ± 5.24	0.9423 ± 0.1661	$\frac{1}{5}$
10	MMP-13	108820	16.42 ± 3.72	1.7213 ± 0.2370	$\frac{1}{12}$
11	MMP-14	14180	21.87 ± 6.55	0.3101 ± 0.0620	$\frac{1}{2}$

Table 3.3.6: SM P 124 activities for MMP-11 in comparison to other MMPs; Substrate activity with MMP-11 is depicted in yellow, green rows mark MMPs with factor for which SM P 124 is selective for MMP-11, whereas blue rows show MMPs with equally well cleavage

creased 45 fold in comparison to substrates synthesized by Mucha *et al.*

3.3.2.2 LC/MS-TOF Validation

Cleavage of SM P 124 was confirmed by LC/MS-TOF measurements. Injection of 12.5 μM substrate SM P 124 assayed with a variation of MMPs yielded a cleavage product peak at 10.4 min retention time and was observed with almost all MMP family members. However, no conversion was confirmed via LC/MS-TOF for MMP-1, even though the FRET assay displayed some activity. Additionally, only very little cleavage product was observed with MMP-7. These results confirm the activity determination measured via FRET assay (Figure 3.3.19 and 3.3.20).

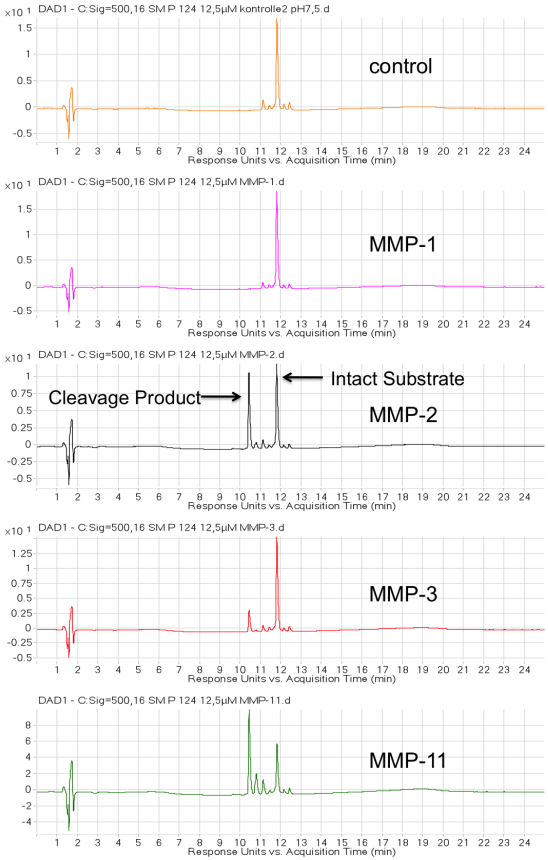

Figure 3.3.19: LC/MS-TOF validation of SM P 124 FRET assay with varying MMPs, negative control (top) followed by MMP-1, -2, -3, and -11; substrate cleavage peak evolves at 10.4 min

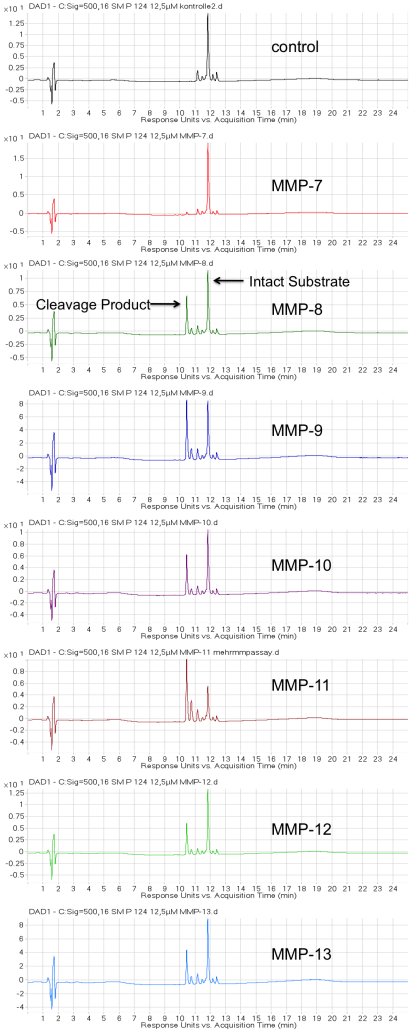

Figure 3.3.20: LC/MS-TOF validation of SM P 124 FRET assay with varying MMPs, negative control (top) followed by MMP-7, -8, -9, -10, -11, -12 and -13; substrate cleavage peak evolves at 10.4 min

As has been previously stated in section 1.1.5.2 on page 39, other metalloproteases significantly up-regulated in PDAC are MMP-3, MMP-7, and MMP-9.[67] FRET substrate SM P 124 is hardly active with MMP-7 and shows reduced activity for MMP-3. A drawback could be the 12-fold increased activity for MMP-9. This protease and also MMP-14 (which was used as an activity comparison standard) were shown to be expressed by Langerhans cells following cell activation.[113] However, MMP-9 is expressed as an inactive pro-form whereas MMP-14 is coexpressed and regulated by tissue inhibitor of matrix metalloproteases 2 (TIMP-2).[113, 114] MMP-9 is activated by tumor necrosis factor alpha (TNF-α), a cytokine involved in systemic inflammation and cancer.[115] MMP-14 is most often overexpressed and therefore activated in malignant tumor tissues, including lung and stomach carcinomas.[116] Overexpression of MMP-9 and MMP-14 is therefore not considered critical, but cancer-related activation would actually help produce a strong fluorescence signal for *in vivo* detection.

However, selectivity is a major problem observed when adressing matrix metalloproteases. Increasing substrate activity especially for the hardly active MMP-11 over MMP-14 poses a true challenge, due to the wide substrate specificity of MMP-14, as it has been found to degrade, for example, collagen type 1, collagen type 2, collagen type 3, aggrecan, elastin, fibronectin, gelatin, tenascin, perlecan, laminin, α_1-proteinase inhibitor, and α_2-macroglobulin.[117, 118, 119].
Due to the highly conserved catalytic domain throughout the family, with only small mutations within the selectivity pocket and equal physiological substrate preferences, selectivity remains an issue to be addressed.

Since substrate conversion of MMP-11 is relatively slow in comparison to more active MMPs, FRET assay measurements provide a fast and sensitive way of substrate cleavage detection. However, LC/MS-TOF is independent of background fluorescence and is able to identify cleavage products by mass. Employing these two methods in a tandem assay provides a precise analysis of reactions taking place between enzyme and substrate.

3.3.3 Cellular Kinetic FRET Assay

Furthermore, cellular evaluation of the most active and selective FRET substrate SM P 124 was performed to investigate the potential of MMP-11 imaging probes for the early detection of pancreatic cancer. Therefore, MMP-11 overexpressing cancer cell lines and a negative control cancer cell line were tested with SM P 124. Cell lines known for MMP-11 overexpressions are pancreatic adenocarcinoma cell line MIA PaCa-2 and breast adenocarcinoma MCF-7.[120, 121] Jurkat was chosen as a putative negative control cell line, since MMPs are extracellular matrix proteins, that are presumably not expressed by cells in suspension.

To prove this hypothesis, a Western Blot was performed and the protein content was quantified. Cells were harvested and lysed, the supernatant was denatured, and the proteins were separated via electrophoresis. The proteins were then transferred to a PVSF membrane and stained with anti-MMP-11 as a primary antibody. Applying a horseradish peroxidase (HRP) labeled secondary antibody allowed observation of the signals via luminescence. MMP-11 expression was confirmed in MIA PaCa-2 and MCF-7, while MMP-11 expression in Jurkat cells was proven negative (Figure 3.3.21a). Employment of a β-actin antibody as a standard for the detection of housekeeping protein β-actin allowed quantification of the observed MMP-11 bands. Quantification was evaluated with a Welch's t-test[1] and was validated as being significant (P= 0.0114) for expression level comparison

[1] a null hypothesis of unpaired samples is tested for their probability, determined by the obtained results

$t = \frac{\overline{X}_1 - \overline{X}_2}{\sqrt{\frac{s_1^2}{N_1} + \frac{s_2^2}{N_2}}}$ ($\overline{X}$= sample, mean; s = sample variance; N = sample size)

of MIA PaCa-2 to Jurkat, whereas the expression difference of MCF-7 and Jurkat was tested extremely significant with an individual P value of P= 0.0002. The overall P value for the applied t-test is P= 0.0001.

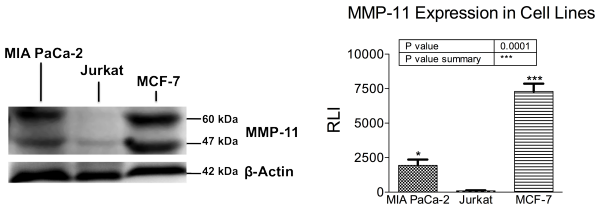

(a) Western blot of cell lysates (b) MMP-11 expression quantification

Figure 3.3.21: Western blot of cell lysates

Additionally, SM P 124 substrate activity was monitored in a FRET assay with the evaluated cell lines. Adherent cells were seeded onto a microplate two days prior to measurement. Suspension cells were added to the plate shortly before measurement. Substrates SM P 124 and negative control substrate SM P 123 were added and the change in fluorescence was recorded over time. MIA PaCa-2 and MCF-7 show strong substrate cleavage, while no substrate conversion was observed with Jurkat cells. Negative control substrate SM P 123 displays no cleavage with MIA PaCa-2 and Jurkat cells, whereas only little signal was observed for MCF-7. The corresponding spectra are displayed below (Figure 3.3.22) .

The performed FRET assays confirm activity measurements carried out with the catalytic domain of MMP-11 and are in agree-

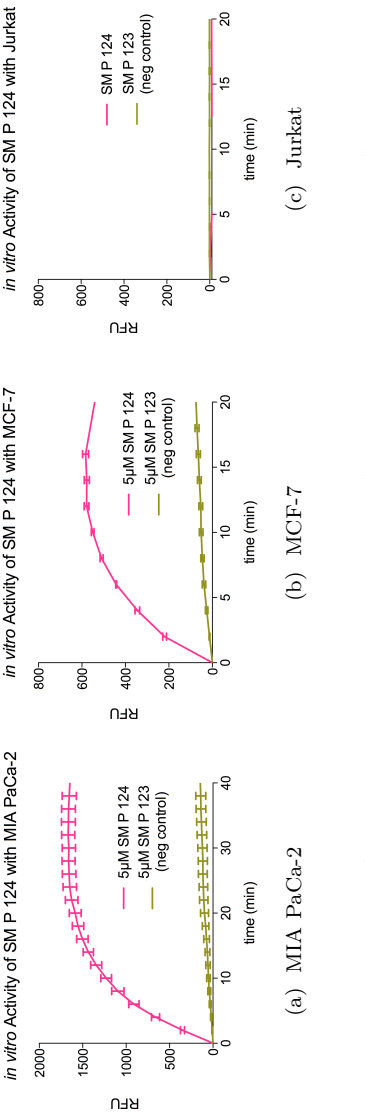

(a) MIA PaCa-2 (b) MCF-7 (c) Jurkat

Figure 3.3.22: Cell lines assayed with substrate SM P 124 and neg. control SM P 123

ment with MMP-11 expression determined via Western Blot. Protein expression of MCF-7 is different from MIA PaCa-2 expression which may be a reason for the observed SM P 123 cleavage, since peptides are always susceptible for protease cleavage.

3.3.4 Confocal Laser Scanning Microscopy of FRET Substrates

Substrate cleavage was furthermore monitored via confocal laser scanning microscopy (CLSM) by seeding the cells on glass slides. Slides were adapted to a carrier, and FRET substrates SM P 124 and negative control SM P 123 were administered to the cells. Results obtained from CLSM confirm previous kinetic measurements. Interestingly, MIA PaCa-2 cells show internalization of the cleaved substrate, apart from a strong fluorescent signal. Images taken show compartmentalized intracellular cleavage, indicating substrate cleavage at MMP-11 transporting vesicles. The surrounding solution also depicts high amount of substrate cleavage, suggesting accumulation of secreted MMP-11 in solution. Furthermore, membrane staining is observed probably showing release of MMP-11 from vesicles (Figure 3.3.23a). SM P 123 displays some unspecific cleavage in solution. However, the substrate was neither internalized by MIA PaCa-2 nor located at the membrane and is therefore confirmed as a valid negative control substrate (Figure 3.3.23b).

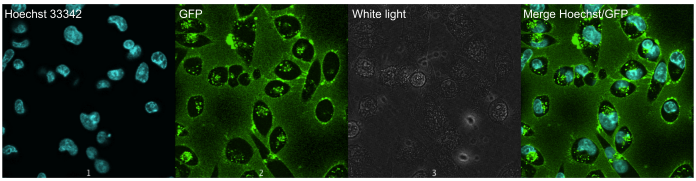

(a) SM P 124 30 min after addition to MIA PaCa-2

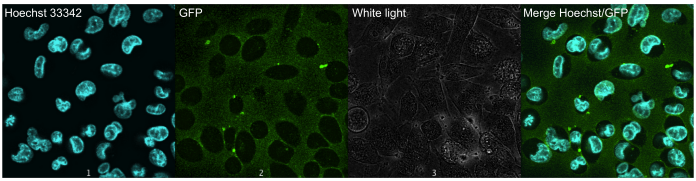

(b) SM P 123 (neg control) 30 min after addition to MIA PaCa-2

Figure 3.3.23: MIA PaCa-2 cells with MMP-11 activatable FRET substrate SM P 124 and negative control SM P 123

MCF-7 cells were also tested for substrate cleavage, and a strong fluorescence signal was emitted after addition of MMP-11 tracer SM P 124. Cells show membrane staining and internalization of cleaved substrate, although not as distinctly as with MIA PaCa-2 cells. Negative control substrate SM P 123 produces some background signal in solution and little membrane staining, but internalization was not observed. However, MMP-11 tracer and its negative control are clearly distinguishable (Figure 3.3.24). Furthermore, as anticipated, cleavage of SM P 124 and SM P 123 was not detected with negative control cell line Jurkat (Figure 3.3.25).

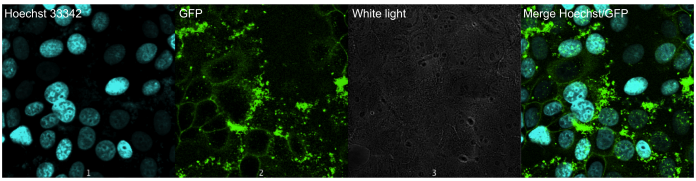

(a) SM P 124 30 min after addition to MCF-7

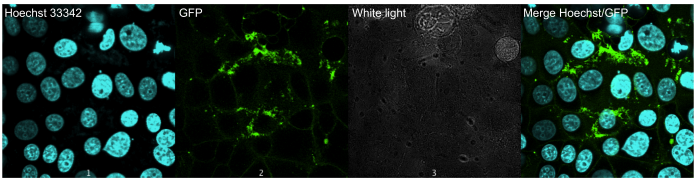

(b) SM P 123 (neg control) 30 min after addition to MCF-7

Figure 3.3.24: MCF-7 cells with MMP-11 activatable FRET substrate SM P 124 and negative control SM P 123

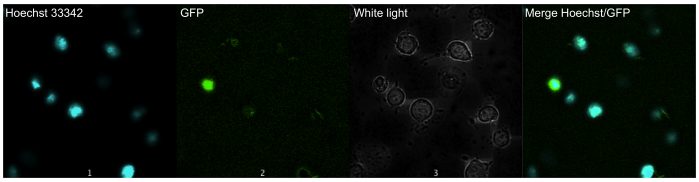

(a) SM P 124 30 min after addition to Jurkat

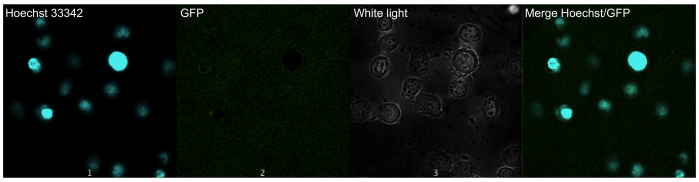

(b) SM P 123 (neg control) 30 min after addition to Jurkat

Figure 3.3.25: Jurkat cells with MMP-11 activatable FRET substrate SM P 124 and negative control SM P 123

SM P 124 has been successfully validated as a MMP-11 tracer with the recombinant catalytic domain of MMP-11. The substrate delivered convincing quantitative fluorescent signal increase in cellular assays and was not cleaved by the negative control cell line Jurkat. Furthermore, CLSM images confirmed kinetic assay measurements and cellular MMP-11 detection was made visible for the first time by the use of the prepared FRET substrate SM P 124. The recorded images consolidate SM P 124 as an imaging tool for MMP-11 detection *in vitro* and for cellular events. Moreover, SM P 123 proved to be a valuable negative control, since it was cleaved neither by the catalytic domain of MMP-11, nor during cellular quantitative fluorescence measurements, and it displayed only low fluorescence background during CLSM. These facts confirm the success of the challenging task of moni-

toring MMP-11 activity *in vitro* and point out the high potential for substrates as *in vivo* imaging tools.

Unfortunately, peptides were degraded *in vivo* within 30 minutes (data not shown), rendering them useless for *in vivo* imaging. In order to detect MMP-11 activity *in vivo* the tracer has to accumulate at the site of expression, preferably over a time range of 24 hours. Therefore, polymers have been used previously as drug delivering supports to prevent early degradation.[122]

3.4 Polymer-Supported FRET Imaging Substrates

Bremer et al. developed polymer-conjugated peptidic substrates for MMP-2 cleavage applicable for *in vivo* imaging in 2001.[123] In this first approach single near infrared fluorophore (NIRF)-labeled substrate sequences were coupled to a graft copolymer (methoxy-polyethylene-glycol-(MPEG)-derivatized poly-L-lysine). In this construct quenching was achieved by self-quenching of NIRF labels, due to the very small Stokes shift of NIR cyanine dyes, resulting in a large overlap of excitation and emission spectra, cyanine dyes represent efficient self-quenchers. The copolymer-supported probe was successfully imaged in HT1080 xenografts 2 h after tail vein injection, proving that matrix metalloprotease activity is accessible for *in vivo* imaging (Figure 3.4.1).

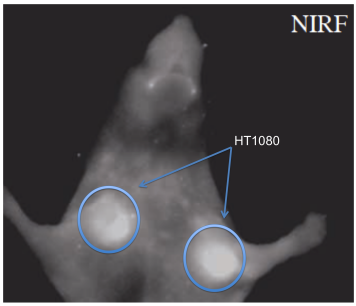

Figure 3.4.1: MMP-2 activatable tracer by Bremer *et al.* imaged in HT1080 xenograft [123]

Unfortunately, synthesis of these probes was tedious, since poly-L-lysine needs to be conjugated to MPEG chains in order to

decrease its toxicity *in vivo*.[124] Synthesis of the MPEG conjugated poly-L-lysine graft polymer affords first functionalization of succinimidyl anhydride with MPEG and its conjugation to the poly-L-lysine backbone.[125] Furthermore, peptides were introduced via a thiol-specific reaction by substitution of iodine, requiring protecting groups for additional thiols present in the sequence.[126] In summary, to prepare this MMP-2 cleavable substrate sequence conjugated to the MPEG-poly-L-lysine graft polymer afforded at least 6 coupling steps and various steps of isolation, rendering this synthesis strategy not only time consuming but also work intensive.

Jindrich Kopeček and his colleagues first developed N-(2-hydroxypropyl)methacrylamide (HPMA) copolymers (pHPMA[2]) in the 1970s.[127] The copolymer is water-soluble and was developed as a carrier for therapeutical delivery.[128, 129] pHPMA-conjugates posess several advantages over non-polymer supported therapeutics, including increased aqueous solubility, bioavailability, prolonged drug retention time, reduced systemic toxicity, decreased multiple drug resistance, and enhanced therapeutic efficacy.[127, 130, 131] Copolymer-drug conjugates like pHPMA–doxorubicin conjugate and pHPMA–platinate conjugate have even entered various phases of clinical trials.[132, 133, 134] pHPMA therefore offers a clear advantage over the graft polymer that Bremer's group employed for *in vivo* imaging, since generation of pHPMA is achieved in a single step free radical polymerization (FRP) and can afterwards be readily used for substrate conjugation and fluorophore introduction, resulting in a 2-3 step straightforward synthesis.

[2]the copolymer made of HPMA is termed polyHPMA, therefore it is abbreviated by pHPMA

3.4.1 Synthesis of Polymer-Supported FRET Substrates

pHPMA was therefore chosen as an *in vivo* imaging matrix in order to develop novel, highly quenched polymer-supported FRET substrates that produce a fluorescent signal only after cleavage of the conjugated FRET sequence. The advantage over self-quenched conjugates is the dark quenching effect of the dabcyl moiety of FRET substrate SM P 124, which should increase the signal-to-noise ratio during *in vivo* measurements.
Unfortunately, up to now, a general tool to access versatile peptide-polymer conjugates is missing, since conventional amide coupling requires fully protected peptide sequences. To address this challenge, a HPMA copolymer bearing thioester functionalities **15**, which enable native chemical ligation (NCL), was developed and synthesized by M.Sc. Katharina Koschek of Prof. Jörg Rademann's group at the Leibniz-Institut für Molekulare Pharmakologie (FMP) (Figure 3.4.2, unpublished work). NCL is a chemoselective method that enables peptide bond formation by reacting a thioester **15** with an N-terminal unprotected cysteine **16**. The peptide bond is formed through a S→N acyl shift, as shown in figure 3.4.2.[135]

3.4.1.1 Synthesis of Fluorescein-labeled Copolymer-Substrate Conjugates

As described above, pHPMA was synthesized with thioester functionalities, therefore, FRET substrate SM P 124 needed to be synthesized with an additional cysteine at the N-terminus. This tag allows chemoselective coupling to the polymeric support via

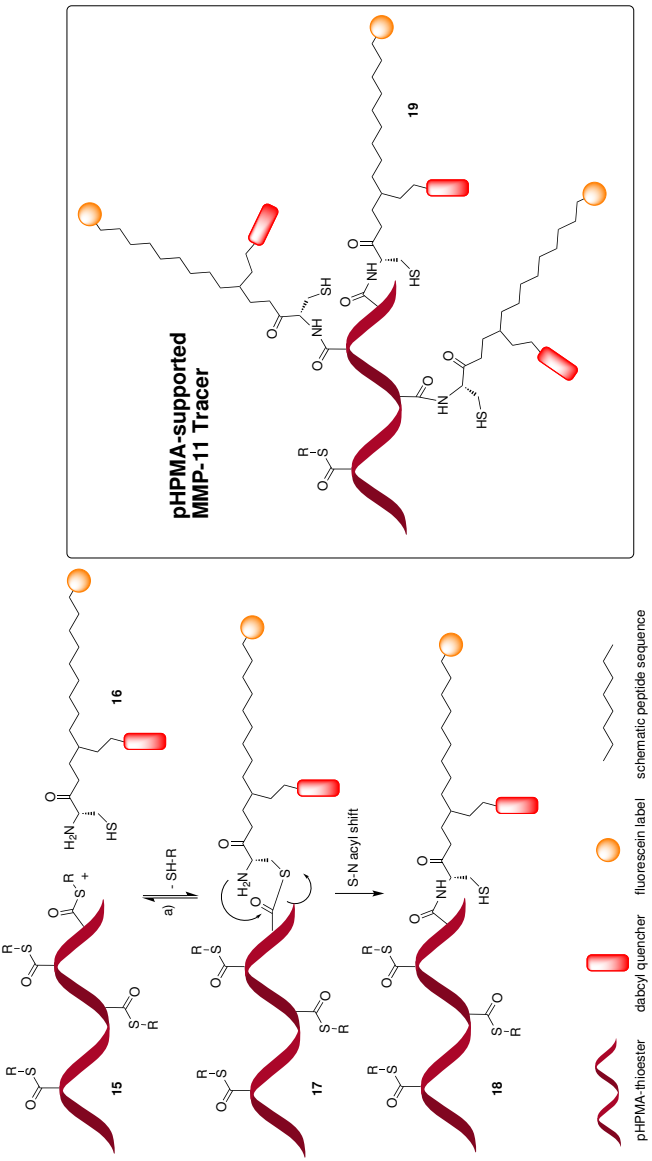

Figure 3.4.2: Native chemical ligation enables substrate coupling to polymeric support

NCL with the fully unprotected peptide sequence.
The synthesis of the peptide sequences was carried out as described previously (see 3.2.2.2 on page 70). Table 3.4.1 lists the prepared sequences and yields, relating to the uncoupled sequences with N-terminal cysteine. Again, the yields when applying the fluorescein labeled resin were low when compared to sequences that were prepared on a Rink amide resin. Entry 1 shows the MMP-11 cleavable substrate modified with an N-terminal cysteine SM P 122, and entry 2 shows its negative control sequence SM P 194.

Native chemical ligation reactions will be described briefly at this point but will not appear in the experimental part, since coupling of substrates to the polymer was carried out by Katharina Koschek, as this represents part of her PhD thesis.
The copolymer was dissolved in sodium phosphate buffer (100 mM, pH 7.4) - dioxane mixture to give a final concentration of 10 mg/ml. After addition of the appropriate amount of peptide the reaction was started by addition of thiophenol (1% v/v) and benzylmercaptan (1% v/v). The ligation reaction was allowed to proceed for 24 h at RT. The reaction mixture was purified by dialysis (cut-off 3500 Da) and gel filtration (Pd10; G25).
Substrate loading was confirmed via UV/Vis measurements as well as via amino acid analysis. Employing Lambert-Beer's law[3], the absorbance intensity determined of the pHPMA-substrate conjugate (Figure 3.4.3b) is divided by the slope of fluorescence standard absorption per μM, determined by figure 3.4.3a.
Unfortunately, coupling conditions to the copolymer need to be further investigated, since loading efficiency was determined to

[3] $A = \varepsilon cd$; A= absorption, ε= emission coefficient, c= molar concentration, d= pathlength of sample

Entry	Sequence	Name	Yield crude (%)	Yield (%)	Polymer Name
1	H-CGRRRK(Dabcyl)GGAAN-C(MeOBn)RMGG-Fluo	SM P 122	11	2	KK258
2	H-CGRRRK(Dabcyl)GYAENG-Fluo	SM P 194	27	9	KK257

Table 3.4.1: Sequences synthesized for polymeric support and yields

be only 5 % for MMP-11 cleavable substrate copolymer conjugate KK258, meaning that out of 20 possible functionalized thioesters at the polymer only 1 actually reacted with the offered substrate. The negative control substrate KK257 reacted somewhat better and yielded 18 % loading, meaning 4 substrates out of 20 possible. Results obtained by absorption measurements are in agreement with results from amino acid analysis (Data not shown).

Low loading efficiency was mainly due to solubility problems[4], as 10 mg/ml of copolymer afforded high amounts of substrate solved. Unfortunately, due to the small quantities obtained of the substrate synthesis, coupling could not be repeated and pHPMA-substrate conjugates had to be evaluated as obtained.

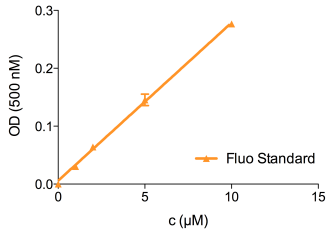

(a)

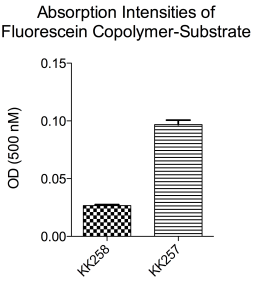

(b)

[4]the prepared peptides are usually water soluble, however they did not dissolve in this case. Addition of dioxane did also not increase solubility. Experiments will be repeated with a water/acetonitrile mixture.

Fluorescence Standard	OD/μM
SM P 124	0.02728

Conjugate	Loading (mmol/g)	Loading (%)	Peptides coupled out of 20 possible
KK258	0.01	5	1
KK257 (neg control)	0.04	18	4

Figure 3.4.3: Loading determination of fluorescein labeled copolymer-substrate conjugates KK258 and negative control KK257; a) Fluorescence standard determination; b) Absorption intensity of conjugates

3.4.1.2 FRET Efficiency

FRET efficiencies of the prepared copolymer-substrate conjugates were determined at an excitation wavelength of 483 ± 10 nm and an emission wavelength of 525 ± 10 nm. Both substrate conjugated copolymers KK258 and KK257 were quenched by a factor of 8 at a concentration of 1 μM in comparison to the cleaved substrate that was used as a fluorescence standard. However, the more substrate was present in solution, the more effective the quenching, as demonstrated with negative control substrate KK257 with a quenching factor of 95, when increasing the concentration 4-fold from 1 μM to 4 μM (Figure 3.4.4).

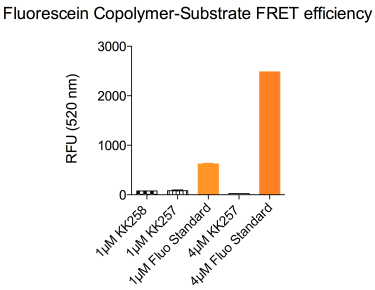

Figure 3.4.4: FRET efficiency of copolymer-conjugated substrates KK258 and neg control KK257

FRET efficiency was found to be increased with conjugated substrates, exhibiting a quenching factor of 95 in comparison to 35 for non-conjugated substrates with comparable substrate concentrations (4 μM and 5 μM). It is believed that quenching efficiency increases, due to the forced proximity of substrates conjugated to the copolymer backbone.

3.4.1.3 Synthesis of NIRF-labeled Copolymer-Substrate Conjugates

In order to pursue full body *in vivo* imaging of mice, penetration depth in tissue needs to be enhanced by utilizing near infrared fluorophores (NIRF). At their long excitation and emission wavelengths (600-900 nm), autofluorescence of tissue and scattering light, both main causes of signal depletion in tissue, are at a minimum.[77]
Since the NIR dye could not be introduced to the substrate sequences on solid phase, peptide sequences bearing lysine residues

were synthesized and isolated. The peptide sequences were loaded to the HPMA copolymer via NCL and were then labeled at the lysine residues with the NIR dye in solution.
A small variety of peptides was prepared. Peptide sequences were designed as singly labeled self-quenched substrates (one lysine residue) as well as doubly labeled FRET substrates (two lysine residues) (Figure 3.4.5). To investigate the importance of a three arginine motif for increased hydrophilicity and cellular internalization, sequences were prepared with and without this motif.

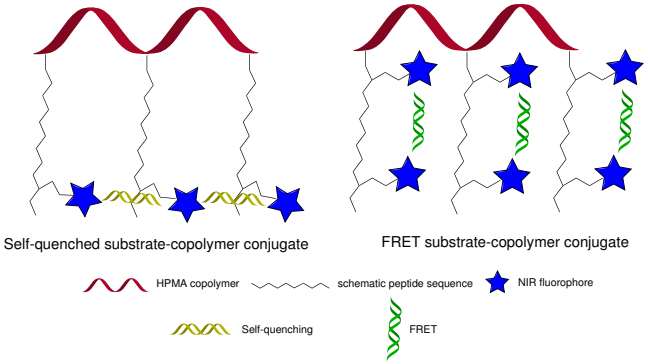

Figure 3.4.5: Singly labeled self-quenched conjugate vs doubly labeled NIR-FRET substrate conjugate

Substrates were prepared via standard Fmoc strategy solid phase synthesis, employing Rink amide resin for all sequences. The prepared peptide sequences were cleaved off the resin and isolated via HPLC. Yields of plain, unlabeled peptide sequences are represented in table 3.4.2. Entry 4 displays the cleaved NIRF-labeled substrate that is employed as a fluorescence standard. The cya-

nine dye NIR-797 was purchased from Sigma-Aldrich as an isothiocyanate and was used without further purification. Labeling of the cleaved peptide with the NIR dye was achieved in solution in DMF with 5 eq of NIR-797 and 5 eq of DIPEA, overnight at RT. The yield for SM P 190 corresponds to the overall yield after cyanine labeling of the cleaved substrate sequence, whereas all other yields represent yields of the peptide syntheses before loading to the copolymer. Entry 5 displays the non-targeted negative control copolymer KK216 loaded with 1,2-diaminoethane that was then used for NIRF-labeling.

The prepared substrate sequences SM P 110, SM P 137, and SM P 192 were coupled to the pHPMA thioester **15** via NCL to yield the unlabeled conjugate, as has been described earlier (Figure 3.4.6, example coupling is shown for peptide SM P 137 yielding KK244). The copolymer-substrate conjugate KK244 was then labeled in solution with 5 eq excess of cyanine isothiocyanate **20** (NIR-797, Sigma Aldrich) including 5eq of DIPEA in DMF, yielding final NIR-FRET MMP-11 tracer KK249. After consumption of all starting material the copolymer was precipitated and washed, filtrated over a gel column and dialysed to remove excess fluorophore.

Substrate loading was determined via amino acid analysis and yielded about 0.2 mmol/g, representing a mean coupling of 10 peptides of 29 possible coupling sites or a mean loading of 40 % peptide per copolymer.

Entry	Sequences	Name	Yield crude (%)	Yield (%)
1	H-CGGAANC(MeOBn)RMGGK(NH_2)-NH_2	SM P 110	97	88
2	H-CGGK(NH_2)GGAANC(MeOBn)RMGGK(NH_2)-NH_2	SM P 137	78	41
3	H-CGRRRK(NH_2)GGAANC(MeOBn)RMGGK(NH_2)-NH_2	SM P 192	54	23
4	Ac-C(MeOBn)RMGGK(Cy7)-NH_2 (Fluorescence Standard)	SM P 190	51	28
5	pHPMA-NH-CH_2-CH_2-NH_2 (neg control)	KK216	-	-

Table 3.4.2: Sequences and yields for NIRF-labeled substrates

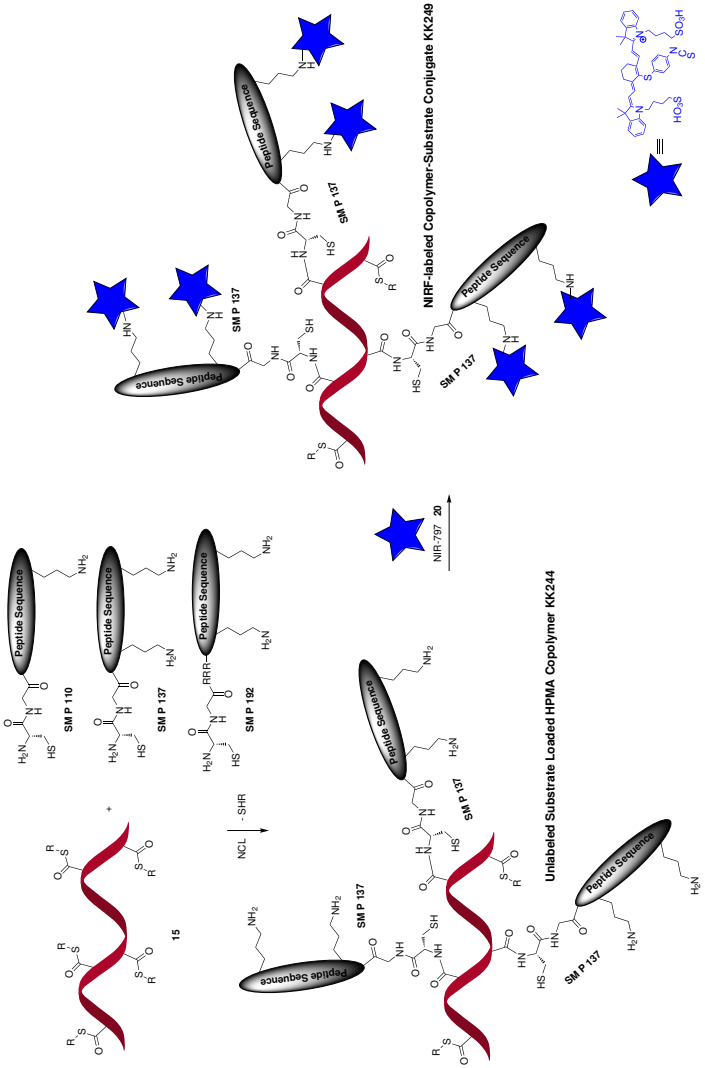

Figure 3.4.6: Synthesis scheme for copolymer-supported NIRF-labeled substrate

Entry	Peptide	Polymer Name	Peptide Loading (mmol/g)	Peptide Loading (%)	Peptides coupled out of 29 possible
1	SM P 110	KK229 II	0.198	34	10
2	SM P 137	KK244	0.150	31	9
3	SM P 192	KK252	0.210	38	11

Table 3.4.3: Yields for unlabeled peptide-loaded pHPMA

Labeling efficiency was determined via absorption measurements at 700 nm in comparison to the slope of cleaved substrate fluorescent standard SM P 190 at differing concentrations (Figure 3.4.7a and 3.4.7b). Labeling of FRET substrate-conjugates KK263 and KK249 yielded over 100 % labeling (275 % and 139 %, respectively), indicating either a side reaction with the hydroxy group of the pHPMA backbone or unbound fluorophore within the probe. Even after several dialyses and gel filtration steps, excessive fluorophore could not be removed from the probe, pointing towards the possible side reaction with the copolymer backbone. As a negative control, copolymer without substrate conjugation but labeled with NIR-797 was chosen in order to monitor copolymer contribution *in vivo* (KK241).

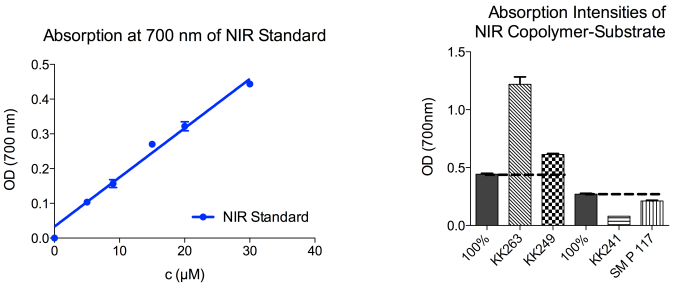

(a) (b)

Fluorescence Standard	OD/μM
SM P 190	0.01416

Unlabeled Conjugate	Labeled Conjugate	Labeling Degree (%)
KK252	KK263	275
KK244	KK249	139
KK229II	SM P 117	99
KK216	KK241 (neg control)	38

Figure 3.4.7: Labeling determination of NIRF-labeled copolymer-substrate conjugates a) Fluorescence standard determination; b) Absorption intensities, the dashed line represents 100 % coupling

3.4.1.4 Quenching Efficiency

Quenching efficiency was determined at an emission wavelength of 780 nm. The signal is quenched 12-fold for NIR-FRET copolymer-

substrate conjugates KK263 and KK249[5] and 7-fold for singly labeled self-quenched conjugate SM P 117 and non-targeted negative control copolymer KK241. As determined by absorption measurements, KK263 contains a significant amount of additionally bound fluorophore, that could not be separated by isolation. However, fluorophore emission is equally high as fluorescence emission of FRET-quenched KK249 and self-quenched SM P 117. It shows that quenching of cyanines works efficiently, but is not further decreased beyond a certain limit as it is demonstrated in figure 3.4.8. This also proves that two cyanines can function as a NIR-FRET pair, when attached to a peptide sequence. The advantage over singly labeled sequences is the stronger signal generation, due to two fluorescent parts instead of just one after substrate cleavage.

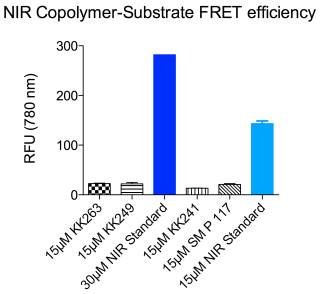

Figure 3.4.8: NIR-substrate conjugate FRET efficiency

NIR-FRET and self-quenched substrate-copolymer conjugates experienced a similar signal reduction of 12-fold for FRET conju-

[5] 15 μM substrate = 30 μM fluorophore, since 2 NIRF are coupled per peptide sequence; 30 μM NIRF standard value was corrected for its inner filter effect, since fluorescence emission is not linear at that concentration

gates and 7-fold for self-quenched substrate conjugates. Fluorescence output could not be diminished beyond a certain level, employing fluorophore-fluorophore FRET. A dark quencher, emitting excitation via molecular vibrations might further increase signal reduction of the quenched conjugates.

3.5 *In vitro* Validation of Polymer-Supported Imaging Substrates

3.5.1 Cellular FRET Assays

In vitro validation of the prepared copolymer-substrate conjugates had to be carried out directly at the cellular level, since conjugation to pHPMA affects substrate cleavage, strongly decelerating the cleavage process up to several hours. However, due to the relatively low activity of MMP-11 and its resulting inactivity upon storage at RT even after 2 h, measurement of copolymer conjugates with the recombinant catalytic domain of MMP-11 was not pursued. The prepared fluorescein-labeled substrate-copolymer conjugates and their NIRF-labeled analogs were therefore tested *in vitro* with MIA PaCa-2, MCF-7, and Jurkat cells, in order to prove substrate conversion of the copolymer-conjugates.
Cells were seeded to a cell-binding micro plate 2 days prior to measurement. Jurkat cells were seeded right before measurements. Copolymer-substrate conjugates were administered to the cells and were measured at 37 °C over 10 h.

3.5.1.1 Fluorescein-labeled Copolymer-Substrate Conjugates

Due to the low loading efficiency of fluorescein-labeled conjugates KK258 and negative control KK257, the increase of fluorescence effected by substrate cleavage, was small and decreased the signal-to-noise ratio, thereby resulting in deviations, which

are represented by large error bars. However, substrate cleavage of MMP-11 tracer KK258 was successfully observed with MMP-11 overexpressing MIA PaCa-2 and MCF-7 cells, whereas Jurkat cells exhibited an intensive signal increase for negative control conjugate KK257. KK257 was also cleaved to some extent by MIA PaCa-2 and MCF-7. It was observed, however, that KK257 is cleaved a lot slower than MMP-11 tracer KK258 (Figure 3.5.1).

3.5.1.2 NIRF-labeled Copolymer-Substrate Conjugates

NIRF-labeled MMP-11 Tracers KK249 and KK263 and negative control copolymer KK241 were also evaluated cellularly with the cell lines listed above. Cleavage was monitored over 10 h while fluorescent output was recorded every 30 min.
KK249 and KK263 were both cleaved at the same rate with all cell lines, indicating that the additional RRR motif at the N-terminal of KK263 is not necessary for cellular cleavage of the conjugates. MIA PaCa-2 cells even displayed a slightly better cleavage rate for KK249 (without RRR motif). Surprisingly, not only MIA PaCa-2 and MCF-7 cells showed MMP-11 tracer cleavage, but cleavage was also observed with MMP-11 negative Jurkat cell line. Negative control copolymer KK241 showed some signal increase with MCF-7 cells. It must be considered that cells internalize pHPMA over a range of several hours and then degrade it, thereby increasing the signal slowly, as it was observed with MCF-7 cells. MIA PaCa-2 cells exhibited a faster rate of cleavage of KK263 and KK249, which was therefore believed to be substrate dependent (Figure 3.5.2).

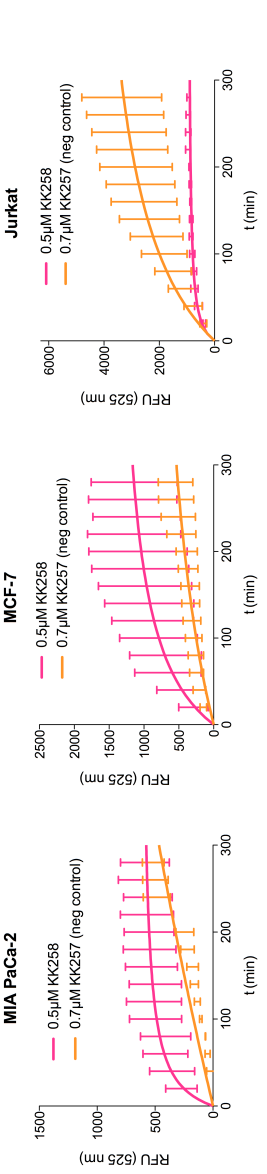

Figure 3.5.1: Cellular turnover of copolymer-supported FRET probes KK258 and negative control copolymer-substrate KK257

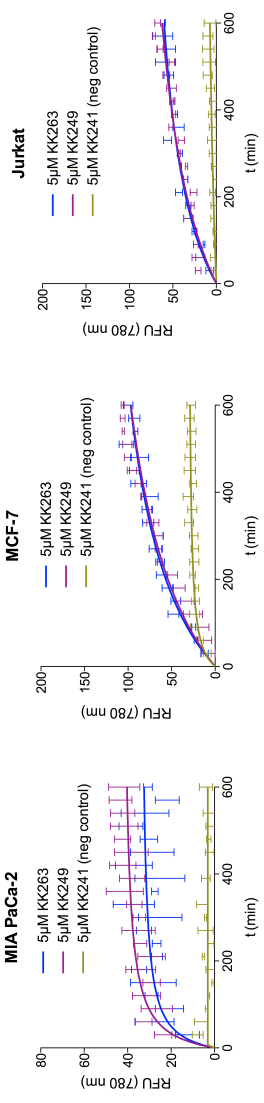

Figure 3.5.2: Cellular turnover of NIRF-copolymer-supported FRET probes KK263, KK249 and negative control probe KK241

3.5.2 Confocal Laser Scanning Microscopy of Copolymer Conjugates

The copolymer conjugates were furthermore monitored via CLSM. Cells were incubated for 5-8 h and up to 48 h with the tracers and were then observed under the microscope for substrate cleavage and internalization.

3.5.2.1 Fluorescein-labeled Copolymer-Substrate Conjugates

Due to the low loading and overall small quantities obtained of the fluorescein-labeled probes KK258 and KK257, these conjugates were only tested with MIA PaCa-2 cells for substrate conversion. Figure 3.5.3a shows the Hoechst dye, white light, and fluorescein channel, with low, but visible fluorescent signal of KK258, incubated 5.5 h with MIA PaCa-2 cells. The overlay of Hoechst and fluorescein channel also shows internalization of the probe with signal coming from intracellular vesicles. Fortunately, negative control substrate KK257 exhibits significantly less signal in the fluorescein channel (Figure 3.5.3b).

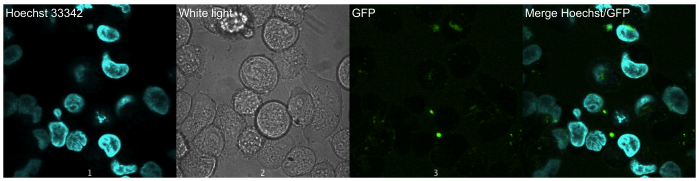

(a) MIA PaCa-2 cells with 5μM KK 258, 5.5 h

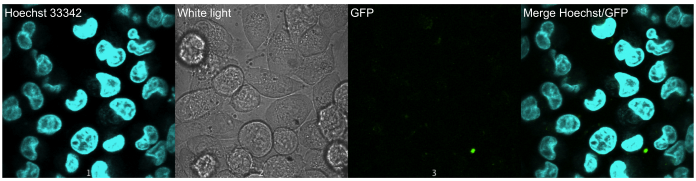

(b) MIA PaCa-2 cells with 5μM KK 257 (neg control), 5.5h

Figure 3.5.3: MIA PaCa-2 cells incubated with fluorescein-labeled conjugates

3.5.2.2 NIRF-labeled Copolymer-Substrate Conjugates

NIR-FRET conjugates KK263 and KK249 were tested with all cell lines, whereas KK241 was employed as a negative control. Images were recorded with a Cy5.5 bandpass filter set with an excitation wavelength of 633 nm, since a Cy7 filter set was not available for confocal microscopy. It must be noted that Cy7 dyes can be measured at Cy5.5 wavelengths, although the signal is not as intensive.

Substrate cleavage was observed with conjugates KK249 and KK263 with MIA PaCa-2 and MCF-7 cells (Figures 3.5.4a, 3.5.4b, 3.5.5a, and 3.5.6b). Almost no signal was observed with Jurkat cells after incubation of KK249 and KK263 for 5.5 h and 8.5 h, respectively (Figure 3.5.6). Negative control copolymer KK241 exibited some negligible fluorescence located at the cell

membrane of MCF-7 cells, whereas partly internalization was observed with MIA PaCa-2 cells, while no signal evolution was detected with Jurkat cells. The images show a dramatic effect when comparing tracer KK249 to KK263. Due to its RRR motif, KK263 is completely internalized and therefore produced a strong fluorescent signal upon substrate cleavage. KK249 lacks the RRR motif and is only partly internalized with MIA PaCa-2 cells or locates to the membrane with MCF-7 cells. However, it seems that most of the probe is washed off, when transferring the glass slide to the carrier, in order to observe the cells under the microscope. This might also explain the fact that no signal was observed with Jurkat cells under the microscope, even though *in vitro* measurements (see figure 3.5.2) suggest substrate cleavage of KK263 and KK249. Since KK263 contained some additional and potentially unbound fluorophore, the fluorophore NIR-797 was also incubated with the cells for 8.5 h by itself. Only a weak background signal was observed indicating that unbound fluorophore does not contribute to signal increase (Figure 3.5.7).
The results obtained from CLSM indicate selective NIRF-labeled MMP-11 tracer activation and internalization (KK263 and to some extent KK249). Due to intracellular activity of MMP-11, the probe can accumulate over time and a signal-to-noise increase is observed.

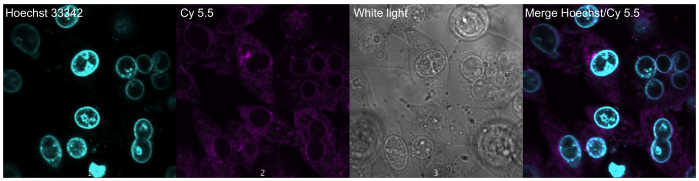

(a) MIA Paca-2 cells with 5μM KK263 8.5 h

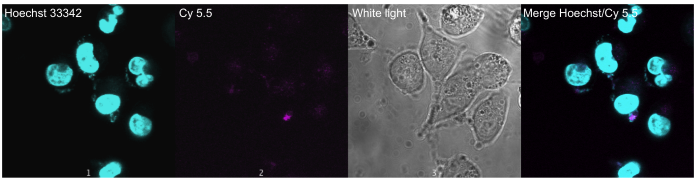

(b) MIA PaCa-2 cells with 5μM KK249 5.5h

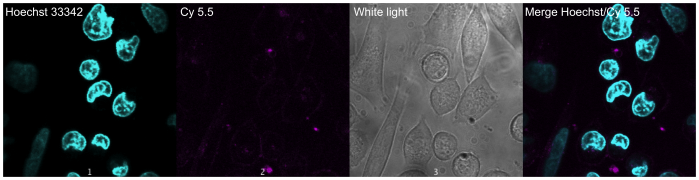

(c) MIA PaCa-2 cells with 5μM non-targeted copolymer KK241 (neg control) 5.5 h

Figure 3.5.4: MIA PaCa-2 cells incubated with NIRF-labeled conjugates

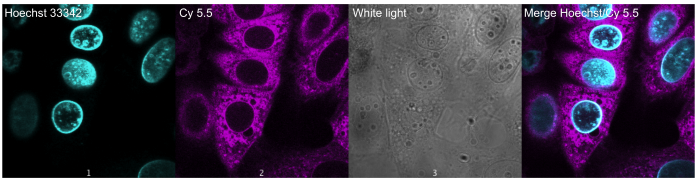

(a) MCF-7 cells with 5μM KK263 8.5 h

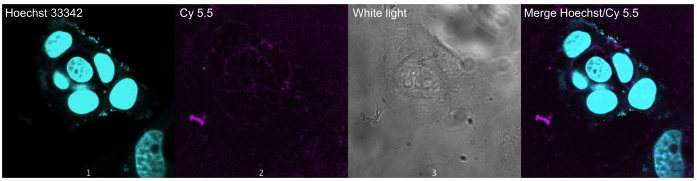

(b) MCF-7 cells with 5μM KK249 5.5h

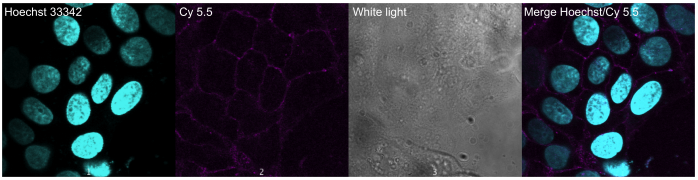

(c) MCF-7 cells with 5μM KK 241, 5.5 h

Figure 3.5.5: MCF-7 cells incubated with NIRF-labeled conjugates

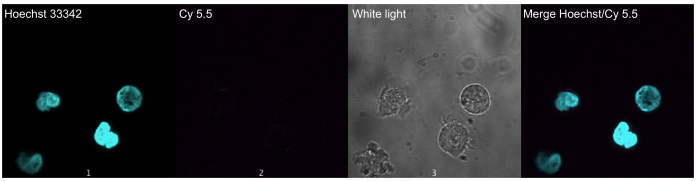

(a) Jurkat cells with 5μM KK263 8.5 h

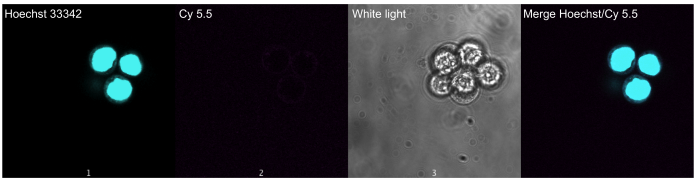

(b) Jurkat cells with 5μM KK249 5.5 h

Figure 3.5.6: Jurkat cells incubated with NIRF-labeled conjugates

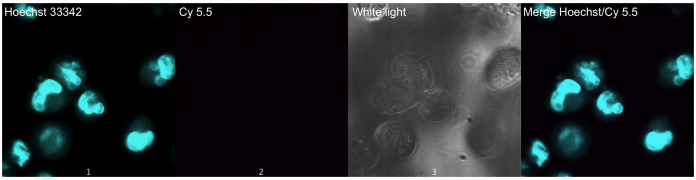

(a) MIA PaCa-2 cells with 5μM NIR-797 8.5h

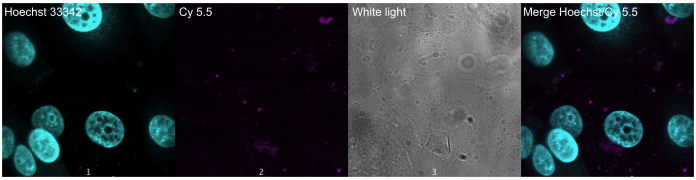

(b) MCF-7 cells with 5μM NIR-797 8.5h

Figure 3.5.7: NIR-797 dye incubated with MIA PaCa-2 and MCF-7 cells

Incubation of NIRF-labeled tracers for 48 h with MIA PaCa-2 cells also produced strongly fluorescent cells, whereas cells incubated with non-targeted copolymer control KK241 were not fluorescent after 48 h (Figure 3.5.8). A Cy7 filter set was used for these measurements confirming results from CLSM measurements recorded with a Cy5.5 filter set. These findings were encouraging and the probes were submitted for *in vivo* imaging.

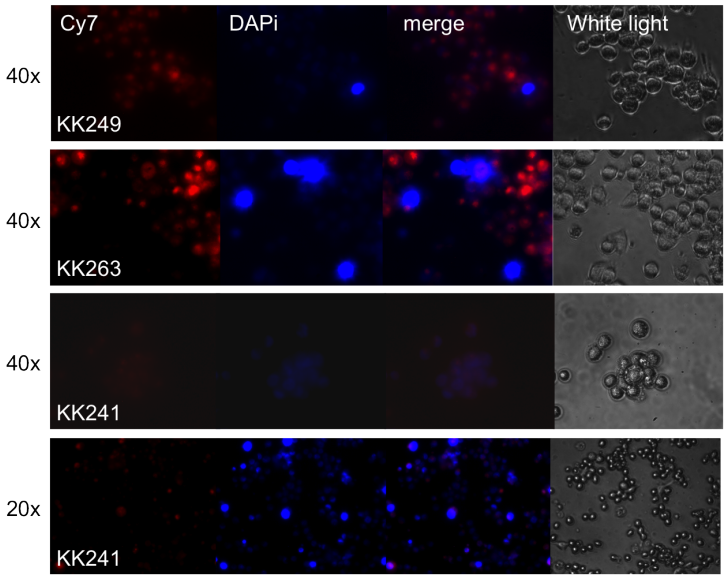

Figure 3.5.8: MIA PaCa-2 after incubation of 48 h of KK249, KK263, and non-targeted control KK241

3.6 *In vivo* Validation of Polymer-Supported Imaging Substrates

In order to further determine MMP-11 activity noninvasively *in vivo*, biodistribution, delivery, and clearance were monitored via fluorescence reflectance imaging (FRI). This imaging methodology uses 150-W halogen illuminator with Cy 7 bandpass excitation (730 nm) and emission filters (790 nm) or a GFP/FITC[6] bandpass filter set with an excitation wavelength of 470 nm and an emission wavelength of 535 nm to image anesthetized test animals. Fluorescent signals are recorded through a charge-coupled device camera as illustrated in figure 3.6.1. However, when imaging the gastrointestinal tract, the animals are preferably measured from the bottom.

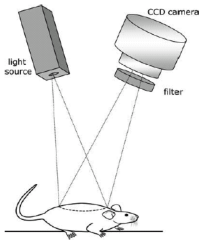

Figure 3.6.1: Fluorescence reflectance imaging (FRI)

MIA PaCa-2 xenografts were generated by subcutaneous injection of 10 x 10^6 MIA PaCa-2 cells to the breast of immunodefi-

[6] green fluorescent protein/fluorescein isothiocyanate can both be excited at an excitation wavelength around 480 nm

cient *nu/nu* mouse. Xenografts were imaged 2 to 3 weeks after injection, when a tumor of 2 to 5 mm had formed.

3.6.1 Fluorescein-labeled Copolymer-Substrate Conjuagates

3.6.1.1 MIA PaCa-2 Xenograft Biodistribution *ex vivo*

Test animals were administered with 2 nmol of fluorescein-labeled MMP-11 activatable tracer KK258 and the negative control conjugate KK257 48 h before the animals were sacrificed. Organs were explanted and fluorescence was measured via FRI. Since the fluorescein label interferes significantly with absorbing matter such as blood and skin, whole body *in vivo* measurements of xenografts yielded no fluorescent signal apart from the autofluorescence of the animal (data not shown).
The quantitative evaluation of fluorescent signal of explanted organs recorded after 48 h revealed that muscle tissue, which is usually used as a background signal, due to its low absorbtion at NIR wavelengths, exhibits a strong autofluorescence at fluorescein excitation wavelengths. Therefore, signal detected from spleen and heart were rather considered as a background reference, since both organs were hardly visible in the fluorescence image (see biodistribution images below in figure 3.6.3). The biodistribution of both fluorescein-labeled tracers shows high similarity as both probes localized to the pancreas, liver and kidneys, and lung. However, the signal detected of tracer KK258 from the tumor was somewhat stronger than the signal evolving from the tumor with KK257 uptake, even though not significantly stronger.

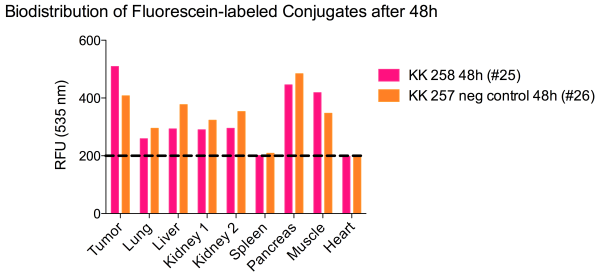

Figure 3.6.2: Biodistribution after 48 h of fluorescein-labeled conjugate KK258 and neg control KK257 (scrambled peptide sequence)

The organs are displayed in figure 3.6.3 showing the fluorescence channel on the left and the white light channel on the right. The difference of tumor uptake of tracer KK258 to KK257 is visible as negative control conjugate KK257 produced a less intensive signal of the comparably larger tumor, whereas heart and spleen are hardly visible.

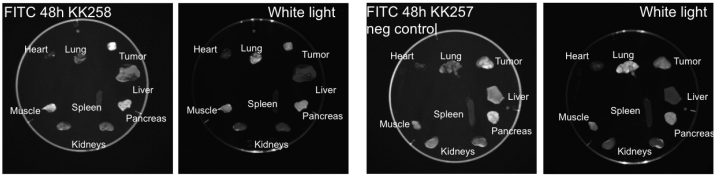

(a) KK258 (b) KK257

Figure 3.6.3: Biodistribution *ex vivo* 48 h after tail vein injection

3.6.1.2 Xenograft Imaging *in vivo* - Tumor Signal Determination

Furthermore, fluorescence intensities evolving from the tumor and muscle tissue measured *in vivo* at various time points were recorded, as it was not clear that the muscle tissue would exhibit strong autofluorescence. However, the tumor to muscle ratio as well as its difference was determined and evaluated. The tumor over muscle ratio highlights the relative strength of the evolving signal, whereas the difference of tumor and muscle tissue points out changes over time.
The signal of MMP-11 targeted tracer KK258 increased relative 83-fold by means of RFU signal intensity over the first six hours and increases 1.5-fold in strength. The signal stayed constant for up to 48 h, while negative control conjugate KK257 displayed a strong signal 30 min after injection and steadily decreased from there with a minimum signal below the muscle autofluorescence at 24 h. The signal in the tumor of KK257 increased over the next 24 h and yielded a 1.2-fold ratio at 48 h in comparison to muscle tissue. However, if fluorescence obtained from the spleen or heart at 48 h is used as a reference signal, then the tumor signal of KK258 is 2.5-fold stronger, whereas the tumor signal evolving from KK257 is only 2 times stronger (represented by dots in the graph of figure 3.6.4).

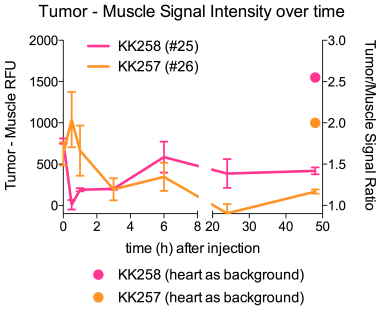

Figure 3.6.4: Tumor signal over time of substrate copolymer conjugates KK258 and neg control KK257 (scrambled sequence)

The results show that the conjugates were successfully taken up by tumor tissue and accumulated up to 48 h. The best signal difference of targeted MMP-11 tracer KK258 and its negative control KK257 was reached after 24 h. Still, the strength of the signal is rather weak, as it approached a maximum of 2.5-fold, when employing signal from spleen or heart as background reference. Additionally, more time points in between 6 h and 24 h might elucidate whether the signal of tracer KK258 further increases during this time frame, while the KK257 signal decreases, thereby creating a more distinct difference of specific cleavage of MMP-11 targeted copolymer-substrate conjugate KK258 in comparison to the negative control conjugate KK257. Furthermore, it must be considered that other controls might be more reasonable to address specificity questions. For example, implantation of a second tumor with down-regulated MMP-11 expression or blocking with an MMP-11 active inhibitor might elucidate the

application potential of this tracer better for the early detection of pancreatic lesions.

3.6.1.3 Transgenic Mice Imaging *in vivo*

In order to visualize fluorescein-labeled copolymer-substrate conjugates *in vivo*, a transgenic mouse model was utilized by imaging fluorescence invasively. Invasive imaging needed to be pursued with fluorescein-labeled probes, due to the low penetration depth of fluorescein in tissue, as well as correlating autofluorescence from surrounding tissue.

Wagner *et al.* found in 2001 that a tumor progression model for pancreatic ductal adenocarcinoma using TGF-α overexpressing mice crossbred with p53[7] null mice yielded accelerated tumor growth to a rate similar to that found in humans.[136]
Therefore, transgenic mice with a TGF-α/p53^{+}/$^{-}$ gene mutation leading to pancreatic tumor formation and healthy control mice (provided by Dr. Dieter Saur's group, Technische Universität München) were anesthetized and 3 nmol of fluorescein-labeled MMP-11 targeted copolymer-substrate conjugate KK258 were administered by retrobulbar injection 14 h prior to measurement.
The next day, mice were anesthetized, a small left abdominal incision was made, and spleen and pancreas were displayed by a gentle pull, followed by fluorescence measurements. It must be noted that the transgenic mouse imaged had not yet developed a tumor, the pancreas did not show any signs of cancerous tissue. However, excitation under a fluorescence microscope at 483 nm

[7] tumor suppressor that can be activated to induce apoptosis of diseased cells

for 300 s yielded a strongly fluorescent pancreas of the transgenic mouse, whereas no signal of the pancreas was observed with healthy control mice. Microscopic images taken show the fluorescein channel on the left and white light images on the right. The autofluorescent intestine is observed in both fluorescence images represented by a yellow signal, whereas the pancreas exhibits a more greenish fluorescence of fluorescein-labeled conjugate KK258 (Figure 3.6.5).
Even though no tumor had formed in the transgenic test animal, fluorescein labeled MMP-11 copolymer-substrate conjugate accumulated in the pancreas. The control mouse showed no signal within the pancreas after 14 h.
Although, these images show the successfull testing of precancerous lesions leading to PDAC in the living organism, the mice needed to be imaged invasively, due to low penetration depth of the fluorescein fluorophore. Since early detection of pancreatic cancer is supposed to be a noninvasive method, focus was placed on the NIRF-labeled copolymer-substrates conjugates for full body noninvasive imaging *in vivo*.

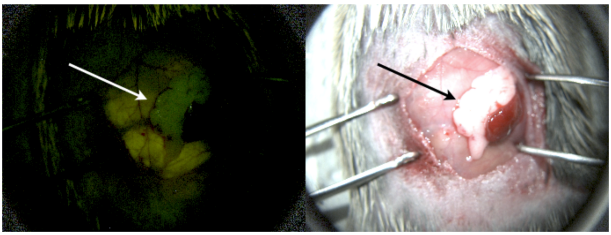

(a) #10359 transgenic mouse 3 nmol KK258

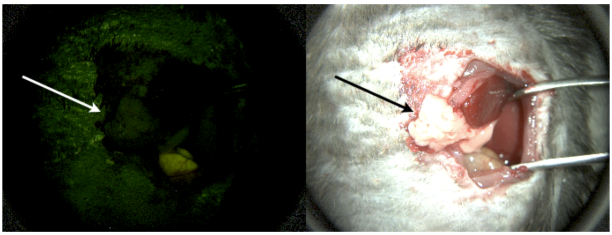

(b) #9711 control mouse with 3 nmol KK258

Figure 3.6.5: Administration of KK258 14h after retrobulbar injection

3.6.2 NIRF-labeled Copolymer-Substrate Conjugates

In order to investigate uptake, clearance, and accumulation within the body of NIRF-labeled copolymer-substrate conjugates, MIA PaCa-2 xenografts as well as healthy control mice were imaged at different time points after injection of the NIRF-labeled tracers.

3.6.2.1 MIA PaCa-2 Xenograft Biodistribution *ex vivo*

Healthy control mice and MIA PaCa-2 xenografts were anesthetized with isoflurane gas, while being imaged from below with white light or a filter set for cyanine dyes (Cy7) for 30 s. 2 nmol of MMP-11 tracers KK249 (NIR-FRET), SM P 117 (self-quenched), both lacking a RRR motif, KK263 (NIR-FRET with RRR motif) and non-targeted control copolymer KK241 were administered to the test animals via tail vein injection and fluorescent measurements *in vivo* were recorded right after injection, 30 min, 1 h, 3 h, 6 h, 24 h, and 48 h.

Clearance studies of tracer KK249 and SM P 117 in healthy control mice indicated early uptake in the bile rather than the kidneys, whereas this signal is lost after about 10 h (KK249 is represented in figure 3.6.6; see appendix 6 on page 257 for further clearance studies). Non-targeted control KK241 exhibits an early uptake in the bile for up to 3 h, before the signal diminished. In general, unpolar, hydrophobic substances locate to the bile and are excreted from there. It would be interesting whether KK263, bearing the RRR motif, yields a less intensive signal in the bile, due to increased hydrophilicity. Unfortunately, the bile of tested healthy control mice was not examined with

tracer KK263 and this comparison could not be made.
Furthermore, all probes exhibited a significant signal in the liver. This signal may be due to the rather high polydispersion index (PDI) of the applied copolymer. Renal clearance cutoff is estimated at about 55 kDa, larger substances accumulate in the liver and are cleared by biliary excretion.[137] The copolymer has a mean weight of about 40 kDa, but a PDI of roughly 3, suggesting that most of the probe would be cleared via biliary excretion, while the smaller copolymer parts and especially cleaved substrate would be excreted via renal clearance. In fact, the kidneys and partly the bladder were visible with all probes. In summary, targeted probes KK249 and SM P 117 were circulating longer within the system than non-targeted copolymer KK241 that was nearly cleared after 6h. All signal evolving up to 24 h is therefore considered as unspecific cleavage and following measurements focused on values obtained at 24 h or later. In that time frame only liver and kidneys deliver unspecific signal contribution.

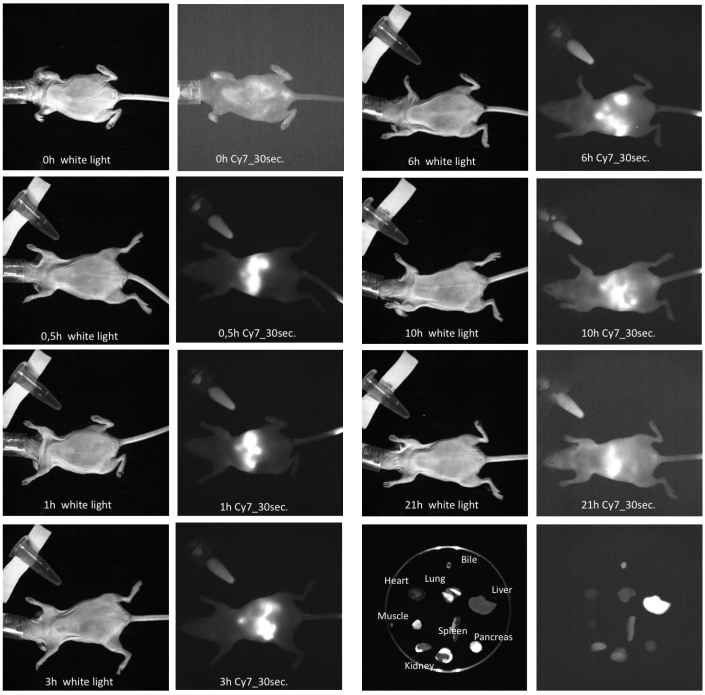

Figure 3.6.6: *In vivo* clearance study for NIR-FRET conjugate KK249; Biodistribution *ex vivo* 21 h after tail vein injection

Furthermore, a biodistribution of healthy control mice at varying time points and one xenograft at 48 h was recorded *ex vivo* and fluorescence of explanted organs was determined and quantified. The results are shown in figure 3.6.7 and indicate delivery to the bile (only shown for KK249), liver, kidneys, spleen, lungs, and pancreas. Signal recorded from non-fluorescent muscle tissue is considered as background signal.
All injected tracers exhibited a background fluorescence of about

100 RFU. NIR-FRET tracer KK249 without RRR motif additionally showed the strongest uptake of probe in the liver, whereas conjugates KK263 (with RRR motif), self-quenched SM P 117, and non-targeted KK241 displayed a slight increase in liver signal from 24 h to 48 h. Moreover, the kidney signal increased from 21 h to 48 h slightly for tracers KK249 and control KK241 and strongly for SM P 117. The delayed liver and kidney signals might point towards a late, specific cleavage and its excretion, due to accumulation within the tumor tissue (48 h fluorescence was detected of xenograft). Unfortunately, also non-targeted tracer KK241 showed an increased fluorescent signal from tumor tissue. This observation was however not surprising, since copolymers are known to accumulate in tumor tissue, due to a phenomenon termed "the enhanced permeability and retention" (EPR) effect of solid tumors.[125, 138] The enhanced vascular permeability of tumor tissue allows long circulating compounds to accumulate passively in the interstitium of solid tumors, due to the lack of a functioning lymphatic drainage system within this type of tissue.[139, 140, 141] Although, tumor signal intensities of xenografts tested *ex vivo* after 48 h were similar throughout all tracers, it was shown that the developed NIRF-labeled tracers locate specifically to the tumor or are excreted via renal or biliary clearance. Even though the signal-to-background ratio is not strong enough at this stage, these results point towards a refinement of the conjugates through copolymer and substrate optimization that might increase overall determined signal strength.

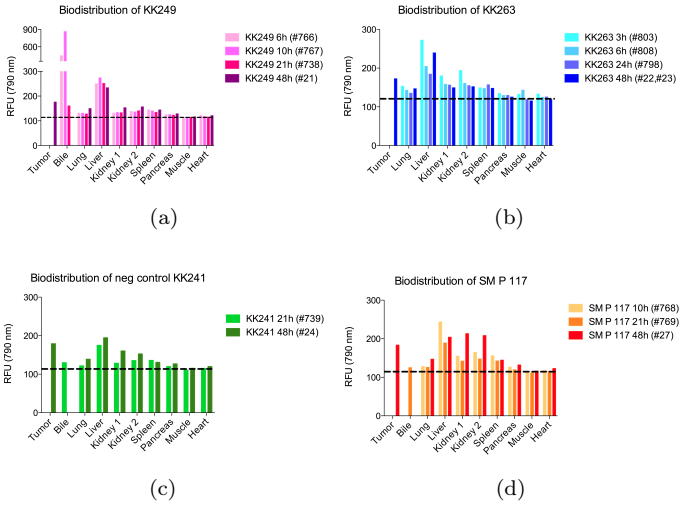

Figure 3.6.7: Biodistribution of a) KK249 (intra-quenched, without RRR motif) and b) KK263 (intra-quenched with RRR motif) c) KK241 as neg control and d) SM P 117 (inter-quenched) at different time pointsat different time points

Explanted organs measured 48 h after injection are displayed in the following figures 3.6.8, 3.6.9, and 3.6.10. The explanted tumor is fluorescent will all tracers injected. The liver is also strongly fluorescent with all tracers, whereas SM P 117 and KK241 displayed an increased signal of the kidneys, pointing towards a delayed activation of tracer, due to accumulation within the targeted tissue. Muscle tissue signal was however hardly observed with all injected tracers.

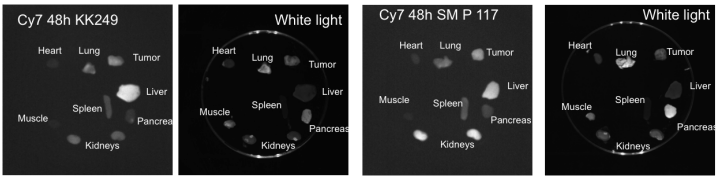

(a) KK249 (b) SM P 117

Figure 3.6.8: Biodistribution *ex vivo* of NIR-FRET conjugate KK249 and self-quenched analog SM P 117 48 h after tail vein injection

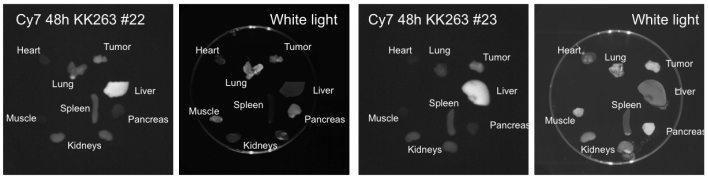

(a) KK263 nr. 22 (b) KK263 nr. 23

Figure 3.6.9: Biodistribution *ex vivo* NIR-FRET conjugate KK263 48 h after tail vein injection

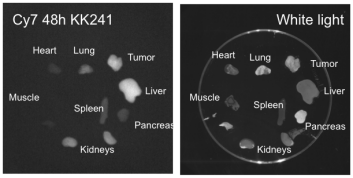

(a) KK241 (non-targeted)

Figure 3.6.10: Biodistribution *ex vivo* of non-targeted copolymer KK241 48 h after tail vein injection

Since large quantities of the tracers are "lost" to unspecific cleavage and excretion in the first 20 h, employing a more narrow distributed copolymer of 60 kDa for prolongued circulation with a PDI close to 1, employing a self–quenched substrate as the targeting functionality, might further increase the signal-to-background ratio, due to faster accumulation in tumor tissue therefore decreasing unspecific cleavage and fast excretion via the kidneys and bile. Moreover, optimization of the substrate sequence might further increase specificity for MMP-11 and might thereby also increase uptake to the desired overexpressing tissues.

3.6.2.2 Xenograft Imaging *in vivo*

The test animals were furthermore imaged *in vivo* after injection of the NIRF-labeled conjugates and after 30 min, 1 h, 3 h, 6 h, 24h and 48h. The tumor signal was recorded in accordance with muscle tissue signal as a background reference. Figure 3.6.11 displays the signal development as the difference of tumor to muscle over the specified time area, whereas the ratio of tumor to muscle signal determines the strength of the recorded signal. It can be seen that a strong signal increase evolved for all tracers 30 min after injection. The signal decreased for self-quenched SM P 117 and slowly increased again after 24 h. NIR-FRET conjugate KK249 and one of the xenografts that was imaged with NIR-FRET conjugate with RRR motif KK263 (#23) displayed a constant signal in the tumor during the first 6 h and showed a strong increase from 24 h to 48 h. The second xenograft that was imaged with KK263 (#22) exhibited rather low fluorescence in the tumor and displayed a constant signal level over the given time points. The non-targeted copolymer KK241 rather showed

a decrease in signal evolution. The strongest difference in tumor signal strength is reached after 48 h where KK241 had a signal strength of 1.25-fold of background signal, while KK249, SM P 117, and KK263 (#23) displayed a 1.4-fold signal ratio of tumor over muscle tissue.

Further time points after 48 h would clarify whether MMP-11 targeted conjugates further accumulate in the tumor, while non-targeted control conjugate KK241 is excreted. If this were true, then that would intensify the signal-to-noise ratio as well as the specificity of the evolving signal.

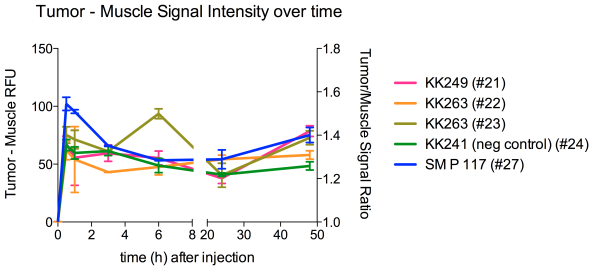

Figure 3.6.11: MIA PaCa-2 xenograft imaging; Trends of tumor signal emission

The distribution and clearance of the tracers in MIA PaCa-2 xenografts were recorded and are depicted below (Figures 3.6.12, 3.6.13, 3.6.14, 3.6.15, and 3.6.16). Tumors were highlighted with red circles in the white light channel images.

Tumor signal evolution was observed after 24 h for NIR-FRET tracers KK249 and KK263, while self-quenched SM P 117 exhibited tumor fluorescence already 30 min and 1 h after injection and for a second time after 24 h with significant increase of flu-

orescence up to 48 h. Non-targeted copolymer KK241 showed weak tumor signal evolution 1 h after injection that steadily increased up to 48 h.

The tracers can be best analyzed by comparing images taken after 24 h and 48 h. The images were false colored in order to emphasize signal strength. NIR-FRET conjugate KK249 showed a distinct signal of the tumor at 24 h that increased strongly up to 48 h. The tumor is easily locatable. Singly labeled self-quenched conjugate SM P 117 evolved a strong tumor signal after 48 h, displaying selective tissue cleavage of the injected tracer. NIR-FRET conjuagte KK263 that includes the hydrophilicity motif RRR at the N-terminus of the substrate exhibited varying results. Xenograft 1 did not show specific localization of the evolving signal, as there are more than one highlighted parts of the animal. Xenograft 2 displayed a tumor signal only after 48 h, although this signal was also not very specific, as there are other signal intensive parts in that area. Non-targeted copolymer KK241 exhibited a more diffuse tumor signal, although it intensified from 24 h to 48 h. Still, the uncorrected *in vivo* tumor signal was best distinguishable of tracers KK249 and especially SM P 117.

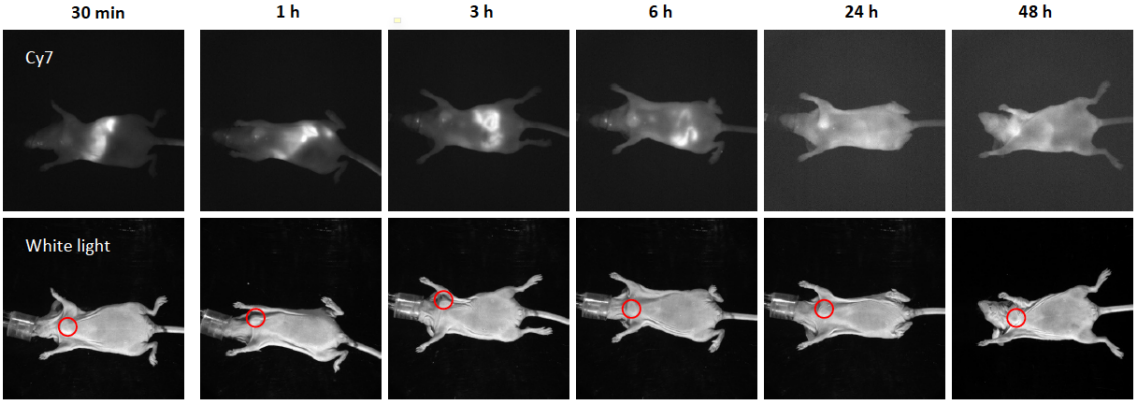

Figure 3.6.12: MIA PaCa-2 xenograft imaging of NIR-FRET conjugate KK249; red circle marks tumor

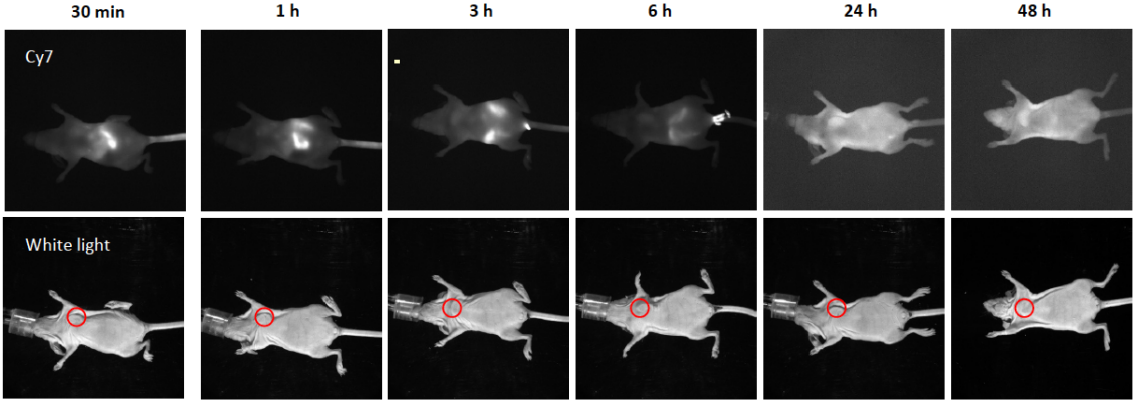

Figure 3.6.13: MIA PaCa-2 xenograft imaging of NIR-FRET conjugate with RRR motif KK263 nr. 22; red circle marks tumor

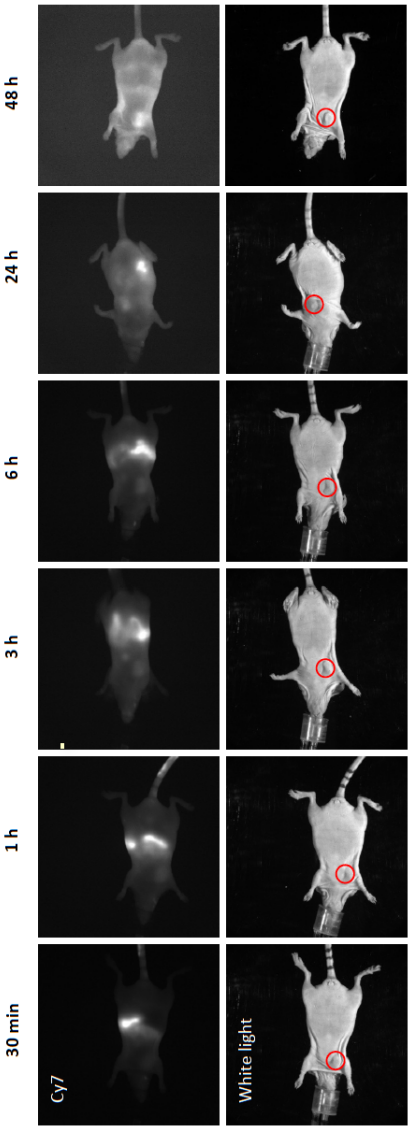

Figure 3.6.14: MIA PaCa-2 xenograft imaging of NIR-FRET conjugate with RRR motif KK263 nr. 23; red circle marks tumor

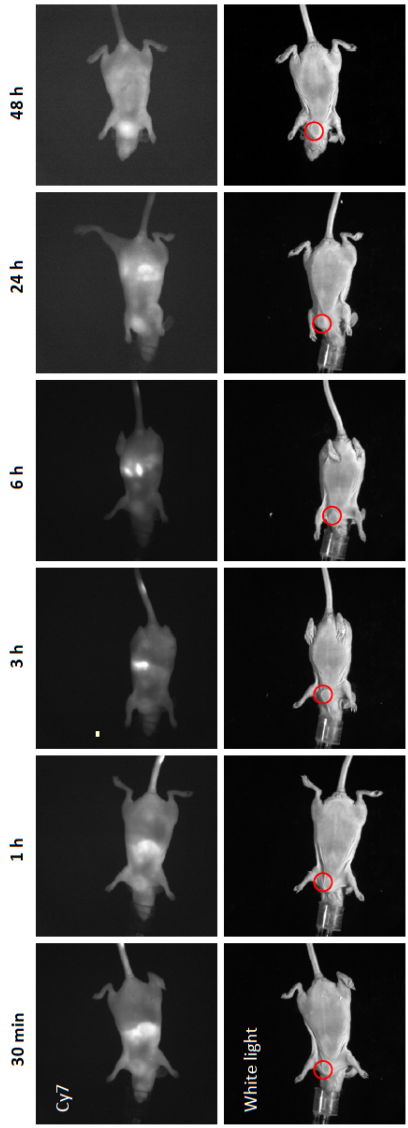

Figure 3.6.15: MIA PaCa-2 xenograft imaging of self-quenched conjugate SM P 117; red circle marks tumor

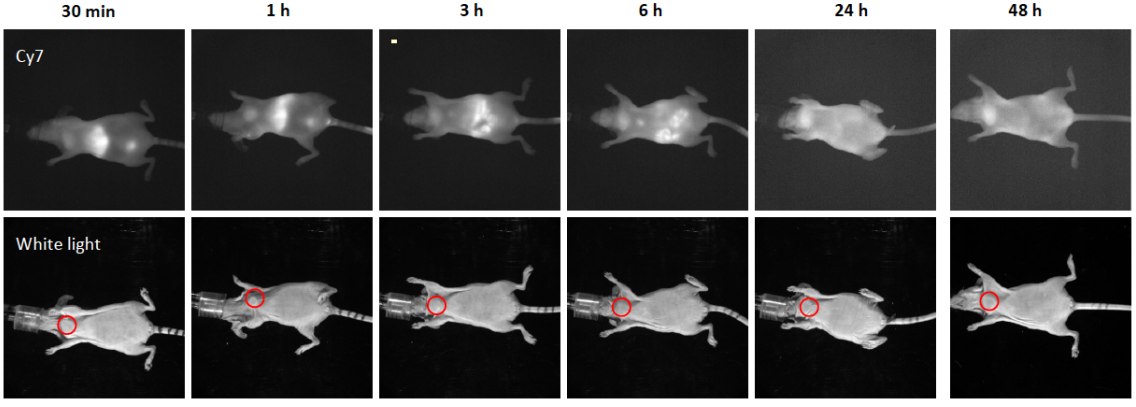

Figure 3.6.16: MIA PaCa-2 xenograft imaging of non-targeted copolymer KK241; red circle marks tumor

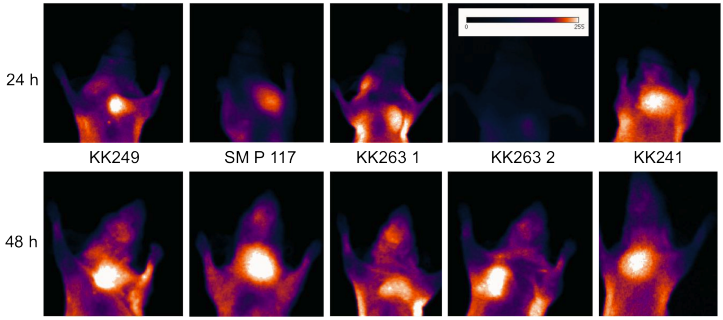

Figure 3.6.17: False color images of xenografts recorded 24 h and 48 h after tail vein injection

The presented *in vivo* measurements show first results obtained with the novel NIR-FRET substrate conjugates synthesized. In order to determine the best variation of copolymer and substrate e.g. size of copolymer, FRET or self-quenched substrate, hydrophilicity admustments, and sufficient controls further investigations as well as more xenograft measurements are needed in order to conclude the significance of the mesurements presented. Furthermore, tracers need to be optimized in order to increase the overall signal strength within the tumor tissue. Additionally, more efficient controls include the implantation of a MMP-11 down-regulated tumor to the MIA PaCa-2 xenograft or the blocking with an MMP-11 active inhibitor.
However, all tracers will be submitted for trangenic mice imaging to further elucidate uptake of these tracers to cancerous pancreatic tissue. In summary, it was shown that the developed novel NIRF-labeled copolymer-substrate conjugates KK249 and SM P 117 were successfully employed to detect pancreatic tumors of xenografts *in vivo*.

3.7 Synthesis of Cryptophane-A-labeled Copolymer-Substrate Conjugates

Due to difficult signal allocation of 2-D *in vivo* imaging measurements with NIRF-labeled tracers, a refined probe for MRI was designed and synthesized. It has been shown by Wei *et al.* that coupling of a Cryptophane-A cage to a protease-susceptible peptide resulted in a 0.5 ppm chemical shift of hyperpolarized (hp) ^{129}Xe when comparing cleaved peptide with intact peptide (Figure 3.7.1 and 3.7.2).[142] It would therefore be possible to monitor MMP-induced cleavage by MRI, due to hp ^{129}Xe sensitivity to its environment.

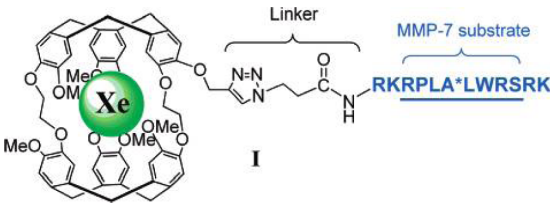

Figure 3.7.1: Protease suscetible peptide labeled with Cryptophane-A

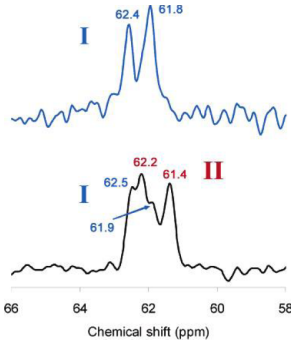

Figure 3.7.2: Tracer design with Cryptophane-A shows chemical shift of ^{129}Xe of intact and cleaved peptide sequence with chemical shift differences of I intact peptide (blue) and II cleaved peptide (red) [142]

Consequently, Cryptophane-A needed to be introduced to the MMP-11 substrate sequence. In a trial synthesis the substrate sequence of SM P 148 was reconstructed on a Rink amide resin without the FRET pair. SM P 148 was chosen since the sequence showed high cleavage potential with MMP-11, but suffered from inefficient FRET quenching. Since the FRET pair is replaced by the Cryptophane-A cage for these ^{129}Xe imaging prototypes, SM P 148 was considered an interesting sequence.
Instead of the fluorescein - dabcyl FRET pair, a lysine was introduced to the position that was occupied by fluorescein. The peptide sequences were synthesized via standard Fmoc-mediated solid phase synthesis. The cysteine-modified sequence for copolymer-conjugation was cleaved off the resin, loaded to pHPMA by NCL and was then coupled in solution to Cryptophane-A.
Coupling of Cryptophane-A **22** to the peptide **21** was achieved in solution, employing 2 eq. of Cryptophane-A, and 4 eq. of col-

lidine for every eq. of peptide, dissolved in dry DMF, whereas Cryptophane-A was presolved in dry THF (Figure 3.7.3).

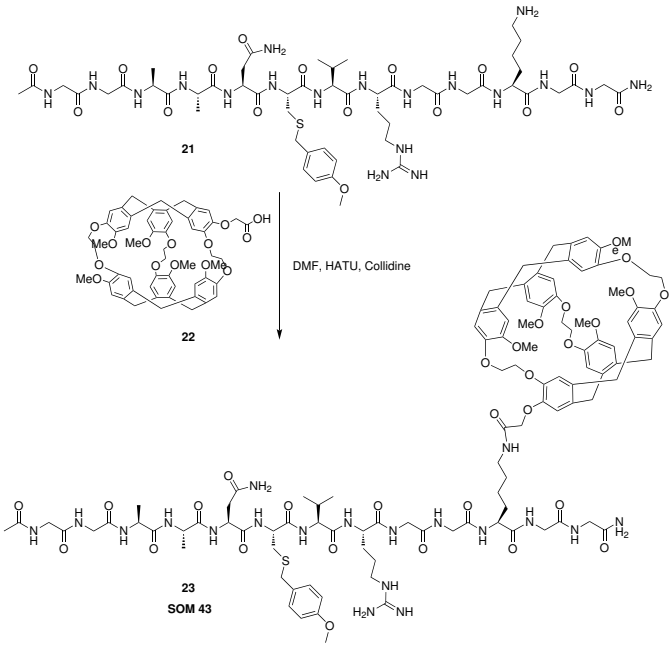

Figure 3.7.3: Cryptophane-A coupling in solution

The overall yields after Cryptophane-A coupling for the described non-fluorescent sequences SOM 43 **23**, SOM 44 as its cleavage standard, and cysteine modified sequence SOM 28 for copolymer conjugation, are given in table 3.7.1. Yields are higher with shorter sequences, basically due to the missing isolation step after resin cleavage.

Since a FRET pair was not included in this sequence, MMP-11 activity could not be monitored via fluorescence. Therefore,

Entry	Sequences	Name	Yield before coupling (%)	Yield after coupling (%)	Polymer Name
1	Ac-C(MeOBn)VRGGK(CryptoA)GG-NH_2	SOM 44	97	17	-
2	Ac-GGAANC(MeOBn)VRGGK(CryptoA)GG-NH_2	SOM 43	12	7	-
3	H-CGGAANC(MeOBn)VRK(NH_2)GG-NH_2	SOM 28	17	5	KK245

Table 3.7.1: Sequences and yields for xenon caged substrates

MMP-11 substrate sequence SOM 43 was validated via LC/MS-TOF for substrate cleavage after incubation with MMP-11 and MMP-14. SOM 43 in assay buffer was recorded as a negative control. The intact substrate shows a retention time of exactly 14 min. The cleavage product is shifted approximately by 0.2 min in retention time, due to similar hydrophobicity of the attached cage. The product peak is evolving in between the substrate peak at 14 min and the oxidized substrate peak at 13.7 min. Incubation with MMP-11 yielded only moderate substrate cleavage, whereas MMP-14 yielded a majority of cleaved substrate in the same time (Figure 3.7.4).

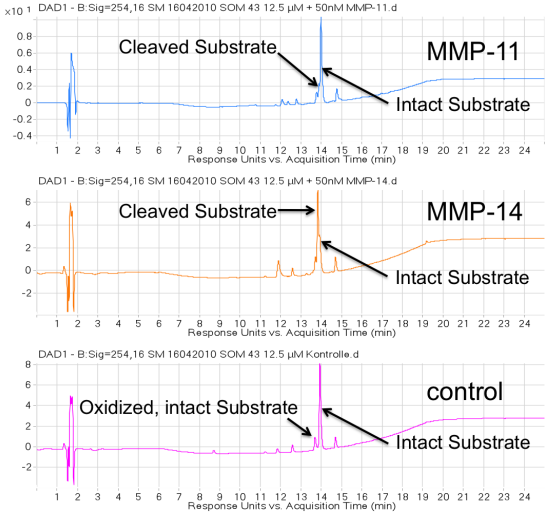

Figure 3.7.4: LC/MS-TOF validation of MMP-11 cleavable substrates sequence labeled with Cryptophane-A

SOM 43 and its cleaved analog SOM 44, as well as the pHPMA conjuagted Cryptophane-A labeled substrate KK245 will now be

passed on to Dr. Leif Schröder, Leibniz-Insitut für Molekulare Pharmakologie (FMP) for first hp ^{129}Xe chemical shift experiments. Hopefully, the chemical shift of cleaved substrate will deviate from the chemical shift measured with intact substrate. Furthermore, a larger chemical shift is anticipated, when comparing cleaved substrate with intact copolymer-substrate conjugate. This would allow clear differentiation of cleaved to intact probe *in vivo* and would facilitate accurate localization of cleavage of the probe. Furthermore, the time frame of cleavage could be observed and measured, employing these novel imaging probes.

Moreover, a multiplexing probe was designed in order to track the probe visually for cellular experiments and later on also for *in vivo* measurements. The synthesis had to be modified from the standard protocol. C-terminally labeled 5-aminofluorescein 2-chlorotrityl resin was utilized to couple glycine in the first step as described previously. However, in the next step Fmoc-3-((1-(4,4-dimethyl-2,6-dioxocyclohexylidene)-3-methylbutyl)amino)-L-alanine (Fmoc-Dap(ivDde)-OH) was introduced to the sequence rather than a second glycine. ivDde was used as a protecting group rather than Dde, because protection group transfer to another unprotected amine within the sequence has been reported not to take place with ivDde, due to steric hinderance of the inroduced isopropyl group to the electrophilic center of the 2,6-dioxocyclohexylidene system. The peptide sequence is constructed as described previously with regular coupling conditions employing 3 eq of each amino acid, HOBT, and DIC while the Fmoc protecting group was deblocked twice for 10 min with 20 % piperidine in DMF. For N-terminal cysteine sequences Boc-Cys(Trt)-OH was employed instead of Fmoc protected cysteine,

since a second Fmoc group would be introduced to the side chain later on.

The ivDde group of **24** is deprotected with 10 % hydrazine in DMF at RT four times for 10 min (Figure 3.7.5). A Kaiser test approved the deblocked amino group of the Dap residue. Another Fmoc-Dap(ivDde)-OH is introduced in order to create a branching within the side chain to yield **25**. The newly introduced Dap residue was Fmoc deprotected with 50 % 1,8-diazabicyclo[5.4.0]undec-7-en (DBU) and 10 % piperidine in DCM once for 30 min. Due to the strong hydrophobic character of Cryptophane-A, Fmoc-11-amino-3,6,9-trioxaundercanoic acid (Fmoc-PEG_3-OH) (5 eq) was introduced with 5 eq HATU and 10 eq of collidine in DMF, overnight at RT in order to increase solubility. The Fmoc group of the attached PEG chain was deblocked and the resulting free amine was acetylated, yielding **26**. The second ivDde group is then deblocked, again with 10 % hydrazine in DMF four times for 10 min and the prepared sequence **27** is cleaved off the resin to yield **28**, employing the standard cocktail for C(MeOBn) containing substrates (see table 3.2.3 on page 75). Coupling with Cryptophane-A in solution in a dry DMF/THF mixture yields the multiplexed-labeled tracer **29**.

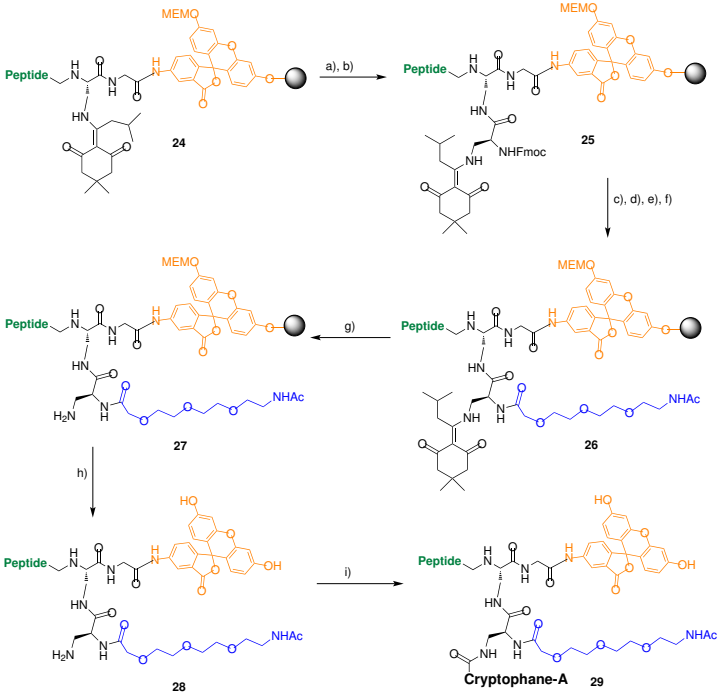

Figure 3.7.5: Multiplexing probe generation: Cryptophane-A labeled FRET substrate a) 10 % hydrazine in DMF, 4 x 10 min, RT; b) Fmoc-Dap(ivDde)-OH, HATU, collidine, DMF, overnight, RT; c) 50 % DBU, 10 % piperidine in DCM, 30 min, RT; d) Fmoc-PEG_3-OH, HATU, collidine, DMF, overnight, RT; e) see c); f) acetic anhydride:DIPEA:DCM 1:1:1, 10 min, RT; g) see a); h) DCM:TFA:Phenol:H_2O:EDT:TIS 50:40:1(w/v):4:2.5:2.5, 24 h, RT; i) Cryptophane-A, HATU, collidine, THF:DMF 1:4, overnight, RT

Cryptophane-A coupling was prepared in solution as decribed in the previous section. Table 3.7.2 summarizes yields obtained be-

fore and after Cryptophane-A labeling in case of entry 1. Entries 2 and 3 were obtained only at a crude yield even after HPLC. However, entry 3 consisted mainly of singly oxidized substrate and desired product. Therefore, SM P 188 was loaded to pHPMA as obtained. Entry 2 was also used as obtained and was furthermore coupled to Cryptophane-A. These substrates can be isolated more efficiently after attachment of the hydrophobic cage to the sequence. Before cage-coupling substrates are too polar and afford special polar columns in order to isolate the sequences via HPLC.

The general assembly of the Cryptophane-A-labeled FRET substrate **30** is shown in figure 3.7.6. The MMP-11 sequence is represented in green, the FRET pair is highlighted in orange and red, whereas hydrophilicity adjustments are shown in blue. The pink N-terminal cysteine is used for conjugation to pHPMA, whereas the Cryptophane-A cage is represented in black.

Entry	Sequences	Name	Before coupling (%)	After coupling (%)	Polymer Name
1	Ac-C(MeOBn)RMDap(Dap(PEG$_3$-Ac)CryptA)G-Fluo	SM P 185	9	7	-
2	Ac-GRRRK(Dabcyl)GGAANC(MeOBn)RMDap(Dap(PEG$_3$-Ac)CryptA)G-Fluo	SM P 187	5	-	-
3	H-CGRRRK(Dabcyl)GGAANC(MeOBn)RMDap(Dap(PEG$_3$-Ac)CryptA)G-Fluo	SM P 188	12	-	KK275

Table 3.7.2: Yields of multiplexing probes for FRET and hp ^{129}Xe imaging

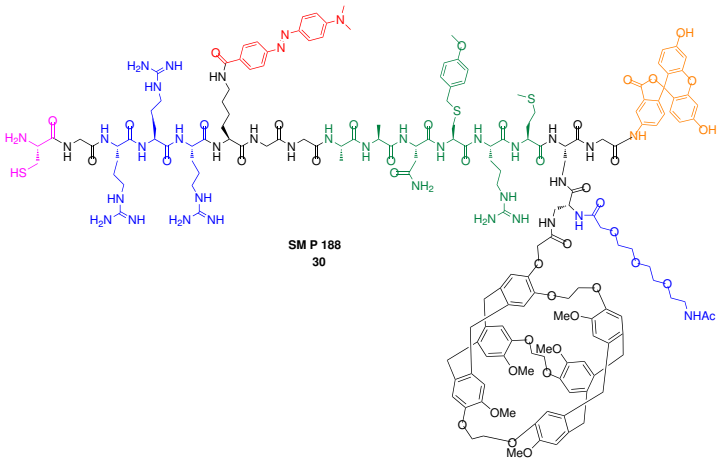

Figure 3.7.6: General multiplexing substrate

Conjugation to pHPMA should, in principle, further increase the chemical shift of intact copolymer conjugated substrate and cleaved substrate. Therefore, special attention was laid on the design of the substrate, as the distance from Cryptophane-A to the cleavage site is as near as possible and furthermore, the linker is rather rigid and short to ensure spatial proximity to the cleavage site, since this might critically influence chemical shift behavior. Figure 3.7.7 indicates the anticipated methodology.

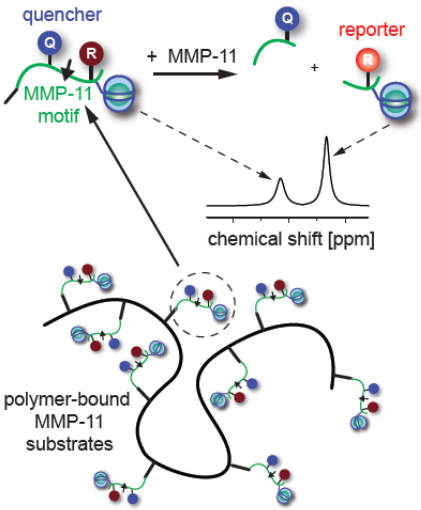

Figure 3.7.7: Copolymer conjugated FRET substrate for hyperpolarized xenon imaging of MMP-11 activity [91]

4 Conclusion and Outlook

Matrix metalloprotease 11 (MMP-11) was identified as a diagnostic biomarker for the early detection of pancreatic cancer by means of a literature search for genes overexpressed in early pancreatic intraepithelial neoplasia stages 2 and 3 (PanIN 2 and 3) and in invasive adenocarcinoma. MMP-11 was validated for pancreatic ductal adenocarcinoma (PDAC) overexpression by Western Blot with 8 tumor tissue samples and 8 pancreatic control tissues, confirming significant expression in PDAC (P=0.0027) (Figure 4.0.1).

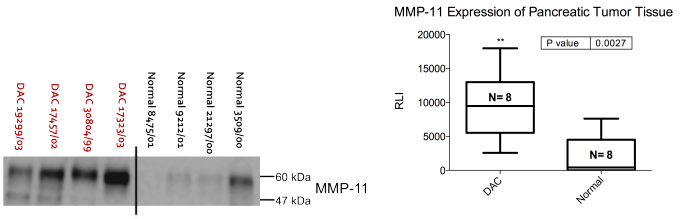

(a) MMP-11 Western Blot (b) Quantitative Validation

Figure 4.0.1: Patient's PDAC and normal tissue tested in Western Blot

Combination of published substrate sequences for MMP-11 containing unusual amino acid residues yielded a substrate library of

17 sequences that were engineered as *in vitro* and *in vivo* imaging agents with increased activity and selectivity for MMP-11. Sequences that were adapted from the literature are highlighted in gray in figure 4.0.1.

Entry	Sequence
1	GGAANC(MeOBn)RMGG
2	GGYAEC(MeOBn)RMGG
3	GGAANLRMGG
4	GGYAELRMGG
5	GGAANC(MeOBn)VRGG
6	GGYAEC(MeOBn)VRGG
7	GGAANLVRGG
8	GGYAELVRGG
9	GGPLAC(MeOBn)WARGG
10	GGAANC(MeOBn)WARGG
11	GGYAEC(MeOBn)WARGG
12	GGPLALWARGG
13	GGAANLWARGG
14	GGYAELWARGG
15	GGNAAC(MeOBn)RMGG
16	GGYAENGG

Table 4.0.1: Sequence library of peptidic substrates for MMP-11

Fluorescein-dabcyl was chosen as a Förster resonance energy transfer (FRET) pair. Dabcyl quenches fluorescein fluorescence when connected by a peptide sequence, due to spatial proximity. Cleavage of the FRET labeled peptide sequence by MMP-11 results in dequenching of fluorescein fluorescence and therefore in a significant signal increase. Figure 4.0.2 presents the construction of the general FRET substrate, highlighting the FRET pair in red and orange while MMP-11 specific sequence is shown in

green. Two glycine spacers flank the sequence, and three arginine residues near the N-terminal were introduced to increase solubility. The N-terminal glycine was added as a spacer for further modifications.

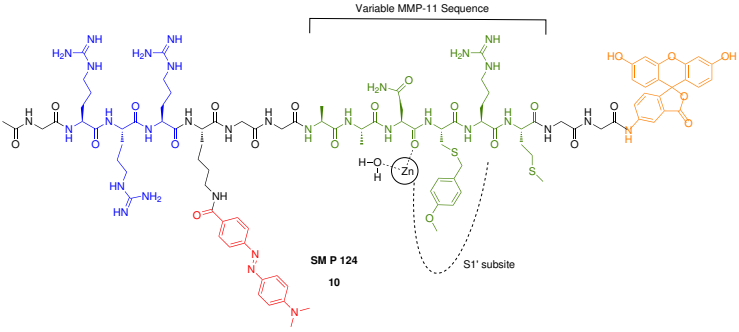

Figure 4.0.2: General substrate assembly

Substrate sequences were evaluated for their activity by measuring fluorescence increase over time in a FRET assay and via LC/MS-TOF measurements. Cleaved substrate was identified by mass in 4 out of 17 sequences tested. The active sequences were further compared with MMP-11 and MMP-14 and SM P 124 (Ac-GRRRK(dabcyl)GGAANC(MeOBn)-RMGG-Fluo) was validated as the most active fluorescein-dabcyl labeled sequence ($k_{cat}/K_M = 9160\ M^{-1}s^{-1}$). The substrate is 4 times more active than the most selective sequence from literature and selectivity was increased by a factor of 20 when compared to the most active sequence published so far, resulting in a combination between high activity and a reduced activity ratio of MMP-14/MMP-11 of a factor of 2.

Taking into account structural and electrostatic properties of

MMP-11 enzyme pockets, design of a FRET substrate for MMP-11 with the following amino acids might further increase activity as well as selectivity, due to optimized occupation of subsites P3-P3' (Table 4.0.2).

Entry	P3	P2	P1	P2'	P3'
1	A	G	Q	F	N
2	F	D	E	W	A
3	V	E	D	Y	W
4	L	R	Y	I	P

Table 4.0.2: Proposed sequence for activity and selectivity optimization

Furthermore, SM P 124 was hardly cleaved by MMP-1 and MMP-7, due to the shallow S1' specificity binding pocket of these enzymes. Stromelysins 1 and 2 (MMP-3 and MMP-10) cleave FRET substrate SM P 124 just as well as MMP-11 (stromelysin 3).

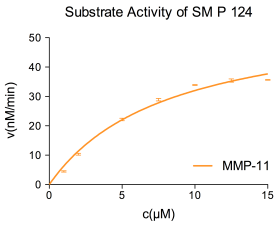

Name	Sequence	k_{cat}/K_M [$M^{-1}s^{-1}$]	K_M [μM]	k_{cat} [s^{-1}]	Selective against	Comparison to MMP-14
SM P 124	Ac-GRRRK(Dabcyl) GGAANC(MeOBn)-RMGG-Fluo	9160	8.23 ± 1.08	0.0778 ± 0.0047	MMP-1 MMP-7	0.5

Figure 4.0.3: Most active FRET substrate SM P 124 for MMP-11

Moreover, SM P 124 was tested in cellular assays with MMP-11 overexpressing cell lines MIA PaCa-2 and MCF-7, as well as with negative control cell line Jurkat. MMP-11 expression of cell lines was validated via Western Blot (Figure 4.0.4).

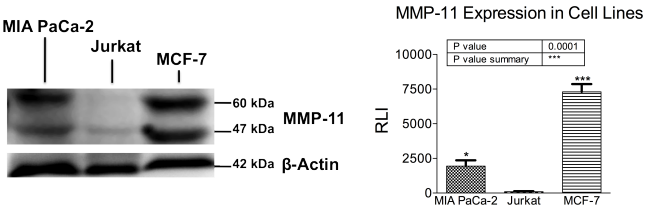

(a) Western blot of cell lysates (b) MMP-11 expression quantification

Figure 4.0.4: Western blot of cell lysates

Substrate cleavage was observed with MIA PaCa-2 and MCF-7, whereas no fluorescence increase was monitored with negative control Jurkat. Confocal laser scanning microscopy (CLSM) images confirmed substrate cleavage of SM P 124 (Figure 4.0.5a), whereas negative control substrate SM P 123 (Ac-GRRRK(dabcyl)-GYAENG-Fluo) that was not cleaved with MMP-11 was only slightly cleaved resulting in some background fluorescence (Figure 4.0.5b). However, cellular cleavage images consolidate SM P 124 as an *in vitro* imaging tool for MMP-11.

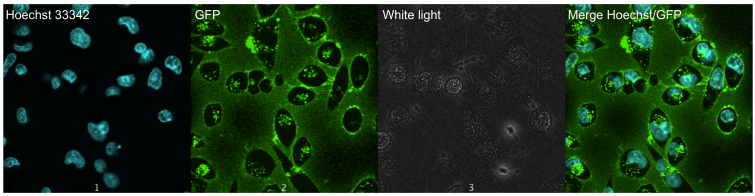

(a) SM P 124 30 min after addition to MIA PaCa-2 cells

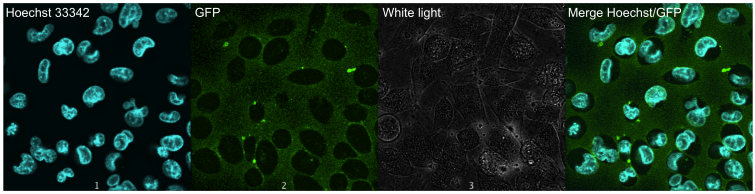

(b) SM P 123 (neg control) 30 min after addition to MIA PaCa-2 cells

Figure 4.0.5: MIA PaCa-2 cells with FRET substrate SM P 124 and negative control SM P 123

Because peptidic substrates lack bioavailability due to imidiate degradation *in vivo*, SM P 124 was coupled to a N-(2-hydroxypropyl)methacrylamide (HPMA) copolymer via native chemical ligation (Figure 4.0.6).

CLSM images confirm internalization of copolymer-substrate tracers. Administration to transgenic tumor mice resulted in a high fluorescent signal of the pancreas, whereas control mice lacked signal evolution measured 12 hours after retrobulbar injection (Figure 4.0.7).

Figure 4.0.6: Native chemical ligation enables substrate coupling to polymeric support

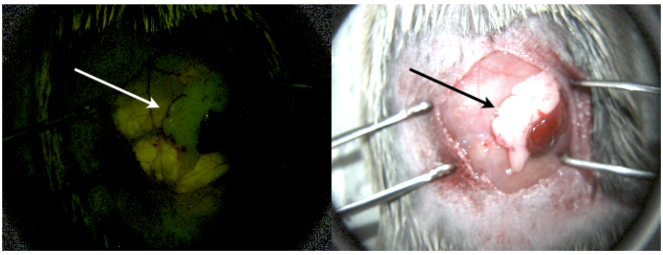

(a) Transgenic mouse with KK258

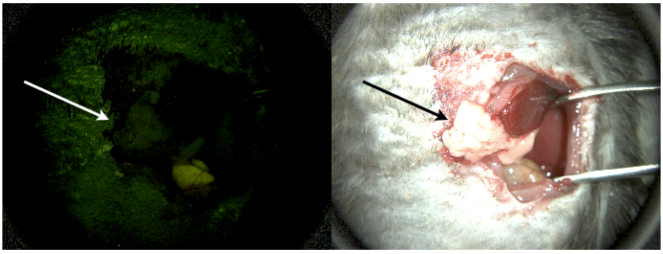

(b) Control mouse with KK258

Figure 4.0.7: Administration of 3 nmol KK258 14 h prior to measurement

In order to develop non-invasive imaging probes, substrates were engineered to fit near infrared (NIR) labels (Figure 4.0.8). The pHPMA conjugates substrates with NIR label were successfully evaluated in cellular assays and resulted in CLSM images that stated high internalization of conjugates bearing an additional RRR motif for solubility.

All NIRF-labeled copolymer-substrate conjugates were tested with MIA PaCa-2 xenografts that exhibited a fluorescent tumor *in vivo* 48 h after tail vein injection. False color images show the increasing signal from 24 h to 48 h especially for tracers KK249 and SM P 117 with very distinct and intensive signals (Figure

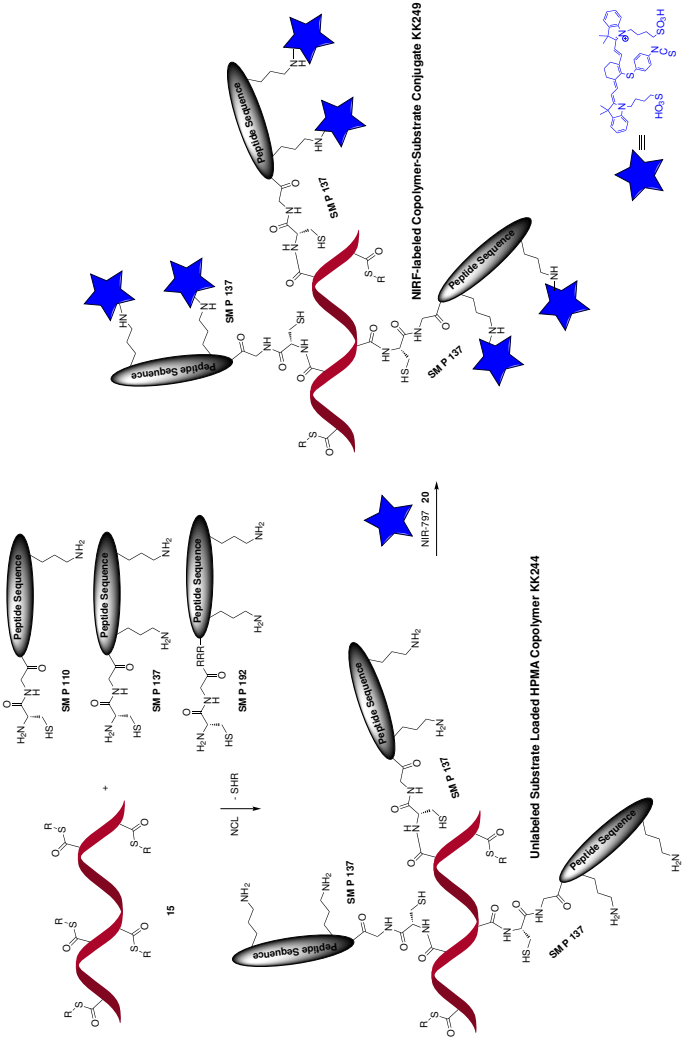

Figure 4.0.8: Synthesis scheme for copolymer-supported NIR labeled substrate

4.0.9). Optimization of the copolymer size and PDI might further increase accumulation in the tumor and could decrease the amount of unspecific cleavage *in vivo*.
Additionally, imaging with transgenic mice tested with NIRF-labeled conjugates will be further pursued to investigate imaging of precancerous lesions. Moreover, refined substrate sequences with higher activity and selectivity for MMP-11 might also further increase the signal-to-noise ratio *in vivo*.

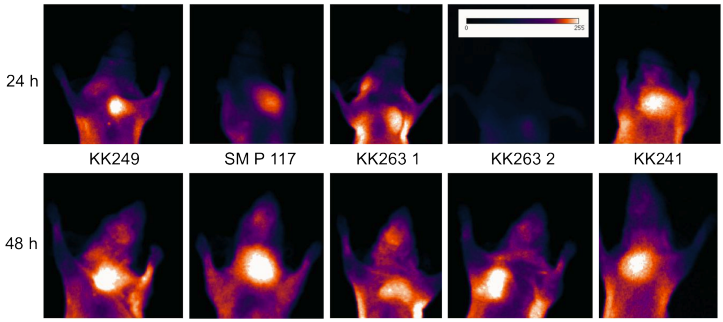

Figure 4.0.9: False color images of xenografts recorded 24 h and 48 h after tail vein injection

Furthermore, probes were refined for hyperpolarized xenon imaging to detect spatially resolved activity of MMP-11 for the early detection of pancreatic cancer, employing MRI via hp ^{129}Xe Hyper-CEST imaging (Figure 4.0.10).

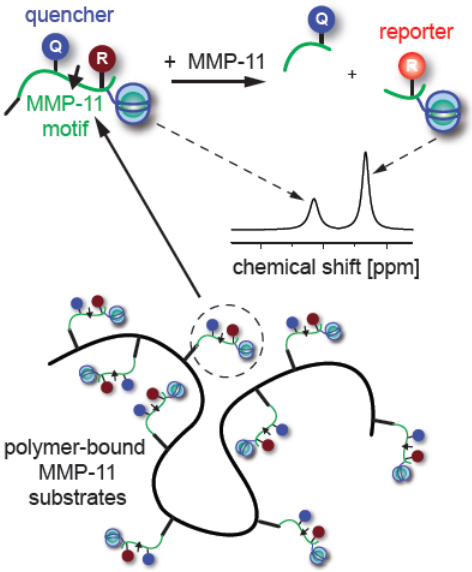

Figure 4.0.10: Copolymer-conjugated FRET substrate for hyperpolarized ^{129}Xe Imaging of MMP-11

In summary, fluorescently quenched FRET imaging probes were designed, synthesized and successfully evaluated *in vitro* and *in vivo*. This is the first time that MMP-11 activity was made visible *in vitro* and *in vivo,* and the results show the high potential of these probes as early detection tools for pancreatic cancer.

5 Experimental Part

5.1 General Materials and Instruments

Chemicals and Solvents Solvents were purchased from Sigma Aldrich, Fisher Scientific, J.T. Baker, Acros Organics, VWR or Fluka in p.a. quality. Anhydrous solvents, puriss. absolute grade, over molecular sieve, $H_2O \leq 0.005$ %, were purchased from Sigma Aldrich. LC-MS grade methanol and acetonitrile were purchased from Fluka CHROMSOLV® at analytical grade $\geq$ 99.9% p.a. and from VWR PROLABO® Grade 1, respectively. Formic acid for LC-MS was 98-100 % p.a. grade from Merck. HPLC solvents (acetonitrile and methanol) at HPLC gradient grade were also purchased from VWR PROLABO® Grade 1. Trifluoroacetic acid for preparative HPLC was 99 % extra pure grade from Acros Organics. HPLC-water was obtained from a Millipore Milli-Q® Biocel A10 purification system. Deuterated solvents for NMR were purchased by Deutero GmbH (Kastellaun). All other chemicals, reagents and resins were purchased from Sigma-Aldrich, Acros Organics, Merck, Novabiochem, EMP Biotech GmbH, ABCR or ChemPep Inc. and were used without further purification.

Thin Layer Chromatography (TLC) TLC was done on silica gel 60 F254 on coated aluminum sheets. UV light with 254 nm wavelength was used to visualize the compounds.

Liquid Chromatography – Mass Spectroscopy (LC/MS) LC/MS analysis was performed on an Agilent 1100 Series Liquid Chromatography Station equipped with a diode-array detector (DAD) and a Single Quadrupole Mass Spectrometer with electrospray ionization (ESI). The following eluent LC/MS grade solvents were used. A: water + 0.1 % formic acid, B: methanol + 0.1% formic acid or C: acetonitrile + 0.1 % formic acid. A flushing run was performed to change from eluent B to C. (method) Employing a switching valve allowed the use of 6 different columns whereas the ones used are named as follows: S3: C18 endcapped, 100 Å pore size, 3 µm particle size, 2 x 30 mm column gradient method: 5 to 99 % B/C in 3.5 min, then 2 min isocratic 99 % B/C, flow 1.2 mL·min-1 S5: C18 endcapped, 110 Å pore size, 5 µm particle size, 4 x 250 mm column (Macherey-Nagel, Nucleodur®) gradient method: 5 to 99 % B/C in 22 min, then 3 min isocratic 99 % B/C, flow 0.8 mL·min-1 S2: ZORBAX® SB-C18, 3.5 µM, 4.6 x30 mm rapid resolution column (Agilent Technologies) gradient method: 5 to 99 % B/C in 3.5 min, then 2 min isocratic 99 % B/C, flow 1.2 mL·min-1 or 5 to 99 % B/C in 10 min, then 2 min isocratic 99 % B/C, flow 0.8 mL·min-1. The m/z range 100-2000 was scanned in positive and negative mode with a voltage of 3000 V and a fragmentation of 70 V. Selected ion monitoring (SIM) was used on a second channel for selective mass detection. Chromatograms were recorded and evaluated at 254 ±4 nm, 500 ±4 nm or 750 ±4 nm. The resulting data

was analyzed with the Agilent LC/MSD ChemStation software B.01.03.

High Resolution –Mass Spectroscopy (LC/MS-TOF) LC/MS-TOF analysis was performed on an Agilent Accurate-Mass 6220 TOF LC/MS Station equipped with a diode-array detector (DAD) and a 1200 series LC. The following eluent LC/MS grade solvents were used. A: water + 0.1 % formic acid and B: acetonitrile + 0.1 % formic acid. Liquid chromatography was performed employing Agilent's ZORBAX® Eclipse column XDB-C18 Rapid Resolution HT 50 x 4.6 mm with 1.8 μm particle size.

Preparative High Performance Liquid Chromatography (HPLC)

Purifications were performed on an Agilent 1100 Series preparative HPLC with the following eluent HPLC grade solvents. A: water + 0.1 % trifluoroacetic acid and B: acetonitrile + 0.1 % trifluoroacetic acid. Solvents for preparative HPLC were degassed prior to use with ultrasound irradiation. The gradients used for purifications were determined on the analytical LC/MS (column S5, see above) and scaled-up to the preparative instrument. A volume of 2 to 9 mL was injected and a flow of 25 mL·min^{-1} was used on a C18 endcapped, 100 Å pore size, 7 µm particle size, 21 x 250 mm column (Macherey-Nagel, Nucleodur®).

ATR-IR Spectroscopy IR-spectra of resins were recorded on a Nicolet Impact 400 series FT-IR spectrometer equipped with a PIKE MIRacle^{TM}ATR-IR (KBr) detection system with a ZnSe crystal. The measurements were performed in the 400–4000 cm^{-1}

range, with a number of 32 scans, a resolution of 16, a Happ-Genzel apodization and manual background substraction.

CD Spectroscopy CD-spectra were recorded by dissolving the substrates in Millipore^{TM} water to a 10 μM solution that is measured at 24 °C in silica glass cuvettes (Helma, 0.1 x 0.1 x 4 cm^3) with a JASCO (J-720) CD spectrometer. Wavelengths were recorded at a range from 190-330 nm at 0.1 nm intervals. Calibration was performed with aqueous (+)-10-camphersulfonic acid. From obtained milli degree (mdeg) values the molar ellipticity was calculated as shown in the following equation:

$$\Theta = \frac{\Psi}{10 * c * d} \tag{5.1.1}$$

Θ= molar ellipticity [deg cm^2 dmol^{-1}], Ψ = ellipticity [mdeg], c = concentration [mol l^{-1}], d = depth of cuvette [cm]

Mean residue ellipticity was calculated by dividing the molar ellipticity by the number of residues present in the peptide sequence.

$$\Theta_r = \frac{\Theta}{n} \tag{5.1.2}$$

Θ_r= mean residue ellipticity [deg cm^2 dmol^{-1}], Θ= molar ellipticity [deg cm^2 dmol^{-1}], n= number of amino acid residues

Molecular Modeling Three-dimensional structures of proteins and protein-ligand interactions were viewed and docked with the software MOE 2006.08 from the Chemical Computing Group, Inc. The crystallographic protein structure of MMP-11 (1HV5) was downloaded from the RSCB protein data bank (PDB) www.pdb.org

Proteins and Antibodies All Matrix Metalloprotease's catalytic domains were purchased from Enzo Life Sciences (Lörrach). A unit for the protease's activity was not provided for MMP-11. The original concentrations provided in a 50 mM Tris-HCl, 5 mM $CaCl_2$, 300 mM NaCl, 20 µM $ZnCl_2$, 0.5 % Brij-35 and 30 % glycerol at pH= 7.5 buffer were diluted to a final concentration of 50 % glycerol and 1 % BSA in order to increase stability. 3 µl aliquots were stored at -80 °C. Mouse monoclonal [SL3.05] MMP-11 antibody was purchased from Abcam and was diluted 1:500 for Western Blots. Secondary goat anti-mouse HRP-labeled antibody was purchased from Dianova and wre diluted 1:10000. Monoclonal anti-β-Actin peroxidase labeled antibody was purchased from Sigma-Aldrich and was used with dilution of 1:20000. BIO-RAD Precision Plus Protein Standard Dual Color was used as a protein size reference. MMP-11 Immunoblotting Standard in SDS-PAGE buffer was purchased from Enzo Life Sciences (Lörrach).

FRET Measurements All kinetic FRET measurements were carried out on a Tecan Saphire^2 Reader for Micro Well Plates at 28 °C for 45 minutes. Excitation wavelengths: 325 nm, 483 nm, and 700 nm; emission wavelengths: 393 nm, 525 nm, and 780 nm; excitation and emission bandwidth: 10 nm, gain: was

determined corresponding to the fluorophore used; number of reads: 5; flashmode: high sensitivity; integration time: 2000 µs, lag time: 0 µs; plate definition file: COS384lvrbb.pdf; number of kinetic cycles: 200, kinetic interval: 60 s; shake duration (orbital medium): 30 s, shake duration between cycles (orbital medium): 2 s; unit: RFU

Cell Culture Dulbecco's Modified Eagle Medium (DMEM) and RPMI1640 were purchased from Gibco® Invitrogen. 10% of fetal bovine serum (FBS) (Gibco®) and 1% of a Penicillin/Streptavidin (P/S) mix also from Gibco® Invitrogen was added to all culture media. Cell lines were cultured in CORNING's T-25 to T-75 flasks and were treated under a sterile hood and incubated at 37 °C and 5 % CO_2-atmosphere. Cells were tranferred and splitted after a 5 min treatment of 0.05 % Trypsin/EDTA in DMEM. Bisbenzimide H 33342 trihydrochloride (Hoechst stain) was purchased from Sigma-Aldrich and used at a final concentration of 10 μM.

Cell Lines (in alphabetical order) Jurkat [FMP stock] Human lymphoblast T cell leukemia, suspension, Medium: RPMI1640 or DMEM

MIA PaCa-2 [Christoph Bremer's group, Universitätsklinikum Münster] Human epithelial pancreatic adenocarcinoma, adherent, single cells and loosely attached clusters, Medium: DMEM

MCF-7 [Günther Klöppel's group, Universität Kiel] Human epithelial breast adenocarcinoma, adherent, Medium: DMEM

Western Blot Blots were recorded on a Fuji LAS 4000 measuring chemiluminescence generated by addition of ECl (Enhanced Chemiluminescence) Western Blot Substrate Mix (1:1), purchased from Pierce.

Confocal Laser Scanning Microscopy (CLSM) Live-cell images were recorded on a LSM 510 laser scanning confocal microscope from Zeiss equipped with a 100 x 1.3 objective (Plan-Neofluar®, Carl Zeiss). A 200 mW argon laser (488nm) and a 15 mW He-Ne laser (633 nm) were used for excitation and a BP505-530 and LP560 bandpass filters for emission, respectively.

Fluorescence Reflectance Imaging (FRI) Immunideficient *nu/nu* mice (Charles River Laboratories International, Inc.) were anesthetized with isoflurane (2-chloro-2-(difluoromethoxy)-1,1,1-trifluoroethane and were measured with the KODAK In-Vivo Imaging System FX Pro, Carestream Health, Inc. 150 Verona Street Rochester, NY 14608 equipped with a 150-W halogen illuminator with Cy 7 bandpass excitation (700 ± 18 nm) and emission filters (780 ± 17.5 nm) and a GFP/FITC bandpass excitation (470 ± 17.5 nm) emission (535± 17.5 nm) filters. Fluorescence signals were captured for 30 s and 5 s, respectively, with a 4-million-pixel cooled charge-coupled device (CCD) camera equipped with a 10x zoom lens.

Live Microscopic Imaging Transgenic mice were imaged using a fluorescence stereomicroscope (Stemi 11, Carl Zeiss, Göttingen, Germany) equipped with a charge-coupled device camera (AxioCam-MR, Carl Zeiss Digital Camera) for 300 ms.

5.2 Solid Phase FRET Substrate Synthesis Methods and Analysis

Instruments for Solid Phase Synthesis Reactions on solid phase were performed in 2, 5, 10, or 20 mL polypropylene syringes with adapted polyethylene frits and caps, all purchased by Roland Vetter Laborbedarf OHG, Ammerbuch. For small amounts, a VXR basic IKA-Vibrax® shaker was used. A KS-15 B control shaker from Edmund Bühler GmbH was used for larger scale syntheses.

UV spectroscopy for Resin Loading Determination UV/Vis absorption spectra were measured on a JASCO V-550 UV/Vis Spectrophotometer and analyzed with the Jasco Spectra Manager software 1.54.03.
Into a 10 mL volumetric flask 2 mg of washed and dried resin is weighed and filled up with a 20% piperidine in DMF solution. Fmoc cleavage is achieved by shaking the flask occationally in 30 min at room temperature. The concentration of the cleaved Fmoc residues is then determined by UV absorption measurements, using a 20% piperidine in DMF solution as reference and using the Beer-Lambert law for the calculation. Three characteristic absorption peaks of the Fmoc group are noted at λ_1= 267 nm ($\varepsilon_{\lambda 1}$ = 17 500 L mol^{-1} cm^{-1}), λ_2 = 289 nm ($\varepsilon_{\lambda 2}$ = 5 800 L mol^{-1} cm^{-1}) and λ_3 = 301 nm ($\varepsilon_{\lambda 3}$ = 7 800 L mol^{-1} cm^{-1}). Concentrations of solutions displayed an absorption of at least 0.1 OD up to 2 OD.

Kaiser Test The Kaiser test was performed to indicate complete coupling.
To a few resin beads in a 1.5 mL Eppendorf-Cup, 50 µL of solution A and B are mixed: A: 0.2 mM aq. KCN in pyridine B : 5 % ninhydrin in ethanol The mixture is heated for 5 min at 115 °C and the resulting color was observed. The color of the solution remains yellow in absence of free primary amines, whereas it turns dark blue (Ruhemanns Purple) in presence of primary amines (all amino-acids except proline). [143, 144]

5.2.1 Preparation of FRET Substrates

All peptidic substrates were prepared according to standard Fmoc strategy solid phase synthesis. DMF, THF and DCM were used as solvents to wash the resin after each coupling and deprotection step. Kaiser Tests were performed to monitor completeness of the reaction.

Non-labeled Peptide Sequences Peptidic sequences without label for copolymer conjugation or Cryptophane-A couplings were prepared via standard Fmoc mediated solid phase synthesis based on coupling to rink amide AM resin purchased from Novabiochem. Coupling reagents used are 3 eq amino acid, 3 eq hydroxy benzotriazole (HOBt), and 3 eq diisopropylcarbodiimide (DIC). Components are predissolved in DMF to activate the amino acid and are then added to the dry resin. The suspension is allowed to shake for 3 h. Completeness of coupling is determined via Kaiser test. Positive Kaiser tests result in repetition of the performed coupling step.

AMCA-labeled Peptide Sequences 1eq of 7-Amino-4-methyl-3-coumarinylacetic acid (AMCA) is protected with 1.5 eq of Fmoc-chloride in a 1:1 water/acetone solvent mixture at 0 °C after preactivation with 10 eq of aqueous NaOH. The reaction mixture is allowed to stir overnight and the resulting precipitate is filtrated and washed with cold water, ethanol, and ether. Fmoc protected Rink amide resin is deprotected with 20 % piperidine in DMF, twice, for 10 min at RT. 3 eq of Fmoc-AMCA are activated with 3 eq of hydroxy benzotriazole (HOBt) and 3 eq of diisopropylcarbodiimide (DIC). The mixture is added to the Rink amide resin and is allowed to react for 3 h at RT. Loading efficiency is determined via Fmoc determination. The first glycine coupling is achieved by coupling of 5 eq of glycine, 5 eq of O-(7-Azabenzotriazol-1-yl)-N, N, N', N'-tetramethyluronium hexafluorophosphate (HATU) and 10 eq of 2,4,6-trimethylpyridine (collidine) with the Fmoc deprotected AMCA-resin overnight at RT, twice. Following amio acid couplings afford 3 eq of amino acid, 3 eq of HOBt, and 3 eq of DIC in DMF for 3 h at RT. Repeated Fmoc deblocking and coupling yields the AMCA-labeled peptide sequence. The quencher is introduced by coupling of 3eq of Fmoc-N-(2,4-dinitrophenyl)-L-lysine with equivalent amounts of HOBt and DIC in DMF for 3h at RT. Completed sequences are acetylated in the last step with a 1:1:1, v/v/v mixture of acetic anhydride, DIPEA, DCM for 10 min at RT.

Fluorescein-labeled Peptide Sequences The first coupling step is performed by adding the Fmoc-protected amino acid to a solution of 5 eq of O-(7-Azabenzotriazol-1-yl)-N, N, N', N'-tetramethyluronium hexafluorophosphate (HATU) and 10 eq of 2,4,6-trimethylpyridine (collidine) in DMF/DCM (1:1, v/v) to the prepared O-

(methoxyethoxymethyl)-5-aminofluorescein 2-chlorotrityl resin [105] for 3 h at room temperature, twice. Fmoc determination is performed to determine the fluorescein – glycine coupling efficiency. The Fmoc group is then removed by employing a 20 % piperidine in DMF mixture twice for 10 min to the resin. The following amino acids are coupled by adding 3 eq of Fmoc-protected amino acid, 3 eq of diisopropylcarbodiimide (DIC), 3 eq of hydroxy benzotriazole (HOBt), and 3 eq of diisopropylethylamine (DIPEA) in DMF for 3 hours. The Fmoc deblocking and coupling steps are repeated for additional amino acid couplings. The dabcyl quencher is introduced by coupling of 3 eq of N_α-Fmoc-N_ε-4-[4-(Dimethylamino)phenylazo)benzoyl]-L-lysine with 3 eq HOBt and 3 eq of DIC in DMF overnight at RT. The syringe is changed afterwards. Unprotected peptides are N-acetylated in the last step by adding 1 ml of acetic anhydride/DCM/DIPEA (1:1:1, v/v/v) for 10 minutes at RT. Sequences bearing a N-terminal cysteine for Native Chemical Ligation to polymeric support were not acetylated before cleavage.

Fluorescein-labeled Peptide Sequences for Cryptophane-A Labeling The prepared O-(methoxyethoxymethyl)-5-aminofluorescein 2-chlorotrityl resin is coupled with 5 eq of glycine, 5 eq of O-(7-Azabenzotriazol-1-yl)-N, N, N', N'-tetramethyluronium hexafluorophosphate (HATU) and 10 eq of 2,4,6-trimethylpyridine (Collidine) in DMF/DCM (1:1, v/v) for 3 h at RT. The Fmoc group is deprotected with 20 % piperidine in DMF twice for 10 min at RT. Fmoc-Dap(ivDde)-OH (3 eq) is coupled with 3 eq of HOBt and DIC in DMF overnight at RT. The Fmoc group is again deblocked and the peptide sequence is constructed using standard coupling conditions employing HOBT/DIC coupling

cocktails. For N-terminal cysteine sequences Boc-Cys(Trt)-OH was used as the N-terminal amino acid generating an unprotected cysteine upon cleavage. After sequence construction completion, ivDde is deprotected with 10 % hydrazine in DMF four times for 10 min at RT. A positive Kaiser test allows the next coupling step of 5 eq Fmoc-Dap(ivDde)-OH with 5 eq HATU and 10 eq Collidine in DMF overnight at RT. The Fmoc group is deblocked with 50 % DBU and 10 % peiperidine in DCM for 30 min at RT and is confirmed with a positive Kaiser test. Coupling of 5 eq Fmoc-PEG3-OH, 5 eq HATU, and 10 eq Collidine in DMF overnight at RT was followed by Fmoc deblocking with 50 % DBU and 10 % piperidine in DMF for 30 min at RT. The amine group was acetylated with acetic anhydride and DIPEA in DCM (1:1:1) for 10 min at RT followed by ivDde deprotection with 10 % hydrazine four times for 10 min at RT until the Kaiser test shows a positive outcome. The complete sequence is cleaved off the resin, employing the cleavage cocktail for C(MeOBn) containing sequences.

Cleavage Conditions and Isolation Processes The following cleavage cocktails are applied to the resin for 24 h. DCM/TFA/ H_2O/Phenol/EDT/TIS (50:40:5:1:2.5:2.5, v/v/v/m/v/v) is applied to substrates containing MeOBn protected cysteine whereas DCM/
TFA/H_2O/Phenol/EDT/TIS (5:90:2:1:1:1, v/v/v/m/v/v) is used for leucine containing peptides. Substrates are precipitated in ether and are washed thrice with ether/MeCN (95:5) followed by drying in vacuo and isolation by HPLC. All sequences are purified via RP-HPLC employing a 15 % to 40 % MeCN gradient in water over 40 min on a C-18 ec column.

Sequence Validation All Sequences were validated by LC-MS and LC-MS/TOF. Mass deviations are < 0.5 while all purities are $> 95\%$.

5.2.2 Labeling Syntheses

NIR-797 Labeling Unlabeled peptide containing free amine functional groups (1 eq) is dissolved in dry DMF and 5eq of diisopropylethylamine (DIPEA) are added. NIR-797 isothiocyanate (5 eq) predissolved in dry DMF is added dropwise. The reaction mixture is monitored via LC/MS and DMF is evaporated as soon as the starting material is consumed. Work-up processes depend on the nature of the probe to be labeled. Polymeric probes were isolated via dialysis (membrane with 3 kDa cut-off) and gel-filtration whereas peptides were precipitated with ether and isolated via HPLC with a gradient run ranging from 5 % acetonitrile to 50 % in 40 min.

Cryptophane-A Labeling Cryptophane-A (2 eq) is dissolved in dry THF and 4 eq of 2,4,6-trimethylpyridine (Collidine) are added. 2 eq of O-(7-Azabenzotriazol-1-yl)-N, N, N', N'-tetramethyluronium hexafluorophosphate (HATU) are dissolved in dry DMF and are added to the Cryptophane-A/Collidine mixture. The cocktail is stirred for 15 min and is then added dropwise to the amine-reactive peptide (1eq) dissolved in dry DMF. The reaction mixture is stirred overnight, the solvent is evaporated and the residue is dissolved in THF/Ether in order to isolate unreacted Cryptophane-A from the coupled peptide. The precipitate is centrifuged and washed thouroughly with THF/Ether. The peptide is then analyzed by LC/MS and is coupled for a second

time with Cryptophane-A if starting material is detected in the precipitate. The resulting product is then isolated via RP-HPLC with a gradient ranging from 10 % acetonitrile to 40 % in 60 min.

5.2.3 Absorption and Emission Spectra

All substrates are measured on a Tecan Saphire^2 Reader on a Corning #3544 microplate in Tris-HCl buffer at pH= 7.5 at a final concentration of 5 μM. Spectra are recorded at an excitation wavelength of 483 ± 10 nm and an emission wavelength of 525 ± 10 nm. NIR-labeled substrates are measured at an excitation wavelength of 700 ± 10 nm and an emission wavelength of 780 ± 10 nm. AMCA substrates were measured at 325 ± 10 nm ecxitation wavelength and 393 ± 10 nm emission wavelength. Substrate solutions are shaken prior to measurement in an orbital manner for 30 s.

5.2.4 FRET Substrate Sequences and Analysis

Entry	Sequences	Name	Crude Yield (%)	Yield (%)	Mass (calcd)	Mass found LC/MS-TOF
1	Ac-C(MeOBn)RMGG-Fluo (Fluorescence Standard)	SM CM	71	32	1046.331	1046.2200
2	Ac-C(MeOBn)VRGG-Fluo (Fluorescence Standard)	SOM 9	48	48	981.3691	981.3755
3	Ac-C(MeOBn)WARGG-Fluo (Fluorescence Standard)	SOM 11	53	5	1140.4171	1140.2990
4	Ac-LR(M=O)GG-Fluo (Fluorescence Standard)	SOM 5	30	30	919.3585	919.35831 (ox. +16)
5	Ac-LVRGG-Fluo (Fluorescence Standard)	SOM 8	48	48	436.6933	436.7001 (M+2)/2
6	Ac-LWARGG-Fluo (Fluorescence Standard)	SOM 10	39	8	1030.4345	1030.4185
7	Mca-PLG-NH_2 (Fluorescence Standard)	SM P 96	96	89	500.2271	500.2356

Entry	Sequences	Name	Crude Yield (%)	Yield (%)	Mass (calcd)	Mass found LC/MS-TOF
8	Ac-C(MeOBn)VRGG-K(CryptoA)GG-NH_2 (Fluorescence Standard)	SOM 44	97	17	1813.7949	1813.6864
9	Ac-C(MeOBn)RMDap-(Dap(PEG_3-Ac)-(CryptoA)G-Fluo (Fluorescence Standard)	SM P 196	9	7	2279.8672	2279.8722
10	Ac-C(MeOBn)-RMGGK(Cy7)-NH_2 (Fluorescence Standard)	SM P 190	51	28	1784.7001	1784.4994
11	Ac-C(MeOBn)-RMGG-AMCA (Fluorescence Standard)	SM P 93	97	86	841.3251	841.3345
12	Ac-GRRRK(Dnp-)GGAANC(MeOBn)-RMGG-AMCA	SM P 155	40	24	639.9545	640.2970 (M+3)/3
13	Ac-GRRRK(Dabcyl)-GGAANC(MeOBn)-RMGG-Fluo	SM P 124	21	6	2289.0341	2289.0422
14	Ac-GRRRK(Dabcyl)-GNAA-C(MeOBn)-R(M=O)G-Fluo	SM P 126	20	4	736.3246	736.6677 (M+3)/3 (ox. +16)

Entry	Sequences	Name	Crude Yield (%)	Yield (%)	Mass (calcd)	Mass found LC/MS-TOF
15	Ac-GRRRK(Dabcyl)-GGNAAC(MeOBn)-RMGG-Fluo	SM P 125	23	8	1145.5171	1144.8886 (M+2)/2
16	Ac-GRRRK(Dabcyl)-GGYAEC(MeOBn)-RMGG-Fluo	SM P 127	31	7	2396.0600	2396.0668
17	Ac-GRRRK(Dabcyl)-GGAANC(MeOBn)-VRGG-Fluo	SM P 148	25	3	1129.0347	1129.0343 (M+2)/2
18	Ac-GRRRK(Dabcyl)-GGYAEC(MeOBn)-VRGG-Fluo	SM P 151	40	6	2364.0880	2364.0724
19	Ac-GRRRK(Dabcyl)-GGAANLRMGG-Fluo	SM P 130	34	6	2179.0515	2179.0421
20	Ac-GRRRK(Dabcyl)-GGYAELRMGG-Fluo	SM P 133	50	17	2286.0774	2286.0633
21	Ac-GRRRK(Dabcyl)-GGAANLVRGG-Fluo	SM P 154	41	7	1074.0434	1074.0430 (M+2)/2
22	Ac-GRRRK(Dabcyl)-GGYAELVRGG-Fluo	SM P 157	33	8	2254.1053	2254.0928
23	Ac-GRRRK(Dabcyl)-GGPLAC(MeOBn)-WARGG-Fluo	SM P 166	65	11	1220.5871	1220.5859 (M+2)/2
24	Ac-GRRRK(Dabcyl)-GGPLALWARGG-Fluo	SM P 175	42	19	1165.5958	1165.5944 (M+2)/2

Entry	Sequences	Name	Crude Yield (%)	Yield (%)	Mass (calcd)	Mass found LC/MS-TOF
25	Ac-GRRRK(Dabcyl)-GGAANC(MeOBn)-WARGG-Fluo	SM P 169	48	5	1208.0587	1208.0588 (M+2)/2
26	Ac-GRRRK(Dabcyl)-GGYAEC(MeOBn)-WARGG-Fluo	SM P 172	51	7	2522.136	2522.1140
27	Ac-GRRRK(Dabcyl)-GGAANLWARGG-Fluo	SM P 178	46	18	1153.0674	1153.0669 (M+2)/2
28	Ac-GRRRK(Dabcyl)-GGYAELWARGG-Fluo	SM P 181	39	10	2412.1533	2412.1313
29	Ac-GRRRK(Dabcyl)-GYAENG-Fluo	SM P 123	59	26	943.4222	943.9315 (M+2)/2
30	H-CGRRRK(Dabcyl)-GGAANC(MeOBn)-RMGG-Fluo	SM P 122	11	2	2350.0255	2350.5721
31	H-CGRRRK(Dabcyl)G-YAENG-Fluo	SM P 194	27	9	1946.8431	1946.7756
32	Mca-PLGLK(Dnp)-AR-NH_2 (SM Omni)	SM P 95	91	78	1134.5458	1134.5550
33	Ac-GRRRK(NH_2)-GGAANC(MeOBn)-RMGGK(NH_2)-NH_2	SM P 191	98	55	1834.9631	1834.9898
34	H-CGRRRK(NH_2)-GGAANC(MeOBn)-RMGGK(NH_2)-NH_2	SM P 192	99	51	632.9872 (M+3)/3	638.6634 (ox. +16)

Entry	Sequences	Name	Crude Yield (%)	Yield (%)	Mass (calcd)	Mass found LC/MS-TOF
35	H-CGGK(NH_2)-GGAAN-C(MeOBn)-RMGGK(NH_2)-NH_2	SM P 137	78	41	1485.6799	1485.3866
36	H-CGGAANC(MeOBn)-RMGGK(NH_2)-NH_2	SM P 110	97	88	1243.5420	1243.6778
37	Ac-GGAANC(MeOBn)-VRGGK(CryptoA)-GG-NH_2	SOM 43	12	7	2183.9550	2183.7900
38	H-CGGAANC(MeOBn)-VRGGK(CryptoA)-GG-NH_2	SOM 28	17	5	1577.6949	1577.4420 Pbf-protected
39	Ac-GRRRK(Dabcyl)-GGAANC(MeOBn)RM-Dap(Dap(PEG_3-Ac)(NH_2)G-Fluo	SM P 187	5	-	2633.2043	2633.2200
40	H-CGRRRK(Dabcyl)-GGAANC(MeOBn)RM-Dap(Dap(PEG_3-Ac)(NH_2)G-Fluo	SM P 188	12	-	2695.2107	2695.0716

Table 5.2.2: Synthesized Peptide FRET Substrates for *in vitro* Validation

5.3 *In vitro* Validation Methods and Conditions

5.3.1 Kinetic Förster Resonance Energy Transfer (FRET) Assay

Assay Setup Buffer conditions: 50 mM Tris-HCl, pH= 7.5, 150 mM NaCl, 10 mM CaCl2, 0.05 % Brij-35 [99, 145]

All assays include three replicates of each compound tested. Every compound was furthermore independantly measured thrice on different days. The median values of the three measurements are then used to describe activity values for comparison of the prepared comounds.

Enzyme titration assays are prepared by adding varying concentrations of enzyme to a fixed concentration of substrate. For this experiment a final substrate concentration of 12.5 µM of Ac-GRRRK(Dabcyl)AANC(MeOBn)RMGG-Fluo (250 µM stock, 1 µl) is assayed with 100 nM, 50 nM, 25 nM, 12.5 nM, 6.25 nM, and 3.125 nM of MMP-11 (19 µl in Tris-buffer). For MMP-14 final enzyme concentrations of 5 nM, 2.5 nM, 1.25 nM, 0.625 nM, 0.3125 nM, and 0.15625 nM are used (19 µl in Tris-buffer).

All substrates are prepared as 10 mM stock solutions in DMSO. A stock dilution series in DMSO ranging from 400 µM, 350 µM, 300 µM, 250 µM, 200 µM, 150 µM, 100 µM, 50 µM, 20 µM and 0 µM (DMSO) is prepared and used throughout the assays with a further dilution factor of 20. 1 µl of each stock concentration in three replicates is pipetted into each well of the microplate and 19 µl of enzyme in Tris-buffer at its final concentration (12.5 nM for MMP-11 and 0.625 nM for MMP-14, as has been determined by

enzyme titration) are added to start the kinetic measurements. The same setup is prepared with buffer without the enzyme to function as a control and as a fluorescence background measurement. 100 % hydrolysis is measured in respect to the concentration of the fluorescence standard Ac-C(MeOBn)RMGG-Fluo. Concentrations used correspond to 2 - 10 % (1-1000 nM, final assay concentration) of hydrolized substrate to avoid quenching effects in the solution. The wells are also sealed with PCR-foil Ultra Clear RT-PCR in order to prevent evaporation of assay mixture from wells during kinetic measurements.

Förster Resonance Energy Transfer (FRET) measurements are carried out on low-volume roundbottom black non-binding surface 384-multiple well microplates from Corning (#3676) with a Saphire^2 Reader from Tecan at 28 °C. Enzyme dilutions are prepared using the following buffer system: 50 mM Tris-HCl, pH= 7.5, 150 mM NaCl, 10 mM CaCl2, 0.05 % Brij-35. Sequences labeled with the 7-amino-4-methyl-3-coumarinylacetic acid (AMCA) - Nε-(2,4-dinitrophenyl)-L-lysine (K(Dnp)) FRET-pair are measured at an excitation wavelength of $\lambda = 323 \pm 10$ nm and an emission wavelength of $\lambda = 395 \pm 10$ nm. Sequences containing the 5-aminofluorescein (Fluo) - Nε-(4-[4-(dimethylamino)-phenylazo)benzoyl-L-lysine (K(Dabcyl)) FRET-pair are measured at an excitation wavelength of $\lambda = 483 \pm 10$ nm and an emission wavelength of $\lambda = 525 \pm 10$ nm. 3 reads per well and an integration time of 2000 µs is employed. The plates are centrifuged with an Eppendorf® Centrifuge 5810 R at 1000 tr $\times$ min^{-1} for 1 min to eliminate bubbles before measurements. All plates are covered with a PCR-foil Ultra Clear RT-PCR (G060/UC-RT) from G. Kisker GbR to avoid evaporation during 60 min of kinetic measurements at 28 °C. Additionally, the plates are shaken for

10 s before measurements and for 2 s in between measurements in an orbital manner. The results are analyzed by plotting and fitting the curves with Prism 5.0 (Graph Pad Software, Inc., San Diego, CA) to the Michaelis-Menten equation:

$$Y = \upsilon_{max} \frac{X}{K_M + X} \tag{5.3.1}$$

Y= substrate velocity in nM/min; X= substrate concentration in μM

5.3.2 Cellular Kinetic FRET Assay

Culture Conditions Frozen cells (10 % DMSO in cell medium, 1.5 x10^6 cells) are thawed rapidly in a 37 °C warm water bath and are transferred to a T-75 flask containing 20 ml of DMEM culture medium containing 10% FBS and 1% P/S. At near confluence, the culture medium is removed. The cells are washed carefully with PBS and fresh medium is added. Cells are incubated at 37 °C in a 5 % CO_2 atmosphere. Cell culture medium is exchanged as described above every two days, whereas cells are splitted 1:5 every four days (at 80 % confluence).

Assay Setup Corning's black cell-bind multi well plate #3683 is applied to measure 4000 cells per well seeded two days prior to measurement in 50 μl DMEM (10 % FBS, 1 % P/S). 50 μl of varying concentrations of MMP-11 active substrate and negative control substrate dissolved in medium are added two days after seeding. Final concentrations used are: 5 μM, 2,5 μM, 1 μM, 0,5 μM, 0,1 μM, 0 μM (DMSO). Plates were covered with PCR-foil

Ultra Clear RT-PCR to avoid evaporation. Fluorescence is measured over 80 min with a Tecan Saphire^2 reader with excitation wavelength of 485 ± 10 nm and an emission wavelength of 525 ± 10 nm. The results were analyzed by plotting the curves with Prism 5.0 (Graph Pad Software, Inc., San Diego, CA).

Copolymer-substrate conjugates were measured over a time range of 10 hours at 37 °C. Plates (#3683) seeded with 4000 cells per well in 50 μl two days prior to measurement were covered with PCR-foil Ultra Clear RT-PCR to avoid evaporation and to ensure sterility at the time of measurement. 10 μM of substrate-copolymer conjugates dissolved in 50 μl FBS-free medium were added to plated cell wells and were measured at an excitation wavelength of 485 ± 10 nm and an emission wavelength of 525 ± 10 nm for fluorescein labeled probes, while NIR labeled conjugates were monitored at 700 ± 10 nm excitation wavelength and 780 ± 10 nm emission wavelength. The results were analyzed by plotting the curves with Prism 5.0 (Graph Pad Software, Inc., San Diego, CA).

5.3.3 Western Blots

1 x 10^6 cells are lysed in 10 μl of NP-40 lysis buffer. (Table 5.3.2 on page 232) Cell lysate concentrations are determined of the supernatant after centrifugation with a Bradford Assay (see next paragraph). The samples are diluted with Laemmli buffer 5:1 and are loaded to the gel. (Gel purchased from Criterion, gradient gel 4-20 %) As a protein marker BIO-RADs Precision Plus Protein Standard Dual Color is loaded. 200 V for 75 min yield separated proteins on the gel. The proteins are transfered to a PVSF membrane via electroblotting at 200 mA for 1 h. The

membrane is activated with MeOH prior to use. It is then blocked overnight at 4 °C in blocking buffer (5 % BSA in TBS-T buffer) and afterwards washed 3 x 10 min with TBS-T. The first antibody specific for MMP-11 (abcam, monoclonal mouse anti-MMP-11) is applied in blocking buffer at a 1:500 concentration for 1.5 h at RT followed by 3 x 10 min of washing with TBS-T. Goat anti-mouse HRP-labeled antibody from dianova was used as secondary antibody in a 1:10000 dilution in blocking buffer for 2h at RT. The membrane is again washed with TBS-T 3 times for 10 min. ECL western blotting substrate was purchased from Pierce, is mixed 1:1 and applied to the membrane for 1.5 min at RT. Western Blots were recorded on a Fuji LSA 4000 Luminescent Analyzer.

The membrane is stripped from the applied antibodies 4 times 10 min with stripping buffer. It is then washed 3 times for 10 min with TBS-T and a HRP labeled antibody specific to a housekeeping protein is applied for 2h at RT at a 1:20000 dilution. (Sigma-Aldrich, anti-β-Actin peroxidase antibody) The membrane is again washed 3 x 10 min before the ECL western blotting substrate mix is applied. Lanes from β-Actin were quantified with gel analyzing software. (ImageJ, National Institutes of Health, USA) MMP-11 lanes were normalized against β-Actin quantities and were evaluated graphically. (GraphPad Prism 5.0) Additionally, a t-test was performed to test for significance of the displayed results. Statistical significance as represented in the graphs is described in table 5.3.1. Buffer recipies are listed in table 5.3.2 on page 232.

P value	Significance	Marked with
< 0.001	extremely significant	***
0.001 to 0.01	very significant	**
0.01 to 0.05	significant	*
>0.05	not significant	ns

Table 5.3.1: Statistical significance determination

Pancreatic tumor and normal tissue samples are sliced with a cryometer at -20 °C into 5 μm slices. The tissues are lysed in RIPA buffer and protein concentrations of the supernatant are determined with a Bradford Assay. The samples are denatured and loaded to a SDS-gel. The process explained above is repeated.

Bradford Assay Protein concentrations of cell lysates or tissue lysates are determined by protein staining with coomassie-brillant-blue G-250. The forming protein-dye complex has an absorption maximum at 595 nm at which the samples are then measured. A standard slope of known concentration of coomassie dye complexed with BSA is used to convert optical density (OD) values to concentration of protein.

5.3.4 Confocal Laser Scanning Microscopy

30000 cells in 2ml DMEM medium (10 % FBS, 1 % P/S) are seeded on a 30 mm round glass slide of 1 mm height (Thermo-Scientific) that were precoated with poly-L-lysine (Sigma Aldrich) one day prior to use in a 6 well Corning #3331 plate. Cellular nuclei were stained with 10 μM Hoechst dye 33342 30 min before

Entry	Lysis buffer	Leammli Sample Buffer 5x	Migration buffer	Blotting buffer	TBS-T	Stripping buffer
1	50 mM Tris-HCl, pH= 7.5	10 % SDS	25 mM Tris-HCl pH= 8.3	25 mM Tris-HCl pH= 8.3	50 mM Tris-HCl pH= 7.5	6 M Guanidin-HCl
2	140 mM LiCl	25 % β-mercapto-ethanol	190 mM glycine	190 mM glycine	150 mM NaCl	20 mM Tris-HCl, pH= 7.5
3	2 mM EDTA, pH= 8	50 % glycerol	0.1 % SDS	20 % MeOH	0.1 % Tween-20	0.1 M β-mercapto-ethanol
4	0.5 % NP-40	0.01 % bro-mophenol blue (w/v)				0.2 % NP-40
5	1:7 dilution (from 2 tablets in 3 ml stock solution) of Complete Mini EDTA-free Protease Inhibitor Cocktail Tablets	0.3125 M Tris-HCl pH= 6.8				

Table 5.3.2: Buffers used for western blotting

live-cell imaging. The glass slides are adjusted to a carrier and 500 μl DPBS are applied. Additional 500 μl of 10 μM imaging substrate in DPBS are added and a time series is recorded every 5 min for 30 min. Additionally, polymer-conjugated probes are preincubated in FCS-free medium for 5.5 h or 8.5 h, are then transferred to the carrier and measured after addition of 500 μl DPBS.

5.4 *In vivo* Validation Methods and Conditions

5.4.1 Fluorescence Reflectance Imaging (FRI)

MIA PaCa-2 xenografts are generated by subcutanious injection of 10 x 10^6 cells suspensed in 100 μl PBS to the breast of immunideficient *nu/nu* mice (Charles River). After two weeks at a tumor size of 2-5 mm, 2 nmol of imaging substrate are injected via the tail vein to isoflurane anesthetized mice. The animals are imaged with the KODAK In-Vivo Imaging System FX Pro with laser and filter set for Cy7 or GFP/FITC directly after injection, after 30 min, 1 h, 3 h, 6 h, 24 h, and 48 h. All animal experiments were approved by the local authorities and were in compliance with institutional guidelines.

5.4.2 Transgenic Mouse Imaging

Transgenic mice with a TGF-α/p53^{+}/$^{-}$ gene mutation [136] for pancreatic tumor generation are imaged using a fluorescence stereomicroscope equipped with a charge-coupled device camera

AxioCam MR Plus (Stemi 11, Carl Zeiss, Göttingen, Germany). Mice are anesthetized with medetomidine, midazolam and fentanyl (MMF), followed by retrobulbar administration of imaging substrate 14 h prior to fluorescence microscopy imaging. A small left abdominal incision is made and the spleen and pancreas are displayed by a gentle pull followed by fluorescence measurements. Animals are sacrificed afterwards. All animal experiments were approved by the local authorities and were in compliance with institutional guidelines.

6 Appendix

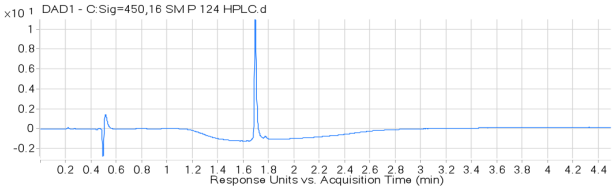

(a) SM P 124

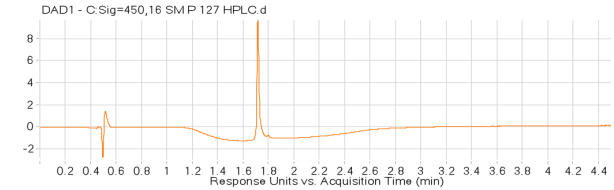

(b) SM P 127

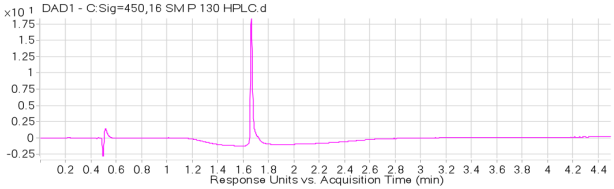

(c) SM P 130

Figure 6.0.1: FRET substrate library chromatograms SM P 124, SM P 127, and SM P 130

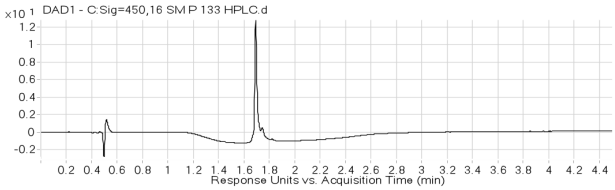

(a) SM P 133

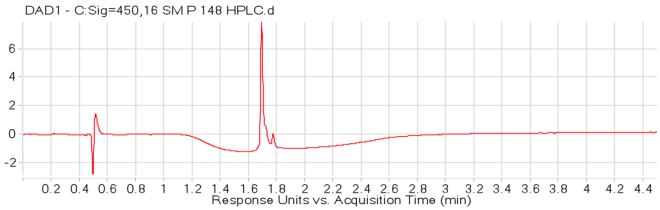

(b) SM P 148

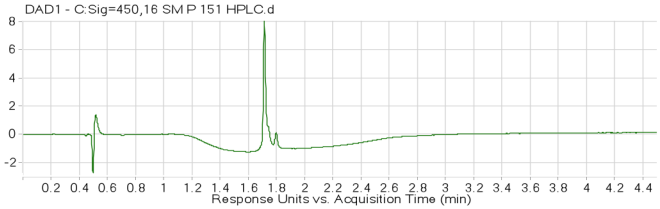

(c) SM P 151

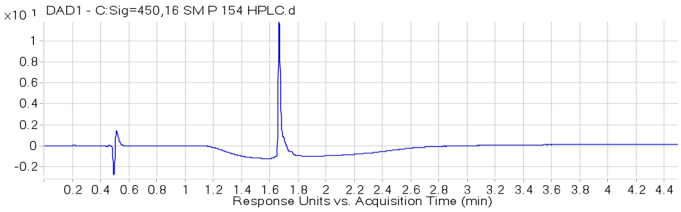

(d) SM P 154

Figure 6.0.2: FRET substrate library chromatograms SM P 133, SM P 148, SM P 151, and SM P 154

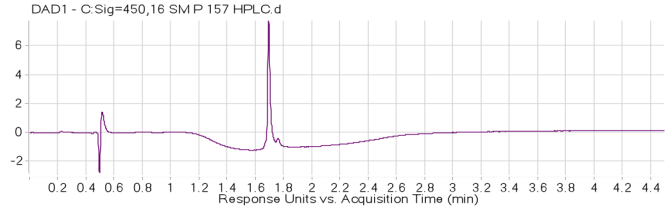

(a) SM P 157

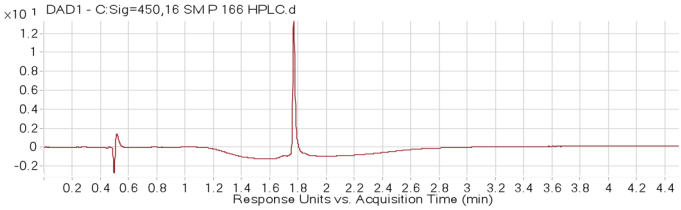

(b) SM P 166

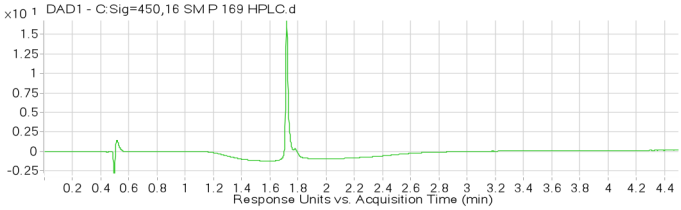

(c) SM P 169

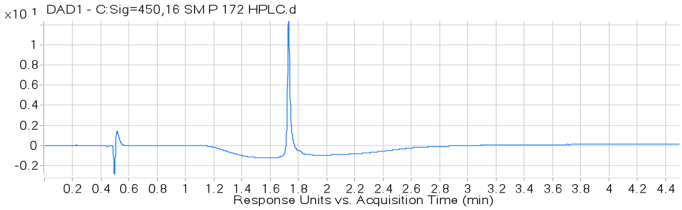

(d) SM P 172

Figure 6.0.3: FRET substrate library chromatograms SM P 157, SM P 166, SM P 169, and SM P 172

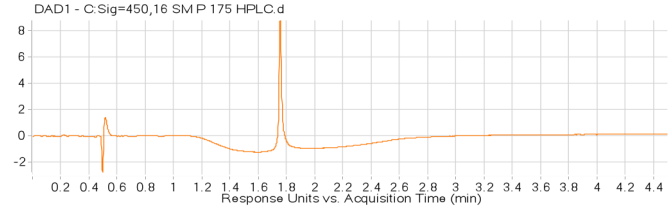

(a) SM P 175

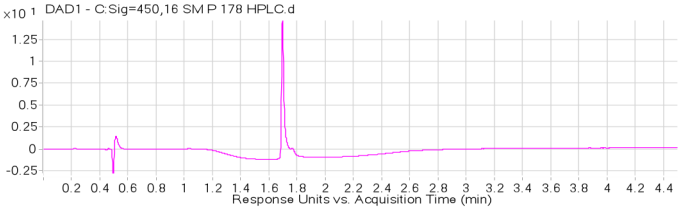

(b) SM P 178

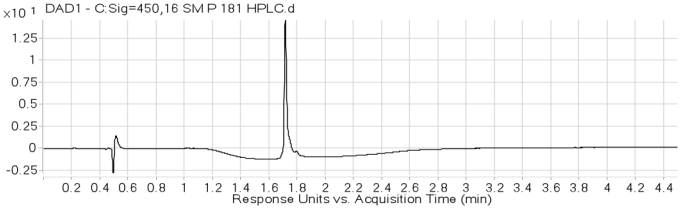

(c) SM P 181

Figure 6.0.4: FRET substrate library chromatograms SM P 175, SM P 178, and SM P 181

LC/MS-TOF assay validation:

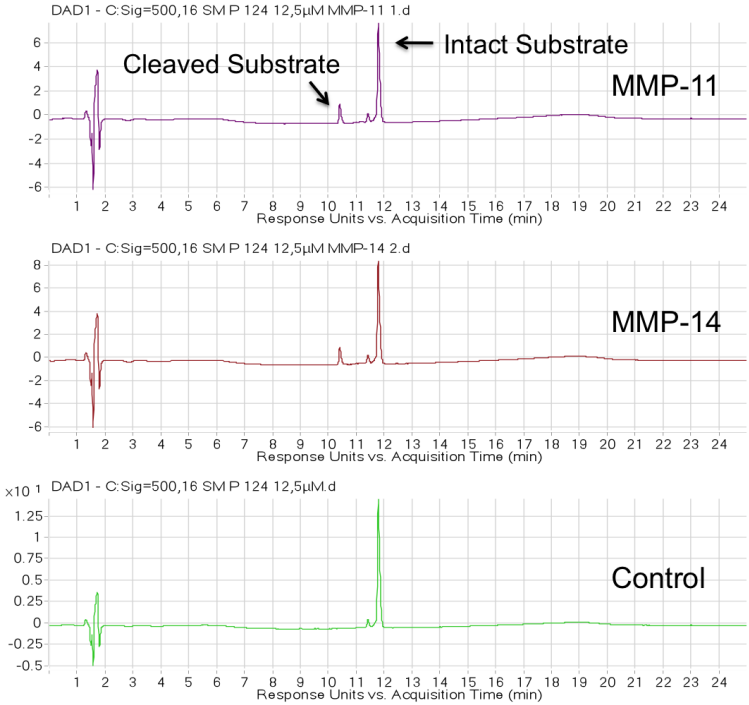

Figure 6.0.5: LC/MS-TOF assay validation of SM P 124; small peak at 11.5 min represents single oxidized intact substrate, whereas evolving peak at 10.4 min displays cleaved substrate

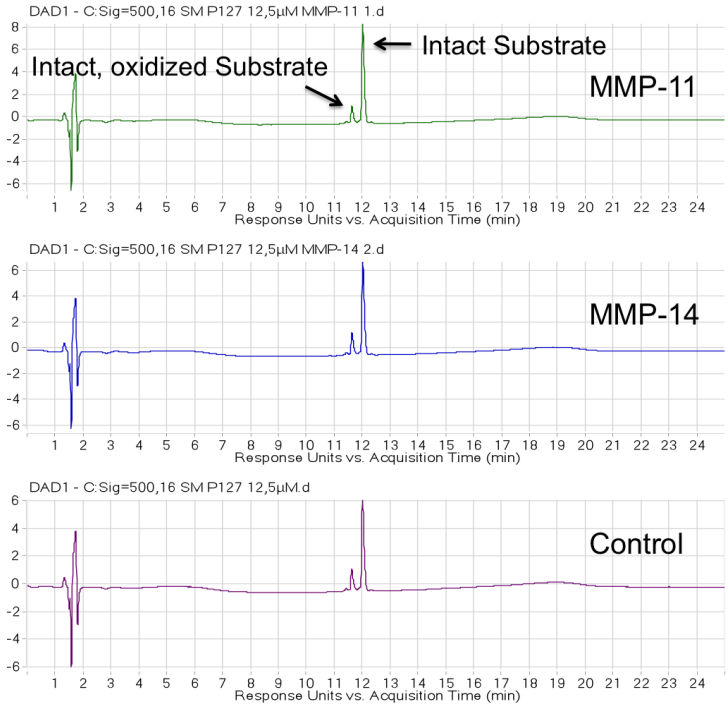

Figure 6.0.6: LC/MS-TOF assay validation of SM P 127; small peak at 11.6 min represents single oxidized intact substrate, no cleavage product was observed

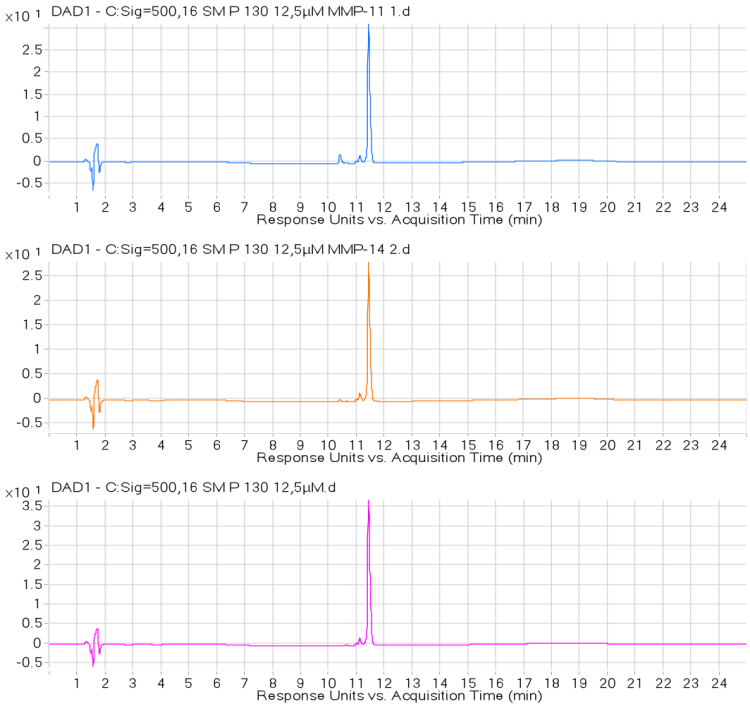

Figure 6.0.7: LC/MS-TOF assay validation of SM P 130; small peak at 11.2 min represents single oxidized intact substrate, whereas evolving peak at 10.4 min displays cleaved substrate

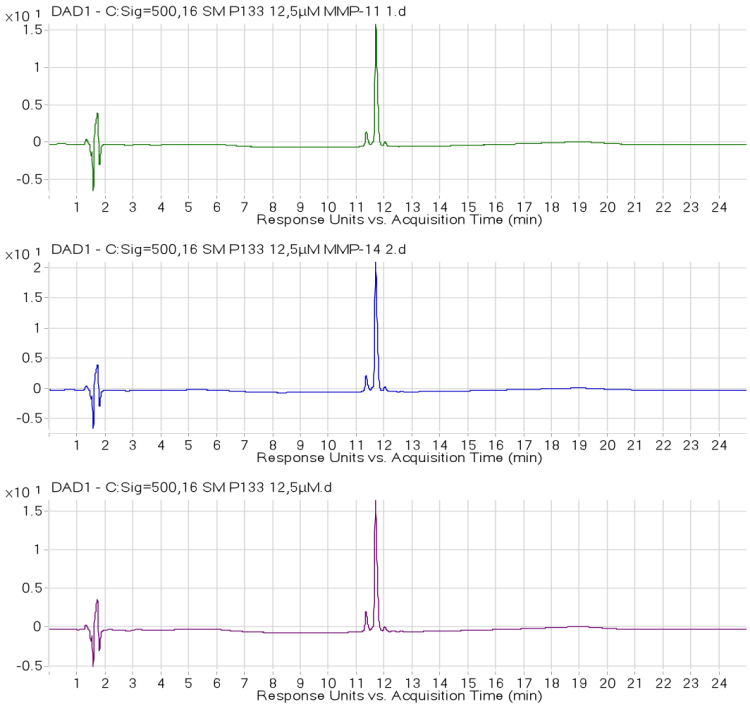

Figure 6.0.8: LC/MS-TOF assay validation of SM P 133; small peak at 11.5 min represents single oxidized intact substrate, no substrate cleavage was observed

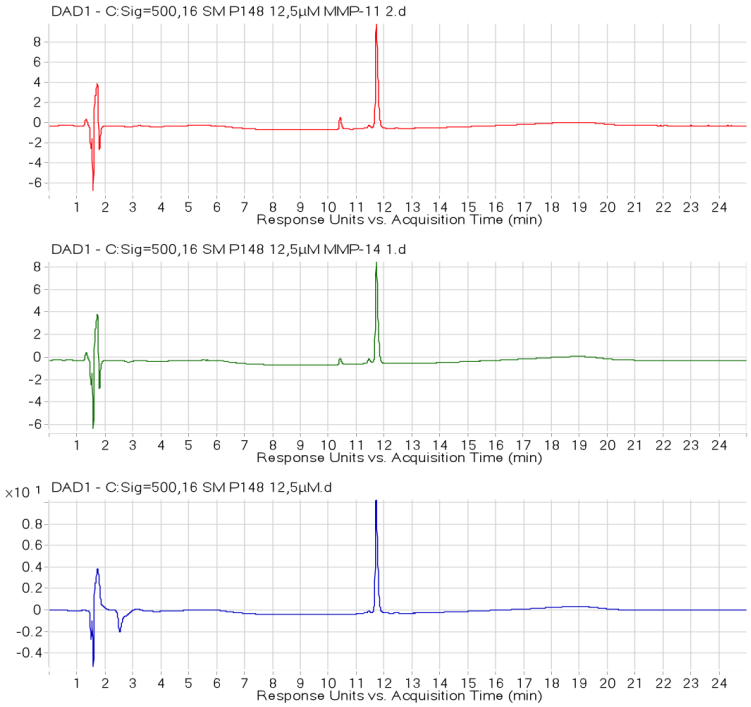

Figure 6.0.9: LC/MS-TOF assay validation of SM P 148; evolving peak at 10.4 min displays cleaved substrate

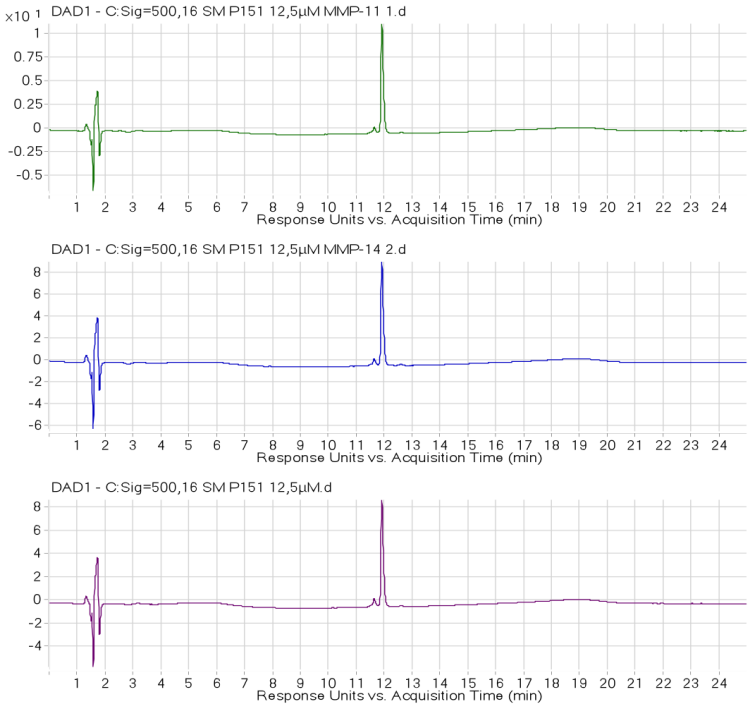

Figure 6.0.10: LC/MS-TOF assay validation of SM P 151; small peak at 11.7 min represents single oxidized intact substrate, no substrate cleavage was observed

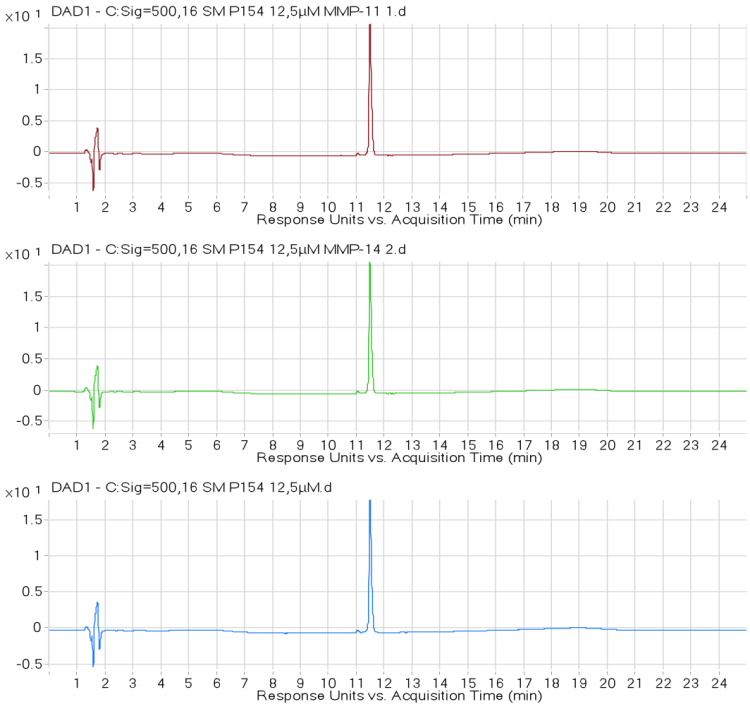

Figure 6.0.11: LC/MS-TOF assay validation of SM P 154; no substrate cleavage was observed

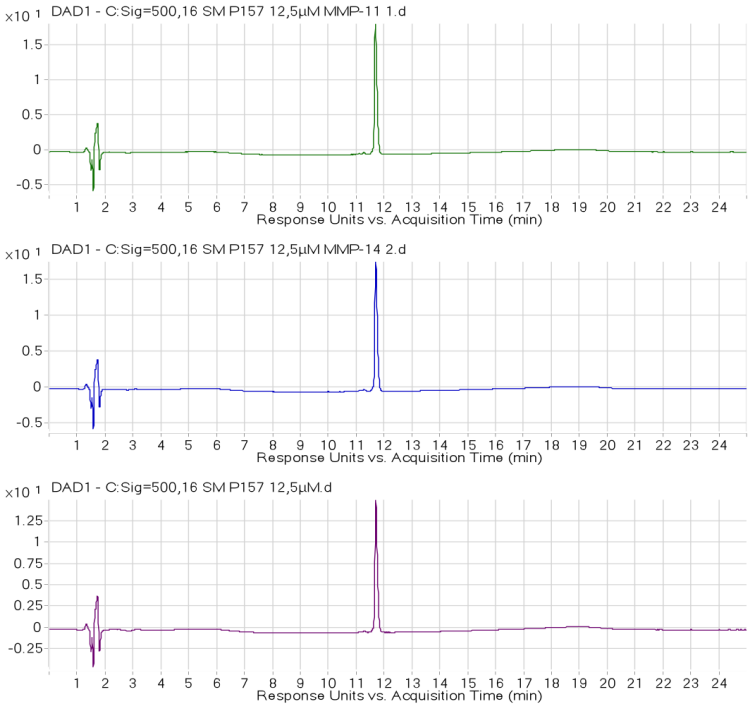

Figure 6.0.12: LC/MS-TOF assay validation of SM P 157; small peak at 11.5 min represents single oxidized intact substrate, no substrate cleavage was observed

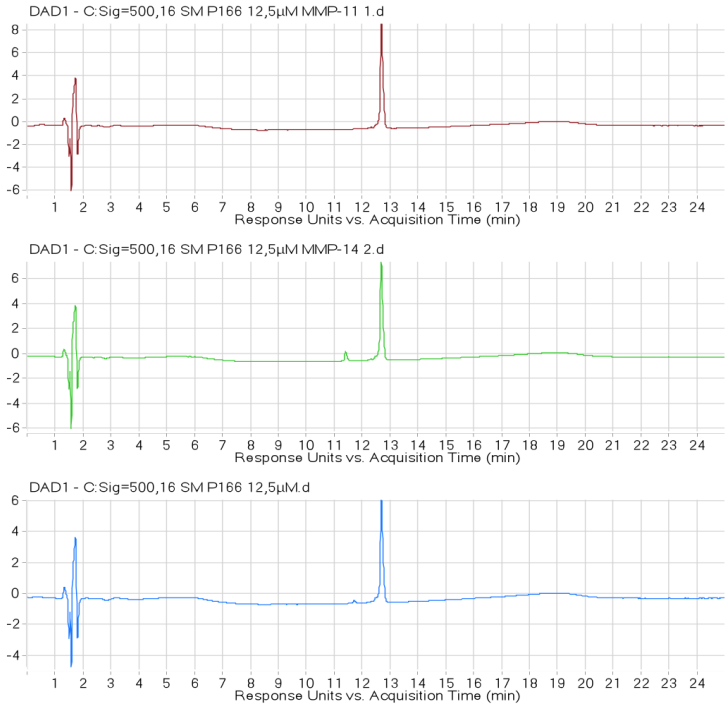

Figure 6.0.13: LC/MS-TOF assay validation of SM P 166; substrate cleavage was only observed with MMP-14

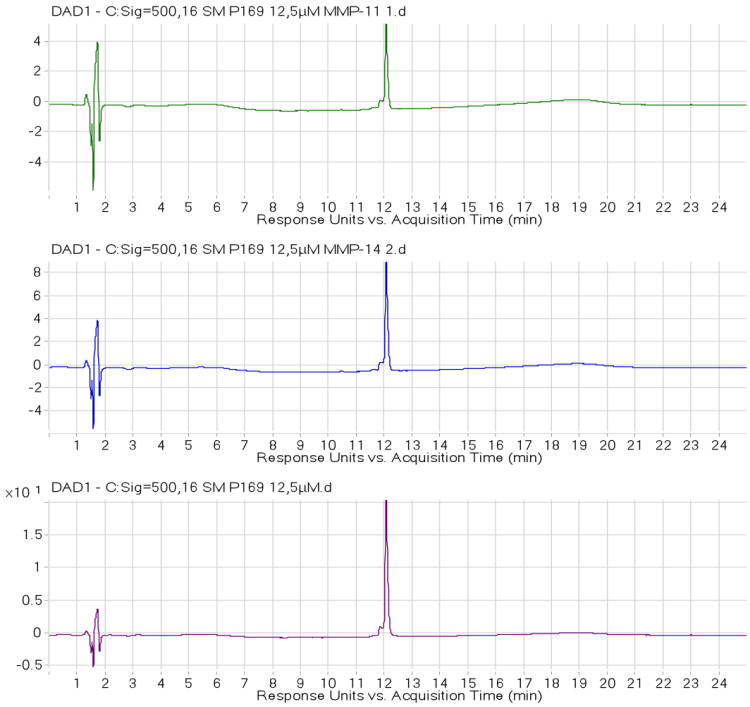

Figure 6.0.14: LC/MS-TOF assay validation of SM P 169; small peak at 11.8 min represents single oxidized substrate, no substrate cleavage was observed

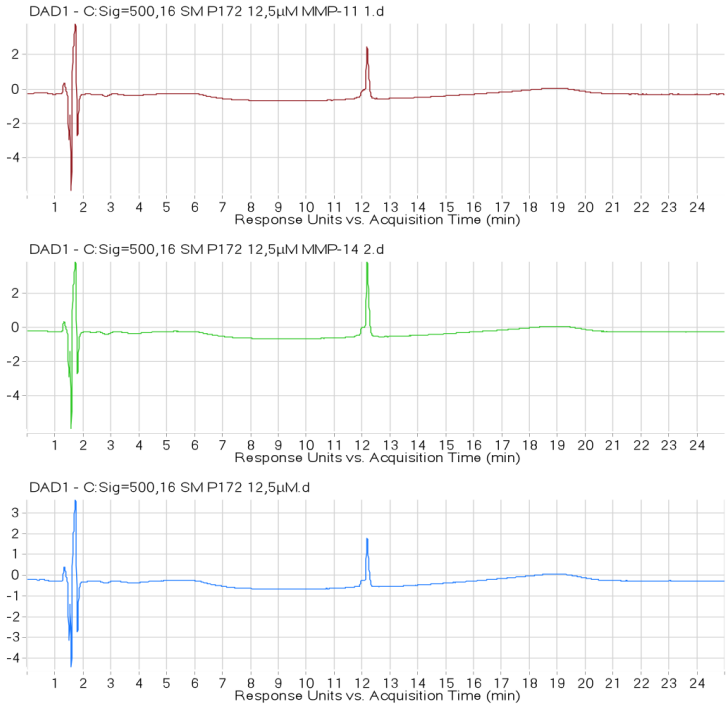

Figure 6.0.15: LC/MS-TOF assay validation of SM P 172; small peak at 12 min represents single oxidized substrate, no substrate cleavage was observed

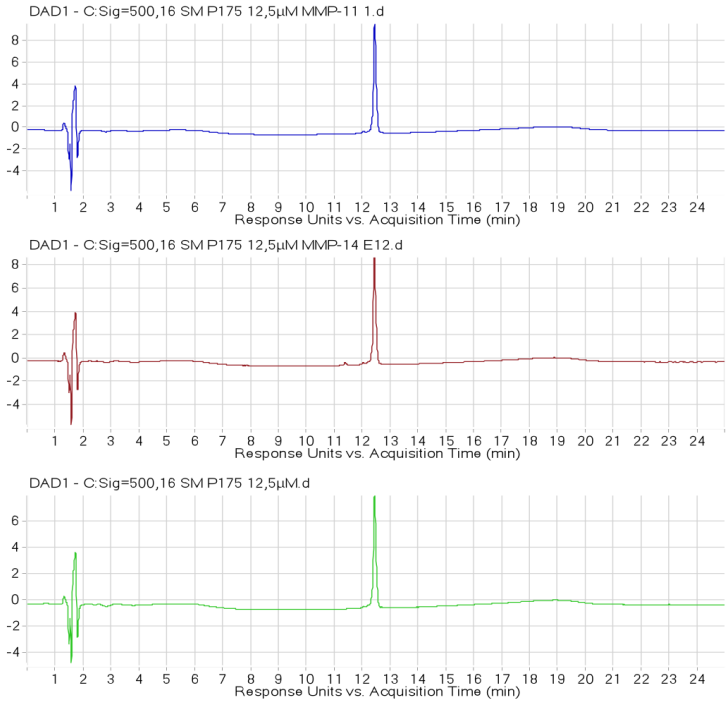

Figure 6.0.16: LC/MS-TOF assay validation of SM P 175; small peak at 11.5 min represents small amounts of cleaved substrate with MMP-14, no substrate cleavage was observed with MMP-11

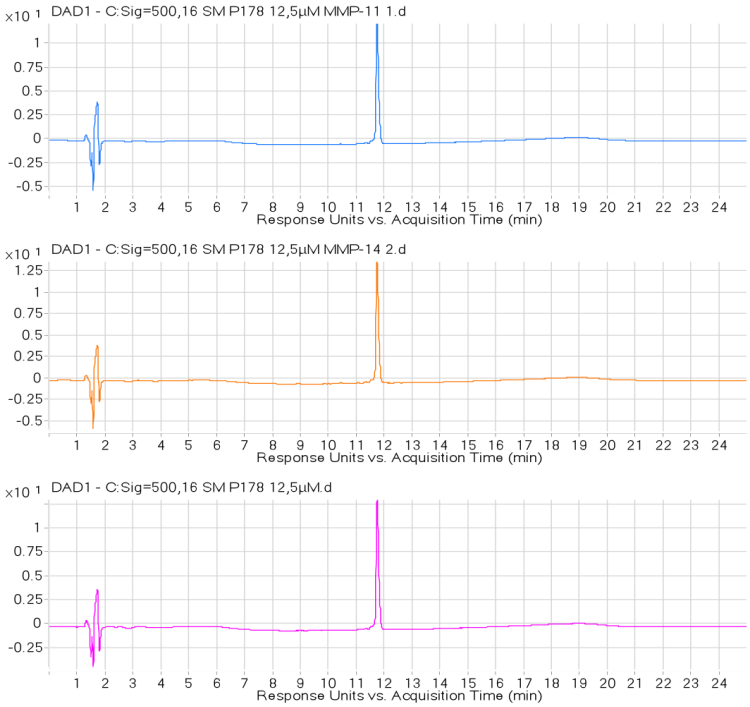

Figure 6.0.17: LC/MS-TOF assay validation of SM P 178; no substrate cleavage was observed

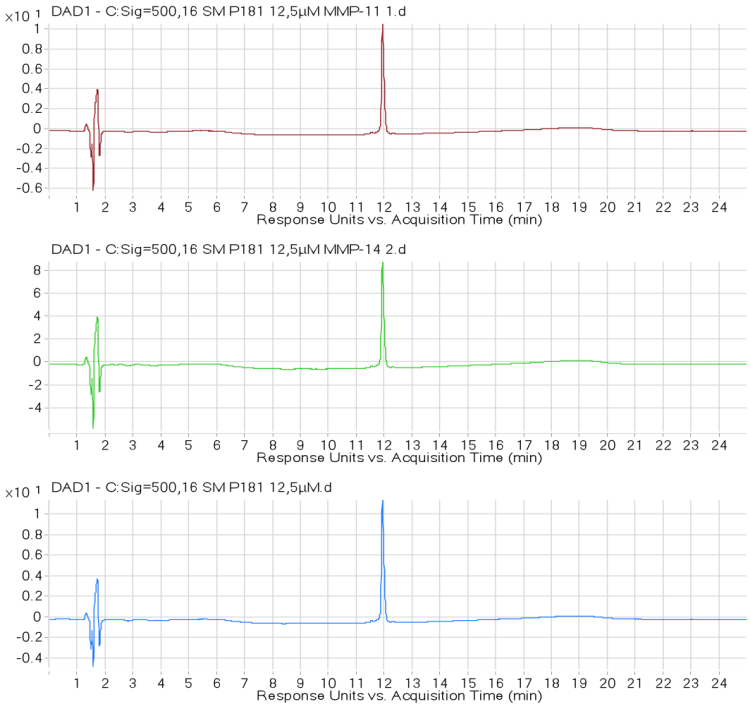

Figure 6.0.18: LC/MS-TOF assay validation of SM P 181; no substrate cleavage was observed

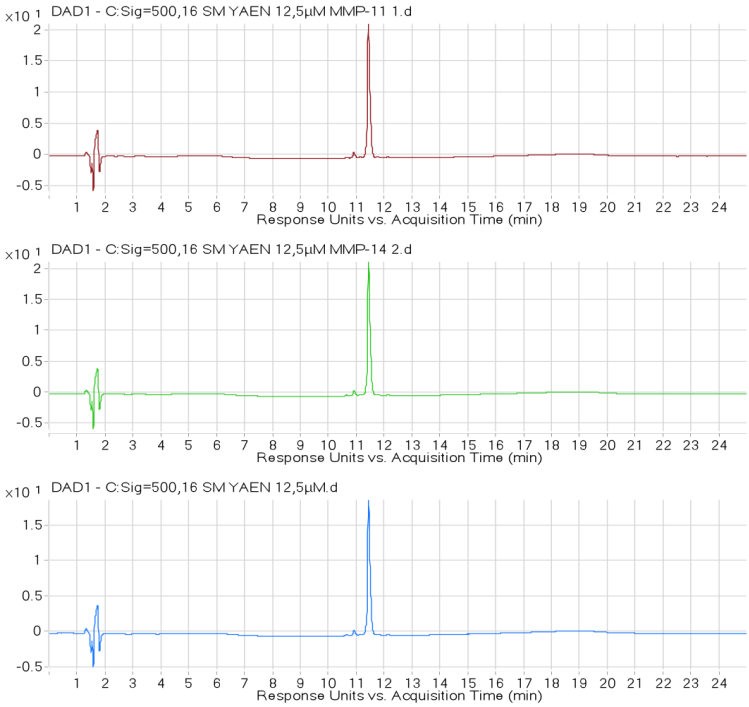

Figure 6.0.19: LC/MS-TOF assay validation of negative control substrate SM P 123; as anticipated, no substrate cleavage was observed

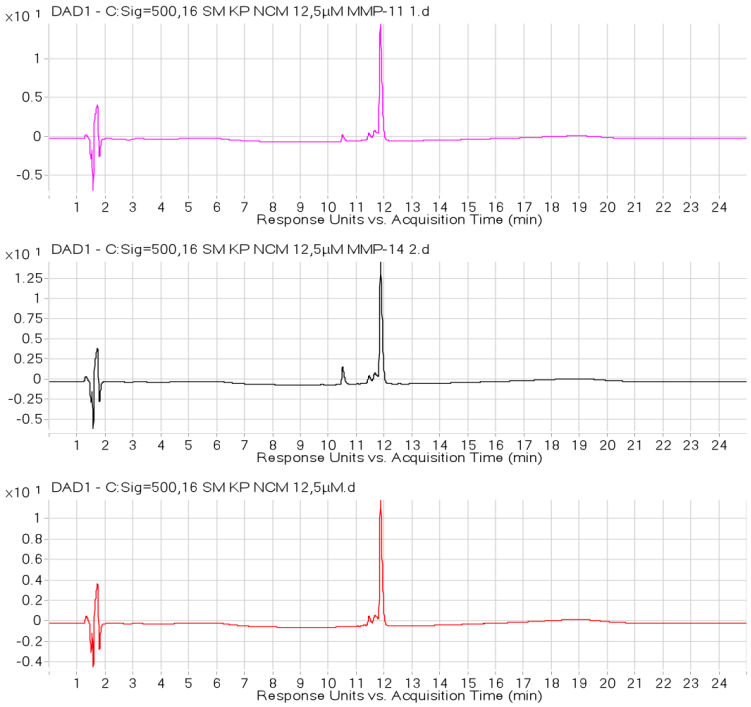

Figure 6.0.20: LC/MS-TOF assay validation of SM P 125; small peaks at 11.5 min and 11.8 min represent single and double oxidized intact substrate, whereas cleaved substrate can be observed at 10.5 min

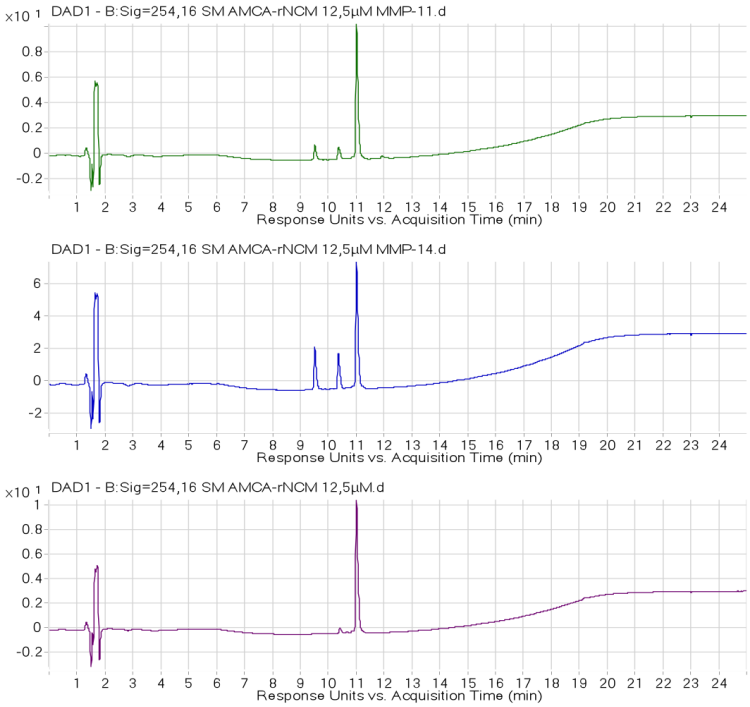

Figure 6.0.21: LC/MS-TOF assay validation of AMCA labeled SM P 155; as anticipated, substrate cleavage was observed with both metalloproteases, at 254 nm both cleavage products are visible, namely peaks at 9.6 min and 10.4 min

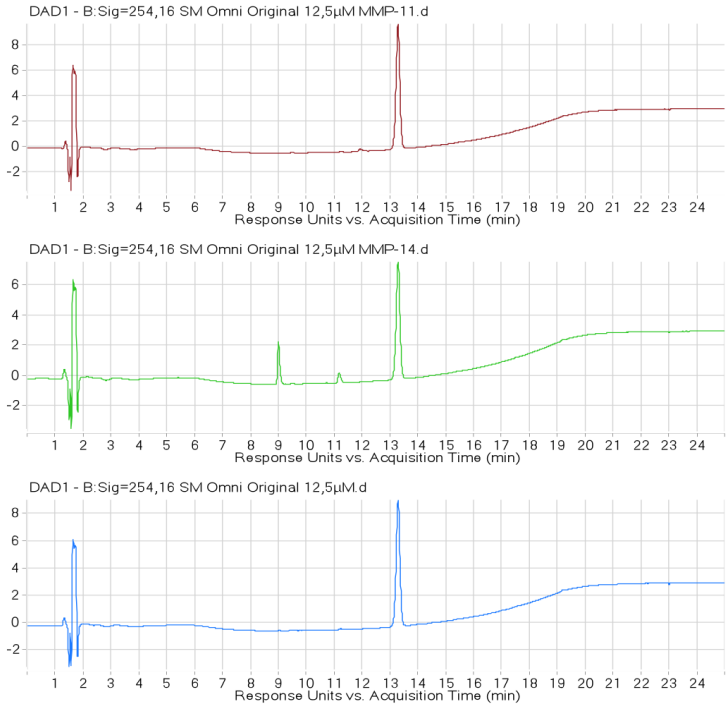

Figure 6.0.22: LC/MS-TOF assay validation of commercially available OmniMMP^{TM} substrate; substrate cleavage was observed only with MMP-14, substrate cleavage peaks can be observed at 9.0 min and at 11.2 min

In vivo Clearance Study of Healthy Control Mice:

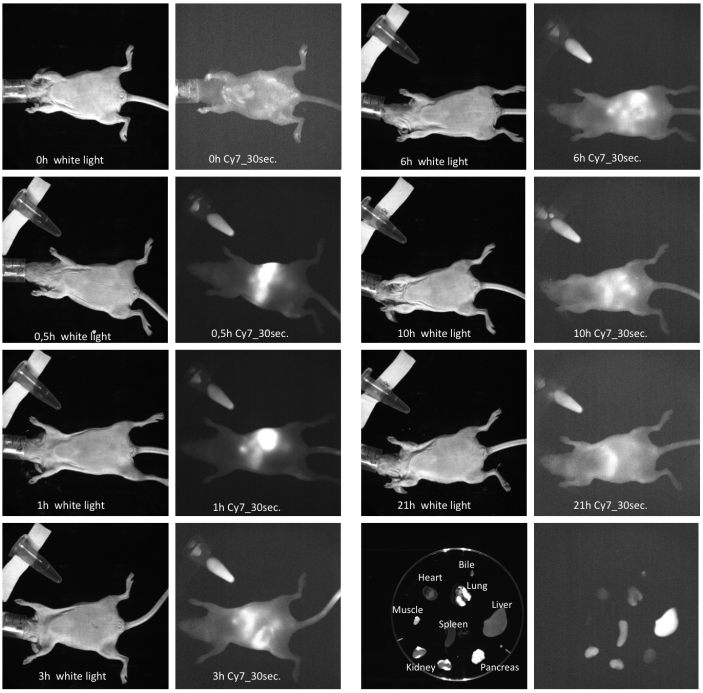

Figure 6.0.23: *In vivo* clearance study for SM P 117; Biodistribution *ex vivo* 21 h after tail vein injection

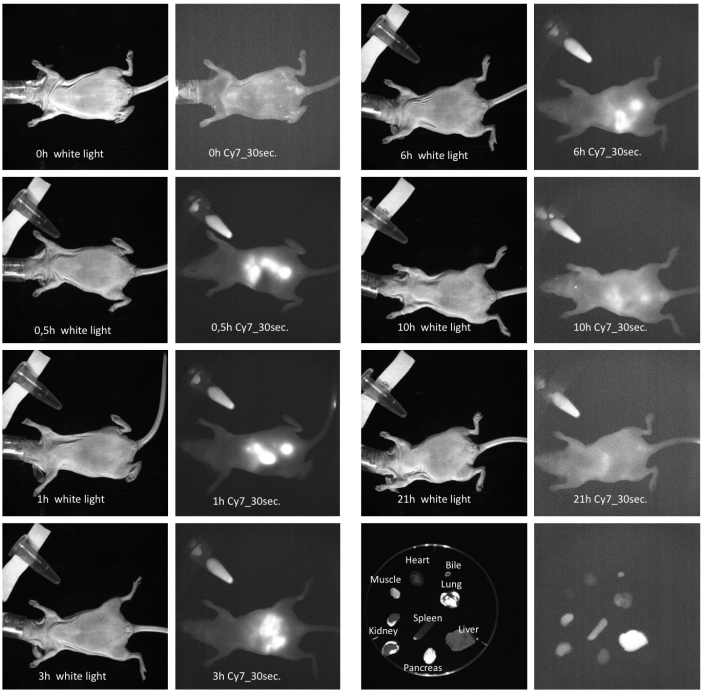

Figure 6.0.24: *In vivo* clearance study for non-targeted KK241; Biodistribution *ex vivo* 21 h after tail vein injection

List of Figures

1.1.1 Cancer deaths in percentages in the U.S. for men and women in 2009 [2] 20
1.1.2 Distribution of cancer cases throughout race and stage in comparison to five-year survival rate throughout race and stage [2] 21
1.1.3 Anatomy of the pancreas[26] 24
1.1.4 From non-invasive lesions to infiltrating adenocarcinoma in three stages [25] 26
1.1.5 Immunohistochemistry of normal pancreatic duct in comparison to PanINs and adenocarcinoma [26] 26
1.1.6 Members of the matrix metalloprotease family [41] 29
1.1.7 Common MMP domains a) Structural representation of full length MMP [48] b) Schematic domain representation of varying MMPs [50] 31
1.1.8 Crystal structure overlay of different MMPs [58] 32
1.1.9 Active site cleft of MMP-12 [49] 34
1.1.10 MMP-mediated substrate cleavage [52] 35
1.1.11 Crystal structure of S1' subsite of MMP-11 [66] 37
1.1.12 Superposition of MMP-11 crystal structure with that of MMP-8 [64] 38
1.1.13 MMP-11 expression in cancer vs normal tissue [67] 40

1.1.14Immunohistochemical staining of MMP-11 in tumorous (1+2) and normal (3+4) tissue [67] . . . 40
1.1.15 MMP-11 mRNA levels determined by RT-PCR [67] 42
1.2.1 Advantages and disadvantages of varying imaging modalities [74] 45
1.2.2 Absorption of differing fluorophores like GFP (green fluorescing protein) and cyanine dyes, adapted from [77] 46
1.2.3 Spectral overlap of FRET donor emission with acceptor excitation [80] 47
1.2.4 Requirements for efficient Förster resonance energy transfer [80] 49
1.2.5 Hyperpolarization of ^{129}Xe a) Optical pumping for the preparation of hyperpolarized ^{129}Xe [91] b) Spin flip by optical pumping [90] 52
1.2.6 ^{129}Xe chemical shift diversity in differing media [91] 53
1.2.7 Selective saturation of hp ^{129}Xe [96] 54
1.2.8 Hyper-CEST demonstration of signal enhancment for *in vivo* imaging applications [96] 55

3.1.1 Target Identification Pathway 59
3.1.2 Patient's PDAC and normal tissue tested in Western Blot 60
3.2.1 Unusual amino acids tested in P1' position of MMP-11 substrates [99] 64
3.2.2 Comparison of unusual amino acid containing sequences for MMP-11 [99] 66
3.2.3 Substrate sequence comparison of Phage Display sequences [64] 67

3.2.4 Preparation of C-terminally labeled fluorescein resin for solid phase peptide synthesis as described by Uryga-Polowy et al.[105] 72
3.2.5 Cleavage condition comparison with and without addition of 1% phenol 76
3.2.6 Linker approach for C-terminal fluorescein labeling 79
3.2.7 General substrate structure 80
3.2.8 C-terminal AMCA labeling on Rink amide AM resin 81
3.2.9 Absorption intensities at 485 nm 83
3.2.10 Emission intensities of prepared FRET-substrates 85
3.2.11 Example CD spectra of secondary structures types and random coil (denatured) [109] 86
3.2.12 CD specroscopy of prepared FRET substrate library; Upper row: overlay of all FRET substrates, lower row: sets of sequences with comparable FRET efficiencies 87
3.2.13 left: white light image showing intact FRET substrate (orange fluid, upper vessel) and cleaved substrate as fluorescent standard (yellow fluid, vessel below) 88
3.2.14 Emission of Dnp quenched AMCA substrates and cleaved fluorescence standards 89
3.3.1 Michaelis-Menten kinetics of substrate conversion [111] 91
3.3.2 Fluorescence (Product formed) increase over time with linear inital rate period [112] 92
3.3.3 Activity determination of MMP-11 and MMP-14 94
3.3.4 Fluorescence increase over time of substrates SM P 124 and SM P 127 95

3.3.5 Fluorescence increase over time of substrates SM P 130 and SM P 133 96
3.3.6 Fluorescence increase over time of substrates SM P 148 and SM P 151 96
3.3.7 Fluorescence increase over time of substrates SM P 154 and SM P 157 97
3.3.8 Fluorescence increase over time of substrates SM P 166 and SM P 169 97
3.3.9 Fluorescence increase over time of substrates SM P 172 and SM P 175 98
3.3.10 Fluorescence increase over time of substrates SM P 178 and SM P 181 98
3.3.11 Fluorescence increase over time of substrates SM P 125 and SM P 123 99
3.3.12 Fluorescence increase over time with AMCA-labeled substrates SM P 155 and commercially available OmniMMP^{TM} 100
3.3.13 Chromatograms of non-converted FRET substrate SM P 127 incubated with MMP-11 102
3.3.14 Chromatograms of FRET substrate SM P 124 incubated with MMP-11 103
3.3.15 Substrate activities with MMP-11 of fluorescein labeled FRET substrates SM P 124, SM P 125, SM P 130, SM P 148, and AMCA labeled substrate SM P 155 106
3.3.16 Substrate activities with MMP-14 of fluorescein labeled FRET substrates SM P 124, SM P 125, SM P 130, SM P 148, and AMCA labeled substrate SM P 155 109

3.3.17 Enzyme titration of different MMPs with FRET substrate SM P 124 115
3.3.18 SM P 124 substrate selectivity assayed with a variation of available MMPs 117
3.3.19 LC/MS-TOF validation of SM P 124 FRET assay with MMP-1, -2, -3, and -11 120
3.3.20 LC/MS-TOF validation of SM P 124 FRET assay with MMP-7, -8, -9, -10, -11, -12, and -13 121
3.3.21 Western blot of cell lysates 125
3.3.22 Cell lines assayed with substrate SM P 124 and neg. control SM P 123 126
3.3.23 MIA PaCa-2 cells with MMP-11 activatable FRET substrate SM P 124 and negative control SM P 123 128
3.3.24 MCF-7 cells with MMP-11 activatable FRET substrate SM P 124 and negative control SM P 123 129
3.3.25 Jurkat cells with MMP-11 activatable FRET substrate SM P 124 and negative control SM P 123 130
3.4.1 MMP-2 activatable tracer by Bremer *et al.* imaged in HT1080 xenograft [123] 132
3.4.2 Native chemical ligation enables substrate coupling to polymeric support 135
3.4.3 Loading determination of fluorescein-labeled conjugates 139
3.4.4 FRET efficiency of copolymer-conjugated substrates KK258 and neg control KK257 140
3.4.5 Singly labeled self-quenched conjugate vs doubly labeled NIR-FRET substrate conjugate 141
3.4.6 Synthesis scheme for copolymer-supported NIRF-labeled substrate 144

3.4.7 Labeling determination of NIRF-labeled conjugates 146
3.4.8 NIR-substrate conjugate FRET efficiency 147
3.5.1 Cellular turnover of copolymer-supported FRET probes KK258 and negative control copolymer-substrate KK257 151
3.5.2 Cellular turnover of NIRF-copolymer-supported FRET probes KK263, KK249 and negative control probe KK241 152
3.5.3 MIA PaCa-2 cells incubated with fluorescein-labeled conjugates 154
3.5.4 MIA PaCa-2 cells incubated with NIRF-labeled conjugates 156
3.5.5 MCF-7 cells incubated with NIRF-labeled conjugates 157
3.5.6 Jurkat cells incubated with NIRF-labeled conjugates 158
3.5.7 NIR-797 dye incubated with MIA PaCa-2 and MCF-7 cells 158
3.5.8 MIA PaCa-2 after incubation of 48 h of KK249, KK263, and non-targeted control KK241 159
3.6.1 Fluorescence reflectance imaging (FRI) 160
3.6.2 Biodistribution after 48 h of fluorescein-labeled conjugate KK258 and neg control KK257 (scrambled peptide sequence) 162
3.6.3 Biodistribution *ex vivo* 48 h after tail vein injection 162
3.6.4 Tumor signal over time of substrate copolymer conjugates KK258 and neg control KK257 (scrambled sequence) 164
3.6.5 Administration of KK258 14h after retrobulbar injection 167

3.6.6 *In vivo* clearance study for NIR-FRET conjugate KK249; Biodistribution *ex vivo* 21 h after tail vein injection 170
3.6.7 Biodistribution after 48 h of KK249, KK263, KK241 and SM P 117 172
3.6.8 Biodistribution *ex vivo* of NIR-FRET conjugate KK249 and self-quenched analog SM P 117 48 h after tail vein injection 173
3.6.9 Biodistribution *ex vivo* NIR-FRET conjugate KK263 48 h after tail vein injection 173
3.6.10 Biodistribution *ex vivo* of non-targeted copolymer KK241 48 h after tail vein injection 173
3.6.11 MIA PaCa-2 xenograft imaging; Trends of tumor signal emission 175
3.6.12 MIA PaCa-2 xenograft imaging of NIR-FRET conjugate KK249; red circle marks tumor 177
3.6.13 MIA PaCa-2 xenograft imaging of NIR-FRET conjugate with RRR motif KK263 nr. 22; red circle marks tumor 178
3.6.14 MIA PaCa-2 xenograft imaging of NIR-FRET conjugate with RRR motif KK263 nr. 23; red circle marks tumor 179
3.6.15 MIA PaCa-2 xenograft imaging of self-quenched conjugate SM P 117; red circle marks tumor . . . 180
3.6.16 MIA PaCa-2 xenograft imaging of non-targeted copolymer KK241; red circle marks tumor 181
3.6.17 False color images of xenografts recorded 24 h and 48 h after tail vein injection 182
3.7.1 Protease suscetible peptide labeled with Cryptophane-A 183

3.7.2 Tracer design with Cryptophane-A 184
3.7.3 Cryptophane-A coupling in solution 185
3.7.4 LC/MS-TOF validation of MMP-11 cleavable substrates sequence labeled with Cryptophane-A . . 187
3.7.5 Multiplexing probe generation: Cryptophane-A labeled FRET substrate 190
3.7.6 General multiplexing substrate 193
3.7.7 Copolymer conjugated FRET substrate for hyperpolarized xenon imaging of MMP-11 activity [91] 194

4.0.1 Patient's PDAC and normal tissue tested in Western Blot 195
4.0.2 General substrate assembly 197
4.0.3 Most active FRET substrate SM P 124 for MMP-11 199
4.0.4 Western blot of cell lysates 200
4.0.5 MIA PaCa-2 cells with FRET substrate SM P 124 and negative control SM P 123 201
4.0.6 Native chemical ligation enables substrate coupling to polymeric support 202
4.0.7 Administration of 3 nmol KK258 14 h prior to measurement 203
4.0.8 Synthesis scheme for copolymer-supported NIR labeled substrate 204
4.0.9 False color images of xenografts recorded 24 h and 48 h after tail vein injection 205
4.0.10 Copolymer-conjugated FRET substrate for hyperpolarized ^{129}Xe Imaging of MMP-11 206

6.0.1 FRET substrate library chromatograms SM P 124, SM P 127, and SM P 130 235

6.0.2 FRET substrate library chromatograms SM P 133, SM P 148, SM P 151, and SM P 154 236
6.0.3 FRET substrate library chromatograms SM P 157, SM P 166, SM P 169, and SM P 172 237
6.0.4 FRET substrate library chromatograms SM P 175, SM P 178, and SM P 181 238
6.0.5 LC/MS-TOF assay validation of SM P 124; small peak at 11.5 min represents single oxidized intact substrate, whereas evolving peak at 10.4 min displays cleaved substrate 239
6.0.6 LC/MS-TOF assay validation of SM P 127; small peak at 11.6 min represents single oxidized intact substrate, no cleavage product was observed . . . 240
6.0.7 LC/MS-TOF assay validation of SM P 130; small peak at 11.2 min represents single oxidized intact substrate, whereas evolving peak at 10.4 min displays cleaved substrate 241
6.0.8 LC/MS-TOF assay validation of SM P 133; small peak at 11.5 min represents single oxidized intact substrate, no substrate cleavage was observed . . 242
6.0.9 LC/MS-TOF assay validation of SM P 148; evolving peak at 10.4 min displays cleaved substrate . 243
6.0.10 LC/MS-TOF assay validation of SM P 151; small peak at 11.7 min represents single oxidized intact substrate, no substrate cleavage was observed . . 244
6.0.11 LC/MS-TOF assay validation of SM P 154; no substrate cleavage was observed 245
6.0.12 LC/MS-TOF assay validation of SM P 157; small peak at 11.5 min represents single oxidized intact substrate, no substrate cleavage was observed . . 246

6.0.13 LC/MS-TOF assay validation of SM P 166; substrate cleavage was only observed with MMP-14 . 247
6.0.14 LC/MS-TOF assay validation of SM P 169; small peak at 11.8 min represents single oxidized substrate, no substrate cleavage was observed 248
6.0.15 LC/MS-TOF assay validation of SM P 172; small peak at 12 min represents single oxidized substrate, no substrate cleavage was observed 249
6.0.16 LC/MS-TOF assay validation of SM P 175; small peak at 11.5 min represents small amounts of cleaved substrate with MMP-14, no substrate cleavage was observed with MMP-11 250
6.0.17 LC/MS-TOF assay validation of SM P 178; no substrate cleavage was observed 251
6.0.18 LC/MS-TOF assay validation of SM P 181; no substrate cleavage was observed 252
6.0.19 LC/MS-TOF assay validation of negative control substrate SM P 123; as anticipated, no substrate cleavage was observed 253
6.0.20 LC/MS-TOF assay validation of SM P 125; small peaks at 11.5 min and 11.8 min represent single and double oxidized intact substrate, whereas cleaved substrate can be observed at 10.5 min . . 254
6.0.21 LC/MS-TOF assay validation of AMCA labeled SM P 155; as anticipated, substrate cleavage was observed with both metalloproteases, at 254 nm both cleavage products are visible, namely peaks at 9.6 min and 10.4 min 255

6.0.22 LC/MS-TOF assay validation of commercially available OmniMMP^{TM} substrate; substrate cleavage was observed only with MMP-14, substrate cleavage peaks can be observed at 9.0 min and at 11.2 min 256
6.0.23 *In vivo* clearance study for SM P 117; Biodistribution *ex vivo* 21 h after tail vein injection . . . 257
6.0.24 *In vivo* clearance study for non-targeted KK241; Biodistribution *ex vivo* 21 h after tail vein injection 258

List of Tables

3.2.1 Sequence combination to yield substrates with high activity and selectivity for MMP-11 [99, 64, 55] . 69
3.2.2 Sequence library of peptidic substrates for MMP-11; Gray rows display sequences adopted from the literature 70
3.2.3 Cleavage cocktail for peptide substrates applied to the resin for 24 h at RT 75
3.2.5 Yields from substrate library, sequences adapted from the literature are highlighted in gray 78
3.2.6 Coumarin labeled FRET sequences synthesized . 82
3.3.1 Assay validation via fluorescence and LC/MS-TOF 104
3.3.2 Substrate Activity with MMP-11 107
3.3.3 Substrate activity with MMP-14 110
3.3.4 Sequence argumentation with crystal sructure information obtained from [64, 65, 57, 56, 53, 52, 48] 113
3.3.5 Enzyme activity determination of varying MMPs with FRET substrate SM P 124 115
3.3.6 SM P 124 activities for MMP-11 in comparison to other MMPs 118
3.4.1 Sequences synthesized for polymeric support and yields 137
3.4.2 Sequences and yields for NIRF-labeled substrates 143

3.4.3 Yields for unlabeled peptide-loaded pHPMA . . 145
3.7.1 Sequences and yields for xenon caged substrates . 186
3.7.2 Yields of multiplexing probes for FRET and hp ^{129}Xe imaging 192

4.0.1 Sequence library of peptidic substrates for MMP-11 196
4.0.2 Proposed sequence for activity and selectivity optimization 198

5.2.2 Synthesized Peptide FRET Substrates for *in vitro* Validation 225
5.3.1 Statistical significance determination 231
5.3.2 Buffers used for western blotting 232

Bibliography

[1] Patten LC and Berger DH, Role of proteases in pancreatic carcinoma. World J. Surg. (2005) vol. 29 (3) pp. 258-63

[2] Greenlee RT, Hill-Harmon MB, Murray T, Thun M, Cancer statistics, CA Cancer J. Clin. (2001) vol. 51 pp. 15-36

[3] Parkin DM, Pisani P, Ferlay J. Estimates of the worldwide incidence of 25 major cancers in 1990. Int. J. Cancer (1999) vol. 80 pp. 827-841

[4] Nagakawa T, Konishi I, Higashino Y, et al., The spread and prognosis of carcinoma in the region of the pancreatic head, Jpn. J. Surg (1989) vol. 19 pp. 510–518

[5] Nagakawa T, Kayahara M, Ueno K et al. A clinicopathologic study on neural invasion in cancer of the pancreatic head, Cancer (1992) vol. 69 pp. 930–935

[6] Mollenhauer J, Roether I, Kern HP, Distribution of extracellular matrix proteins in pancreatic ductal adenocarcinoma and its influence on tumor cell proliferation *in vitro*, Pancreas (1987) vol. 2 pp. 14–24

[7] Gress TM, Neoptolemos JP, Lemoine NR, Real FX, Exocrine pancreas cancer, The European Pancreatic Cancer-Research Cooperative (EPC-RC) (2004)

[8] Anderson KE, Potter JD, Mack TM, Cancer Epidemiology and Prevention, eds Schottenfeld D & Fraumeni JJ, Oxford University Press, New York (1996) pp. 725–771

[9] Ekbom A, Hunter D, Pancreatic cancer. In: Adami HO, Hunter D, Trichopoulos D, Textbook of cancer epidemiology. New York: Oxford University Press, New York (2002)

[10] Anderson KE, Hammons GJ, Kadlubar FF, Potter JD, Kaderlik KR, Ilett KF, Minchin RF, Teitel CH, Chou HC, Martin MV, Guengerich FP, Barone GW, Lang NP, Peterson LA. Metabolic activation of aromatic amines by human pancreas. Carcinogenesis (1997) vol. 18 pp. 1085-1092

[11] Wang M, Abbruzzese JL, Friess H, Hittelman WN, Evans DB, Abbruzzese MC, Chiao P, Li D, DNA adducts in human pancreatic tissues and their potential role in carcinogenesis, Cancer Res. (1998) vol. 58 pp. 38-41

[12] Phillips DH, Smoking-related DNA and protein adducts in human tissues, Carcinogenesis (2002) vol. 23 pp. 1979-2004

[13] Risch HA, Etiology of pancreatic cancer, with a hypothesis concerning the role of N-nitroso compounds and excess gastric acidity, J. Natl. Cancer Inst. (2003) vol. 95 pp. 948-960

[14] Fernandez E, La Vecchia C, Decarli A, Attributable risks for pancreatic cancer in northern Italy, Cancer Epidemiol. Biomarkers Prev. (1996) vol. 5 pp. 23-27

[15] Hezel AF et al. Genetics and biology of pancreatic ductal adenocarcinoma. Genes Dev. (2006) vol. 20 (10) pp. 1218-49

[16] Mangray S, King TC, Molecular pathobiology of pancreatic adenocarcinoma, Frontiers in Bioscience (1998) vol. 3 pp. 1148-1160

[17] Flanders TY, Foulkes WD, Pancreatic adenocarcinoma: epidemiology and genetics, J. Med. Genet. (1996) vol. 33 pp. 889-898

[18] The Breast Cancer Linkage Consortium, Cancer risks in BRCA2 mutation carriers, J. Natl. Cancer Inst. (1999) vol. 91 pp. 1310-1316

[19] Klein AP, Hruban RH, Brune KA, Petersen GM, Goggins M. Familial pancreatic cancer, Cancer J. (2001) vol. 7 pp. 266-273

[20] Bartsch DK et al. CDKN2A germline mutations in familial pancreatic cancer, Ann. Surg. (2002) vol. 236 pp. 730-737

[21] Hahn SA et al. BRCA2 germline mutations in familial pancreatic carcinoma, J. Natl. Cancer Inst. (2003) vol. 95 pp. 214-221

[22] Rogers CD, van der Heijden MS, Brune K, Yeo CJ, Hruban RH, Kern SE, Goggins M, The genetics of FANCC and FANCG in familial pancreatic cancer, Cancer Biol. Ther. (2004) vol. 3 pp. 167-169

[23] Lowenfels AB et al. Pancreatitis and the risk of pancreatic cancer, N. Engl. J. Med. (1993) vol. 328 pp. 1433-1437

[24] Hruban RH et al. An illustrated consensus on the classification of pancreatic intraepithelial neoplasia and intraductal papillary mucinous neoplasm, Am J. Surg. Path. (2004) vol. 28 pp. 977-987

[25] Klein WM, Hruban RH, Klein-Szanto AJP, Wilentz RE, Dysplasia in Pancreatic Intraepithelial Neoplasia (PanIN): Additional Evidence for a Recently Proposed Model of Progression, Mod. Pathol. (2002) vol. 15(4) pp. 441–447

[26] Bardeesy N and DePinho RA, Pancreatic Cancer Biology and Genetics, Nature Reviews (2002) vol. 2 pp. 897-909

[27] Moskaluk CA, Hruban RH, Kern SE. p16 and K-ras gene mutations in the intraductal precursors of human pancreatic adenocarcinoma, Cancer Res. (1997) vol. 57 pp. 2140–2143

[28] Wilentz RE et al. Inactivation of the p16 (INK4A) tumor suppressor gene in pancreatic duct lesions: loss of intranuclear expression, Cancer Res. (1998) vol. 58 pp. 4740–4744

[29] DiGiuseppe JA et al. Overexpression of the p53 protein in adenocarcinoma of the pancreas, Am. J. Clin. Pathol. (1994) vol. 101 pp. 684–688

[30] Day JD et al. Immunohistochemical evaluation of HER-2/neu oncogene expression in pancreatic adenocarcinoma and pancreatic intraepithelial neoplasms, Hum. Pathol. (1996) vol. 27 pp. 119–124

[31] Yanagisawa A et al. Frequent c-K-ras oncogene activation in mucous cell hyperplasias of pancreas suffering from chronic inflammation, Cancer Res. (1993) vol. 53 pp. 953–956

[32] Tada M et al. Analysis of K-ras gene mutation in hyperplastic duct cells of the pancreas without pancreatic disease, Gastroenterology (1996) vol. 110 pp. 227–231

[33] Caldas C, Hahn SA, Hruban RH, Redston MS, Yeo CJ, Kern SE, Detection of K-ras mutations in the stool of patients with pancreatic adenocarcinoma and pancreatic ductal hyperplasia, Cancer Res. (1994) vol. 54 pp. 3568–3573

[34] Hameed M, Marrero AM, Conlon KC, Brennan MF, Klimstra DS, Expression of p53 nucleophosphoprotein in in situ pancreatic ductal adenocarcinoma: an immunohistochemical analysis of 100 cases [abstract], Lab. Invest. (1994) vol. 70 pp. 132A

[35] Wilentz RE et al. Loss of expression of Dpc4 in pancreatic intraepithelial neoplasia: evidence that DPC4 inactivation occurs late in neoplastic progression, Cancer Res. (2000) vol. 60 pp. 2002–2006

[36] Klimstra DS and Longnecker DS, K-ras mutations in pancreatic ductal proliferative lesions, Am. J. Pathol. (1994) vol. 145 pp. 1547–1550

[37] Sipos B, Frank S, Gress T, Hahn S, Klöppel G, Pancreatic Intraepithelial Neoplasia – Revised and Updated, Pancreatology (2009) vol. 9 pp. 45-54

[38] Solcia E, Capella C, Kloppel G. Tumors of the pancreas. Atlas of tumor pathology, 3rd series, fascicle 20. Washington, DC: Armed Forces Institute of Pathology (1997)

[39] Martinez-Hernandez A, Amenta PS, The basement membrane in pathology, Lab. Invest. (1983) vol. 48 pp. 656-677

[40] Schmitt M, Harbeck N, Thomssen C, et al. Clinical impact of the plasminogen activation system in tumor invasion and metastasis: Prognostic relevance and target for therapy, Thromb. Haemost. (1997) vol. 78 pp. 285-296

[41] Snoek-van Beurden PAM and Von den Hoff JW. Zymographic techniques for the analysis of matrix metalloproteinases and their inhibitors. BioTechniques (2005) vol. 38 (1) pp. 73-83

[42] Andreini C et al. Bioinformatic Comparison of Structures and Homology-Models of Matrix Metalloproteinases. J. Proteome Res. (2004) vol. 3 (1) pp. 21-31

[43] Murphy G, Segain J-P, O'Shea M, et al. The 28-kDa N-terminal domain of mouse stromelysin-3 has the general properties of a weak metalloproteinase. J. Biol. Chem. (1993) vol. 268 (29) pp. 15435-15441

[44] Pei D et al. Hydrolytic Inactivation of a Breast Carcinoma Cell-derived Serpin by Human Stromelysin-3. J. Biol. Chem. (1994) vol. 269 (41) pp. 25849-25855

[45] Bode W, Gomis-Ru X, Stocker W. Astacins, serralysins, snake venom and matrix metalloproteinases exhibit identical zinc-binding environments (HEXXHXXGXXH and Met-turn) and topologies and should be grouped into a common family, the Metzincins, FEBS Lett. (1993) vol. 331 pp. 134–140

[46] Nagase H et al. Structure and function of matrix metalloproteinases and TIMPs. Cardiovasc. Res. (2006) vol. 69 (3) pp. 562-573

[47] Sternlicht MD und Werb Z. How matrix metalloproteinases regulate cell behavior. Annu. Rev. Cell. Dev. Biol. (2001) vol. 17 pp. 463-516

[48] Bode W et al. Structural properties of matrix metalloproteinases. Cell. Mol. Life Sci. (1999) vol. 55 (4) pp. 639-52

[49] Bertini I et al. Snapshots of the Reaction Mechanism of Matrix Metalloproteinases. Angew. Chem. Int. Ed. (2006) vol. 45 pp. 7952 –7955

[50] Egeblad M and Werb Z. New functions for the matrix metalloproteinases in cancer progression. Nat. Rev. Cancer (2002) vol. 2 (3) pp. 161-174

[51] Blundell T. Metalloproteinase super-families and drug design. Structural Biology (1994) vol. 1 (2) pp. 73-75

[52] Tallant C et al. Matrix metalloproteinases: Fold and function of their catalytic domains. BBA - Molecular Cell Research (2010) vol. 1803 (1) pp. 20-28

[53] Bode W and Maskos K. Matrix metalloproteinases. Handbook of Metalloproteins (2004) pp. 1-18

[54] Niedzwiecki L et al. Substrate Specificity of the Human Matrix Metalloproteinase Stromelysin and the Development of Continuous Fluorometric Assays. Biochemistry (1992) vol. 31 (50) pp. 12618-12623

[55] Holtz B et al. Role of the S1´ Subsite Glutamine 215 in Activity and Specificity of Stromelysin-3 by Site-Directed Mutagenesis. Biochemistry (1999) vol. 38 pp. 12174-12179

[56] Bode W et al. The X-ray crystal structure of the catalytic domain of human neutrophil collagenase inhibited by a substrate analogue reveals the essentials for catalysis and specificity. The EMBO Journal (1994) vol. 13 (6) pp. 1263-1269

[57] Rowsell S et al. Crystal structure of human MMP-9 in complex with a reverse hydroxamate inhibitor. J. Mol. Biol. (2002) vol. 319 (1) pp. 173-181

[58] Maskos K. Crystal structures of MMPs in complex with physiological and pharmacological inhibitors. Biochimie (2005) vol. 87 pp. 249–263

[59] Grams F et al. X-ray structures of human neutrophil collagenase complexed with peptide hydroxamate and peptide thiol inhibitors. Implications for substrate binding and rational drug design. Eur. J. Biochem. (1995) vol. 228 (3) pp. 830-841

[60] Basset P and Rio MC. MMP-11 (matrix metalloproteinase 11 (stromelysin 3)). Atlas Genet. Cytogenet. Oncol. Haematol. March (2000)
URL : http://AtlasGeneticsOncology.org/Genes/ST3ID200.html

[61] Pei D and Weiss SJ. Furin-dependent intracellular activation of the human stromelysin-3 zymogen. Nature (1995) vol. 375 (6528) pp. 244-247

[62] Visse R and Nagase H. Matrix metalloproteinases and tissue inhibitors of metalloproteinases: structure, function, and biochemistry. Circ. Res. (2003) vol. 92 (8) pp. 827-839

[63] Luo D et al. Alternative splicing and promoter usage generates an intracellular stromelysin 3 isoform directly translated as an active matrix metalloproteinase. J. Biol. Chem. (2002) vol. 277 (28) pp. 25527-25536

[64] Pan W et al. Identification of peptide substrates for human MMP-11 (stromelysin-3) using phage display. J. Biol. Chem. (2003) vol. 278 (30) pp. 27820-27827

[65] Matziari M et al. Matrix Metalloproteinase 11 (MMP-11; Stromelysin-3) and Synthetic Inhibitors. Med. Res. Rev. (2006) pp. 1-25

[66] Gall AL et al. Crystal Structure of the Stromelysin-3 (MMP-11) Catalytic Domain Complexed With a Phosphinic Inhibitor Mimicking the Transition-state. J. Mol. Biol. (2001) vol. 301 pp. 577-586

[67] Jones LE et al. Comprehensive analysis of matrix metalloproteinase and tissue inhibitor expression in pancreatic cancer: increased expression of matrix metalloproteinase-7 predicts poor survival. Clin. Cancer Res. (2004) vol. 10 (8) pp. 2832-2845

[68] Hanbidge AE. Cancer of the pancreas: the best image for early detection-CT, MRI, PET or US?. Can. J. Gastroenterol. (2002) vol. 16 (2) pp. 101-105

[69] von Burstin J et al. Highly sensitive detection of early-stage pancreatic cancer by multimodal near-infrared molecular imaging in living mice. Int. J. Cancer (2008) vol. 123 (9) pp. 2138-2147

[70] Weissleder R and Mahmood U. Molecular Imaging. Radiology (2001) vol. 219 pp. 316–333

[71] Weissleder R. Molecular Imaging in Cancer. Science (2006) vol. 312 pp. 1168-1171

[72] Fass L. Imaging and cancer: A review. Mol. Oncol. (2008) vol. 2 pp. 115-152

[73] Dzik-Jurasz ASK. Molecular imaging *in vivo*: an introduction. Br. J. Radiol. (2003) vol. 76 Spec No 2 pp. S98-109

[74] Scherer RL et al. Cancer Metastasis Rev. (2008) vol. 27 (4) pp. 679-690

[75] Kovar JL et al. A systematic approach to the development of fluorescent contrast agents for optical imaging of mouse

cancer models. Analytical Biochemistry (2007) vol. 367 (1) pp. 1-12

[76] Lee S et al. Peptides and peptide hormones for molecular imaging and disease diagnosis. Chem. Rev. (2010) vol. 110 (5) pp. 3087-3111

[77] Weissleder R and Ntziachristos V. Shedding light onto live molecular targets. Nat. Med. (2003) vol. 9 (1) pp. 123-128

[78] Chance B. Optical method. Annu. Rev. Biophys. Biophys. Chem. (1991) vol. 20 pp. 1-28

[79] Förster T. Zwischenmolekulare Energiewanderung und Fluoreszenz. Annalen der Physik (1948) vol. 6 (2) pp. 55-75

[80] Image was created by Sven Jähnichen, Schwarme, Germany

[81] Tyagi S and Kramer FR. Molecular beacons: probes that fluoresce upon hybridization. Nat. Biotechnol. (1996) vol. 14 (3) pp. 303-308

[82] Squire LF, Novelline RA. Squire's fundamentals of radiology (5th ed.). Harvard University Press. (1997) ISBN 0-674-83339-2.

[83] Nazarenko IA et al. A closed tube format for amplification and detection of DNA based on energy transfer. Nucleic Acids Res. (1997) vol. 25 (12) pp. 2516-2521

[84] Taratula O and Dmochowski IJ. Functionalized ^{129}Xe contrast agents for magnetic resonance imaging. Curr. Opin. Chem. Biol. (2010) vol. 14 (1) pp. 97-104

[85] Louie AY et al. *In vivo* visualization of gene expression using magnetic resonance imaging. Nat. Biotechnol. (2000) vol. 18 (3) pp. 321-325

[86] Tran LA et al. Gadonanotubes as magnetic nanolabels for stem cell detection. Biomaterials (2010) vol. 31 (36) pp. 9482-9491

[87] Albert MS et al. Biological magnetic resonance imaging using laser-polarized ^{129}Xe. Nature (1994) vol. 370 (6486) pp. 199-201

[88] Oros AM and Shah NJ. Hyperpolarized xenon in NMR and MRI. Phys. Med. Biol. (2004) vol. 49 (20) pp. R105-153

[89] Stupic KF et al. Hyperpolarized (131)Xe NMR spectroscopy. Journal of magnetic resonance (San Diego, Calif : 1997) (2010) vol. online release

[90] de Graaf RA. *In vivo* NMR Spectroscopy, 2nd Edition, Wiley VCH (2007)

[91] Images are a courtesy of Dr. Leif Schröder, Molecular Imaging Group, Leibniz-Institut für molekulare Pharmakologie (FMP), 13125 Berlin, Germany

[92] Duhamel G et al. Xenon-129 MR imaging and spectroscopy of rat brain using arterial delivery of hyperpolarized xenon in a lipid emulsion. Magn. Reson. Med. (2001) vol. 46 (2) pp. 208-122

[93] Ruppert K et al. Exploring lung function with hyperpolarized ^{129}Xe nuclear magnetic resonance. Magn. Reson. Med. (2004) vol. 51 (4) pp. 676-687

[94] Driehuys B et al. Imaging alveolar-capillary gas transfer using hyperpolarized ^{129}Xe MRI. Proc. Natl. Acad. Sci. (2006) vol. 103 (48) pp. 18278-18283

[95] Bartik K et al. ^{129}Xe and ^{1}H NMR Study of the Reversible Trapping of Xenon by Cryptophane-A in Organic Solution. J. Am. Chem. Soc. (1998) vol. 120 (4) pp. 784-791

[96] Schröder L et al. Molecular Imaging Using a Targeted Magnetic Resonance Hyperpolarized Biosensor. Science (2006) vol. 314 pp. 446-449

[97] Basset P, Wolf C, Rouyer N, Bellocq JP, Rio MC, Chambon P. Stromelysin-3 in stromal tissue as a control factor in breast cancer behavior. Cancer (Phila) (1994) vol. 74 pp. 1045–1049

[98] Muller D, Wolf C, Abecassis J, et al. Increased stromelysin-3 gene expression is associated with increased local invasiveness in head and neck squamous cell carcinomas. Cancer Res. (1993) vol. 53 pp. 165–169

[99] Mucha A et al. Membrane Type-1 Matrix Metalloprotease and Stromelysin-3 Cleave More Efficiently Synthetic Substrates Containing Unusual Amino Acids in Their P1' Positions. J. Biol. Chem. (1998) vol. 273 (5) pp. 2763–2768

[100] Monici M. Cell and tissue autofluorescence research and diagnostic applications. Biotechnology Annual Review (2005) vol. Volume 11 pp. 227-256

[101] Stack MS and Gray RD. Comparison of Vertebrate Collagenase and Gelatinase Using a New Fluorogenic Substrate Peptide. J. Biol. Chem. (1989) vol. 264 (8) pp. 4277-4281

[102] Netzel-Arnett S, Mallya SK, Nagase H, Birkedal-Hansen H, van Wart HE. Continuously recording fluorescent assays optimized for five human matrix metalloproteinases. Anal. Biochem. (1991) vol. 195 pp. 86-92

[103] Pei D and Weiss SJ. Transmembrane-deletion mutants of the membrane-type matrix metalloproteinase-1 process progelatinase A and express intrinsic matrix-degrading activity. J. Biol. Chem. (1996) vol. 271 (15) pp. 9135-9140

[104] Nagase H. Activation mechanisms of matrix metalloproteinases. Biol. Chem. (1997) vol. 378 pp. 151–160

[105] Uryga-Polowy V et al. Resin-Bound Aminofluorescein for C-Terminal Labeling of Peptides: High-Affinity Polarization Probes Binding to Polyproline-Specific GYF Domains. ChemBioChem (2008) vol. 9 (15) pp. 2452-2462

[106] Isidro-Llobet A et al. Amino acid-protecting groups. Chem. Rev. (2009) vol. 109 (6) pp. 2455-2504

[107] Wood WJ et al. Substrate activity screening: a fragment-based method for the rapid identification of nonpeptidic protease inhibitors. J. Am. Chem. Soc. (2005) vol. 127 (44) pp. 15521-15527

[108] Togashi DM et al. Investigating tryptophan quenching of fluorescein fluorescence under protolytic equilibrium. J. Phys. Chem. A. (2009) vol. 113 (12) pp. 2757-2767

[109] Greenfield NJ. Using circular dichroism spectra to estimate protein secondary structure. Nat. Protoc. (2006) vol. 1 (6) pp. 2876-2890

[110] Nelson DL and Cox MM. Lehninger Principles of Biochemistry. (2000) 3rd Ed, Worth Publishers, USA

[111] Page URL: http://commons.wikimedia.org/wiki/File:Michaelis-Menten_saturation_curve_of_an_enzyme_reaction.svg

[112] Page URL: http://commons.wikimedia.org/wiki/File:-Enzyme_progress_curve.png

[113] Noirey N, Staquet MJ, Gariazzo MJ, Serres M, André C, Schmitt D, Vincent C. Relationship between expression of matrix metalloproteinases and migration of epidermal and *in vitro* generated Langerhans cells, Eur. J. Cell. Biol. (2002) vol. 81(7) pp. 383-389

[114] Apte SS et al. The matrix metalloproteinase-14 (MMP-14) gene is structurally distinct from other MMP genes and is co-expressed with the TIMP-2 gene during mouse embryogenesis. J. Biol. Chem. (1997) vol. 272 (41) pp. 25511-25517

[115] Scott K et al. TNF-α regulates epithelial expression of MMP-9 and integrin αvβ6 during tumour promotion. A role for TNF-α in keratinocyte migration? Oncogene (2004) vol. 23 (41) pp. 6954-6966

[116] Marks V, Cantor T, Meško D, Pullman R, Nosalova G. Differential diagnosis by laboratory medicine: a quick reference for physicians. Springer Verlag Berlin (2002) pp. 264

[117] Ohuchi E et al. Membrane type 1 matrix metalloproteinase digests interstitial collagens and other extracellular matrix macromolecules. J. Biol. Chem. (1997) vol. 272 (4) pp. 2446-2451

[118] d'Ortho MP et al. Membrane-type matrix metalloproteinases 1 and 2 exhibit broad-spectrum proteolytic capacities comparable to many matrix metalloproteinases. Eur. J. Biochem. (1997) vol. 250 (3) pp. 751-757

[119] Fosang AJ et al. Membrane-type 1 MMP (MMP-14) cleaves at three sites in the aggrecan interglobular domain. FEBS Lett. (1998) vol. 430 (3) pp. 186-90

[120] Basset P et al. A novel metalloproteinase gene specifically expressed in stromal cells of breast carcinomas. Nature (1990) vol. 348 (6303) pp. 699-704

[121] Von Burstin J et al. Highly sensitive detection of early-stage pancreatic cancer by multimodal near-infrared molecular imaging in living mice. Int. J. Cancer (2008) vol. 123 (9) pp. 2138-2147

[122] Julyana PJ et al. Preliminary clinical study of the distribution of HPMA copolymers bearing doxorubicin and galactosamine. Journal of Controlled Release (1999) vol. 57 pp. 281–290

[123] Bremer C et al. *In vivo* molecular target assessment of matrix metalloproteinase inhibition. Nature Medicine (2001) vol. 7 (6) pp. 743-748

[124] Seljelid R et al. The effect of poly-L-lysine on the uptake of retrovirus double-stranded RNA in macrophages *in vitro*. J. Cell. Biol. (1973) vol. 57 (2) pp. 484-498

[125] Bogdanov AA et al. An Adduct of cis-Diamminedichloroplatinum(II) and Poly(ethylene glycol)poly(L-lysine)-Succinate: Synthesis and Cytotoxic Properties. Bioconjugate Chem. (1996) vol. 7 pp. 144-149

[126] Tung CH et al. *In vivo* imaging of proteolytic enzyme activity using a novel molecular reporter. Cancer Res. (2000) vol. 60 (17) pp. 4953-4958

[127] Lu Z-R et al. Molecular imaging of HPMA copolymers: Visualizing drug delivery in cell, mouse and man. Advanced Drug Delivery Reviews (2010) vol. 62 (2) pp. 246-257

[128] Kopeček J, Soluble biomedical polymers, Polim. Med. (1977) vol. 7 pp. 191–221

[129] Kopeček J, Controlled biodegradability of polymers—a key to drug delivery systems, Biomaterials (1984) vol. 5 pp. 19–25

[130] Kopeček J, Kopecková P, Minko T, Lu Z-R, HPMA copolymer–anticancer drug conjugates: design, activity, and mechanism of action, Eur. J. Pharm. Biopharm. (2000) vol. 50 pp. 61–81

[131] Lu Z-R, Shiah JG, Sakuma S, Kopecková P, Kopeček J, Design of novel bioconjugates for targeted drug delivery, J. Control. Release (2002) vol. 78 pp. 165–173

[132] Thomson AH, Vasey PA, Murray LS, Cassidy J, Fraier D, Frigerio E, Twelves C, Population pharmacokinetics in phase I drug development: a phase I study of PK1 in patients with solid tumours, Br. J. Cancer (1999) vol. 81 pp. 99–107

[133] Seymour LW, Ferry DR, Anderson D, Hesslewood S, Julyan PJ, Poyner R, Doran J, Young AM, Burtles S, Kerr DJ, Cancer Research Campaign Phase I/II Clinical Trials committee, Hepatic drug targeting: phase I evaluation of polymerbound doxorubicin, J. Clin. Oncol. (2002) vol. 20 pp. 1668

[134] Gianasi E, Wasil M, Evagorou EG, Keddle A, Wilson G, Duncan R, HPMA copolymer platinates as novel antitumour agents: in vitro properties, pharmacokinetics and antitumor activity in vivo, Eur. J. Cancer. (1999) vol. 35 pp. 994

[135] Dawson PE et al. Synthesis of Proteins by Native Chemical Ligation, Science (1994) vol. 266 (5186) pp. 776-779

[136] Wagner M et al. A murine tumor progression model for pancreatic cancer recapitulating the genetic alterations of the human disease. Genes & Development (2001) vol. 15 (3) pp. 286-293

[137] Holliger P and Hudson PJ. Engineered antibody fragments and the rise of single domains. Nat. Biotechnol. (2005) vol. 23 (9) pp. 1126-1136

[138] Noguchi Y et al. Early phase tumor accumulation of macromolecules: a great difference in clearance rate between tumor and normal tissues. Jpn. J. Cancer Res. (1998) vol. 89 (3) pp. 307-314

[139] Duncan R, The dawning era of polymer therapeutics, Nat. Rev. Drug Discov. 2 (2003) pp. 347-360.

[140] Kopeček J, Kopeckova P, Minko T, Lu Z-R, Peterson CM, Water soluble polymers in tumor targeted delivery, J. Control. Release (2001) vol. 74 pp. 147-158

[141] Rihova B, Kubackova K, Clinical implications of N-(2-hydroxypropyl)methacrylamide copolymers, Curr. Pharm. Biotechnol. (2003) vol. 4 pp. 311-322

[142] Wei Q et al. Designing ^{129}Xe NMR biosensors for matrix metalloproteinase detection. J. Am. Chem. Soc. (2006) vol. 128 (40) pp. 13274-13283

[143] Coin I, Beyermann M, Bienert M, Nature Protocols (2007) pp. 461

[144] Kaiser E, Colescott RL, Bossinger CD, Cook PI, Analytical Biochemistry (1970) vol. 34 pp. 595

[145] Nuti E et al. Journal of Medicinal Chemistry (2009) vol. 52 (20) pp. 6347-6361

[146] Holmbeck K et al. MT1-MMP-deficient mice develop dwarfism, osteopenia, arthritis, and connective tissue disease due to inadequate collagen turnover. Cell (1999) vol. 99 (1) pp. 81-92

[147] Pham W et al. Developing a peptide-based near-infrared molecular probe for protease sensing. Bioconjug Chem (2004) vol. 15 (6) pp. 1403-1407